# EARLY ASSESSMENT OF TUMOR RESPONSE TO RADIATION THERAPY USING HIGH-RESOLUTION CONTRAST ENHANCED ULTRASOUND IMAGING TECHNIQUES AND APPLICATIONS FOR PROSTATE CANCER

Sandeep K. Kasoji

A dissertation submitted to the faculty of the University of North Carolina at Chapel Hill in partial fulfillment of the requirements for the degree of Doctor of Philosophy in the Department of Biomedical Engineering in the School of Medicine.

Chapel Hill
2018

Approved by:

Paul A. Dayton

X. Sha Chang

Xiaoning Jiang

Emily Chang

Ronald Chen

## ABSTRACT

Sandeep K. Kasoji: Early Assessment of Tumor Response to Radiation Therapy Using Advanced Contrast Enhanced Ultrasound Imaging Techniques and Applications for Prostate Cancer
(Under the direction of Paul A. Dayton)

Traditional anatomical imaging for cancer diagnosis and assessing response to therapy is limited to just the superficial appearance of a tumor. A functional imaging approach, which takes a closer at look various microenvironments within the tumor, is likely to offer a more holistic view of the tumor behavior and response to treatment. Acoustic Angiography is a novel super-harmonic contrast ultrasound imaging technique that utilizes a dual-frequency transducer to quickly generate high-resolution 3D microvascular images with exceptionally high contrast-to-tissue ratio. Herein, we demonstrate the ability of Acoustic Angiography to quantify tumor microvascular features and investigate their changes after therapeutic doses of radiation therapy in a tumor bearing rodent model. We then demonstrate using functional longitudinal data analysis that quantified microvascular features can be used to predict radiation therapy response with limited time point measurements.

Prostate cancer is the most common cancer in men, resulting in near 30,000 deaths a year in the United States alone. Current diagnostic and staging techniques for prostate cancer have been shown to have low sensitivity and specificity, limiting early detection and intervention. There is potential for improving ultrasound imaging techniques for aiding in prostate cancer detection and biopsy guidance with Acoustic Angiography imaging. The clinical translation of

Acoustic Angiography hinges on certain design improvements, primarily increased depth of penetration. The last part of this dissertation discusses the development of a dual-frequency linear array transducer for Acoustic Angiography.

This dissertation consists of two primary hypotheses:

*1)* Acoustic Angiography can be used to quantify changes in tumor microvascular features and predict radiation treatment response earlier than using tumor volume alone.

*2)* Acoustic Angiography using a dual-frequency linear array transducer is suitable for prostate cancer imaging.

This is dedicated to:

My wife, Dr. Meghana Konanur, who has been a constant source of love and encouragement throughout my academic career.

My family, who through their patience, guidance, love, and support, made this Ph.D. work possible.

All of my teachers and professors throughout my entire education who have advised and encouraged me to aspire for academic excellence.

## ACKNOWLEDGMENTS

I would like to first thank Dr. Paul Dayton, who has been an incredibly supportive adviser. His constant support and guidance throughout my graduate career is greatly appreciated and will always be remembered. I would next like to thank Dr. Sha Chang, whose enthusiasm for novel research has been the backbone for the first section of my thesis. I would like to thank the rest of my committee, Drs. Emily Chang, Xiaoning Jiang, and Ronald Chen, for their indispensable guidance throughout this Ph.D. work in their respective fields of expertise.

I would next like to acknowledge all of my collaborators who made this work possible. Specifically, Drs. Sibo Li and Jinwook Kim for their expertise in novel transducer design, and Dr. Stuart Foster and his lab for their expertise in fabricating dual-frequency transducers. I would also like to thank all of the undergraduate students (Ruby Patel and Amit Cudykier) who I have had the pleasure of mentoring. They made significant contributions to data analysis that helped move these projects forward.

I would like to thank all of the past and current members of the Dayton Lab. I have learned a great deal from each and every one of them. Their kindness and friendship will always be remembered. Lastly, I would like to thank all of my friends and mentors who have acted as role models for me throughout my life. This work and many of my other accomplishments are a result of collective thought and collaboration.

*"I am what I am because of who we all are" – Ubuntu Philosophy*

## TABLE OF CONTENTS

## LIST OF FIGURES

## LIST OF TABLES

## LIST OF ABBREVIATIONS

| | |
|---|---|
| 2D | Two-Dimensional |
| 3D | Three-Dimensional |
| AA | Acoustic Angiography |
| AML | Angiomyolipoma |
| A-T | Adenine-Thymine |
| AUC | Area Under the Curve |
| $a_v\beta_3$ | Alpha-v-beta-3 integrin |
| B-mode | Brightness Mode |
| ccRCC | Clear Cell Renal Cell Carcinoma |
| CE | Contrast Enhanced |
| CEUS | Contrast Enhanced Ultrasound Imaging |
| ChIP | Chromatin Immunoprecipitation |
| chRCC | Chromophobe Renal Cell Carcinoma |
| CPS | Cadence Pulse Sequence |
| CT | Computed Tomography |
| CTR | Contrast-to-Tissue Ratio |
| CTRdB | Contrast-to-Tissue Ratio (measured with voltage data) |

| | |
|---|---|
| CTRImg | Contrast-to-Tissue Ratio (measured with image data) |
| dB | Decibel |
| DFB | Decafluorobutane |
| DF-TRUS | Dual-Frequency Transrectal Ultrasound |
| DICOM | Digital Imaging and Communications in Medicine |
| DM | Distance Metric |
| DMAS | Delay-Multiply-and-Sum |
| DNA | Deoxyribonucleic Acid |
| DP-DF | Dual-Probe/Dual-Frequency |
| DRE | Digital Rectal Examination |
| EV-8C4 | (Siemens Prostate Transducer) |
| FDA | Functional Data Analysis |
| FDG | Fluorodeoxyglucose |
| FFT | Fast Fourier Transform |
| fPCA | Functional Principal Component Analysis |
| FSA | Fibrosarcoma |
| FWHM | Full-Width Half-Max |
| G-C | Guanine-Cytosine |

| | |
|---|---|
| gDNA | Genomic DNA |
| Gy | Gray (unit of ionizing radiation dose) |
| Hz | Hertz (unit of frequency) |
| IQR | Interquartile Range |
| IV | Intravenous |
| MATLAB | (Mathworks computational program) |
| MHz | Megahertz (unit of frequency) |
| MI | Mechanical Index |
| MIP | Maximum Intensity Projection |
| MPa | Megapascal |
| MRA | Magnetic Resonance Angiography |
| MRI | Magnetic Resonance Imaging |
| MV | MegaVolts |
| MVm | Microvascular metric |
| OCT | Oncocytoma |
| OCT | Optical Coherence Tomography |
| PACE | Principal Analysis by Conditional Expectation |
| PC | Principal Component |

| | |
|---|---|
| PCa | Prostate Cancer |
| PCR | Polymerase Chain-Reaction |
| PEG | Polyethylene Glycol |
| PET | Positron Emission Tomography |
| PI | Peak Intensity |
| PN | Percent Necrosis |
| pRCC | Papillary Renal Cell Carcinoma |
| PSA | Prostate Specific Antigen |
| PZT | Lead Zirconate Titanate |
| RCC | Renal Cell Carcinoma |
| RECIST | Response Evaluation Criteria in Solid Tumors |
| RF | Radio Frequency |
| RMV | (Dual-element probe used for AA) |
| RNA | Ribonucleic Acid |
| ROC | Receiver Operator Characteristic |
| ROI | Region of Interest |
| ROS | Reactive Oxygen Species |
| RT | Radiation Therapy |

| | |
|---|---|
| SBRT | Stereotactic Body Radiotherapy |
| SNR | Signal-to-Noise Ratio |
| SNRdB | Signal-to-Noise Ratio (measured with voltage data) |
| SNRImg | Signal-to-Noise Ratio (measured with image data) |
| SOAM | Sum of Angles Metric |
| SPECT | Single Photon Emission Computed Tomography |
| SRS | Stereotactic Radiosurgery |
| SSD | Source-to-Skin Distance |
| T80% | Time to 80% on wash-out |
| T80%-r | Time to 80% on wash-out ratio |
| TCM | Total Curvature Metric |
| TE | Tris-EDTA buffer |
| TIC | Time Intensity Curve |
| TPk | Time to Peak |
| TPk-r | Time to Peak ratio |
| TRUS | Transrectal Ultrasound |
| TUNEL | Terminal deoxynucleotidyl |
| TV | Tumor Volume |

| | |
|---|---|
| $TV_x$ | Start of Tumor Volume Recurrence |
| V | Volt |
| VVD | Volumetric Vascular Density |
| $VVD_x$ | Start of Volumetric Vascular Density Recurrence |
| WIS | Wash-in Slope |
| WIS-r | Wash-in Slope ratio |
| WIWOS-r | Wash-in/Wash-out ratio |
| WOS | Wash-out Slope |
| WOS-r | Wash-out Slope ratio |

# CHAPTER 1:

# Overview of Cancer and Radiation Therapy

## 1.1 Cancer and the Role of Angiogenesis

It is expected that over 1.6 million new cases of cancer will be diagnosed in 2017 in the United States and over 12 million new cases worldwide, with an estimated number of deaths reaching over 600,000 and 7 million, respectively [1,2]. Cancer incidence and mortality increased significantly during the 20th century, most probably due to the surge in tobacco use and other health epidemics such as obesity, increased alcohol consumption, and poor western-type diets. While cancer rates have slowly declined since the 1990's with improved diagnostics, treatment, and healthier lifestyles, it is still the second most deadly disease in America, after heart disease, claiming 1 out of every 4 deaths [3].

Advancements in cancer diagnostics have improved the early detection of specific cancers, allowing physicians to provide treatment at earlier stages, increasing the probability of controlling tumor metastasis and malignancy. Additionally, technological advancements in cancer therapies (i.e. nanomedicines, immunotherapies) have improved the specificity and efficiency for tumor control [4,5]. While advancements in healthcare over the last 50 years have improved cancer survival rates, cancer has remained a worldwide epidemic.

Cancer arises when mutations in the DNA of normal cells result in aberrant cellular growth and function. Mutations can be caused by both environmental factors and genetic disposition, however recent data has shown that most cancers arise from random DNA copying "mistakes" [6]. Native cellular repair mechanisms will usually fix these mutations at various checkpoints in the cell cycle, or the cell will undergo apoptosis to prevent further mitotic divisions of the abnormal cell. Defects or mistakes made in these repair mechanisms may result in accumulation of mutations drastically increasing the probability of cancer [7].

Mutated cellular DNA can lead to the deregulation of cell signal transduction pathways, such as RNA transcription, protein synthesis, resulting in the inactivation or overactivation of certain cellular processes [8]. Usually these sorts of modifications result in increased proliferation of the aberrant cells and unsettles the balance of regulatory pathways that maintain homeostasis in the body. Hanahan et al proposed six "hallmarks of cancer" consisting of molecular characteristics of the tumor microenvironment that contribute to the development and proliferation of tumors, one of which is aberrant angiogenesis.

Normal angiogenesis is precisely regulated by the expression of pro-angiogenic and anti-angiogenic factors. In normal tissue, the balance between the expression of both factors is shifted towards anti-angiogenesis resulting in mostly quiescent blood vessels [9]. Rapidly proliferating tumor cells will eventually become hypoxic as they grow beyond the diffusion limit of oxygen with the existing vascular supply, thus straining the metabolic processes of the neoplasm [10]. This oxygen and nutrient starvation caused by hypoxia is a major driving factor in the upregulation of angiogenesis, resulting in a shift towards pro-angiogenic factors [9].

Tumor angiogenesis is characterized by aberrant, uncontrolled growth of new vasculature as a result of the upregulation of pro-angiogenic factors. The new growth is typically chaotic in

nature, resulting in excessive sprouting of disorganized, tortuous, and highly dense networks of vessels. While initially the newly stimulated angiogenesis increases oxygenation and nutrient delivery to a certain extent, the overall function of the tumor vasculature is deficient, suffering from leaky vessels and poor perfusion [11]. Further endothelial cell recruitment of pericytes ultimately results in the formation of premature vessels, as they are constantly bombarded with signaling factors preventing complete vessel maturation [12].

The rate and extent of angiogenesis varies by tumor type and the microenvironment conditions leading to tumors with a wide range of vascularity. The extent of tumor vascularity has significant implications on the growth of the tumor and the effectiveness of various treatment modalities, specifically chemotherapy and radiotherapy (RT). Chemotherapy (targeted or untargeted), typically administered intravenously, requires sufficient blood flow into the tumor region for maximum effect. In addition to increased vascular density and tortuosity, angiogenesis is often accompanied with tumor hypoxia and necrosis [13]. Tumor necrosis has been reported to correlate with levels of angiogenesis and poor prognosis of malignant cancer. Specifically, $\alpha_v\beta_3$ integrin, a key regulator in tumor angiogenesis is known to be associated with necrosis and apoptotic activity [14]. Therefore it is typical for tumors to develop necrotic and perinecrotic regions of the tumor. Since a higher density of vessels exist in the perimeter of the tumor, successfully delivering a sufficient concentration of drug throughout the entire tumor is difficult. New techniques that stimulate transient *increased* blood flow, such as “vascular promotion therapy”, assist in delivering the drug into the hypoxic regions of the tumor [15]. The opposing school of thought employs methods of reducing the tumor pro-angiogenic drive using anti-angiogenic drugs in order to stunt tumor growth and possibly induce tumor regression [16].

Usually, these techniques are used together with other treatment strategies such as radiation or surgical resection.

Similarly, presence of blood as an oxygen carrier increases the efficacy of RT by increasing oxygen radical formation, an indirect mechanism for radiation assisted cell death. Microvessel density and perfusion have been shown to be a prognostic factor of RT response. Previous studies have demonstrated the radioresistance of hypovascular/hypoxic tumors as well as the improvement in RT response with pro-angiogenic pre-treatment of the tumor prior to radiation. Other studies have proposed the delivery of secondary oxygen carriers via IV or intratumoral injection to increase oxygen concentration for increasing radiosensitivity [17].

## 1.2 Radiation Therapy and its Effect on Tumor Microvasculature

RT is one of the most basic forms of cancer treatment, used to treat approximately 50% of all cancer patients during their first course of treatment, and contributes to 40% of curative cancer treatment [18,19]. Approximately 40% of cancer patients are on at least their second course of RT, with rates of cancer resistance ranging from 20-30% for PCa, 10% for breast cancer, and as high as 90% for some types of lung cancer [20–23].

Although ionizing radiation has been used over 110 years for treating cancer, many facets of radiobiology are still not well understood. The most accepted theory of the radiobiological mechanism for cancer treatment using conventional radiation is the direct and indirect damage inflicted on cellular DNA. The specific chemical mechanisms for DNA damage are still being studied, but in general, DNA is affected by ionizing radiation in two ways. Ionizing radiation (photons or atomic particles) can directly pass through cellular DNA causing base-pair deletions,

or single and double-strand breaks. Although direct ionization occurs, it only accounts for a small contribution of the total DNA damage [24]. Ionization can also pass through the cellular membrane, interacting with aqueous molecules and forming reactive oxygen species (ROS) and free radicals. ROS and free radicals are extremely reactive (given their unpaired electrons) and readily attack covalent bonds of DNA, causing single and double-strand breaks [25]. This accounts for the majority of DNA damage (>80%) and is the most commonly accepted mechanism for cellular death. Cellular repair mechanisms (base excision repair) deal with base-pair deletions and single-strand breaks on a daily basis due to natural production of ROS and free radicals; however, repair of double-strand breaks is prone to errors and usually results in cellular apoptosis. Although some normal cell damage is inevitable during RT of cancer, it has been reported that highly proliferating cells such as cancer are more sensitive to radiation. Cellular death from radiation exposure occurs during the mitotic phases, therefore quickly dividing cells react sooner than healthy tissue [26]. The same phenomenon holds true for other quickly dividing cells such as epithelial and endothelial cells.

To date, the clinical standard for assessing radiation treatment response is a system similar to Response Evaluation Criteria in Solid Tumors (RECIST), where changes in tumor size indicate positive or negative treatment response [27]. Unfortunately, gross changes in tumor volume (TV) occur very slowly (weeks to months after treatment) and is a limitation especially when the tumor is not responding well to the treatment as early assessment of a failed treatment will allow physicians more time to switch treatment strategies. Advances in radiobiology over the last half-century had revealed that changes in TV are the result of a long cascade of intricate biological processes. Better understanding the effect of radiation on various tumor microenvironments will enable us to further improve patient outcomes either by better and faster

assessment of response to therapy, improving the effectiveness of adjuvant therapies, or developing more advanced methods of RT. One such microenvironment, the tumor microvasculature, has been known to be significantly affected by radiation, resulting in a series of molecular changes that result in tumor cell death and control [28]. Endothelial apoptosis of tumor microvasculature is known to be a homeostatic factor in the regulation of tumor growth and is strongly correlated with tumor control when treated with radiation, therefore suggesting that DNA damage and consequential cell death due to exposure to ionizing radiation may not be the only significant factor determining the effect of RT [29]. Better understanding the complex mechanisms behind the microvascular response to radiation may enable a better understanding of overall tumor response to treatment, allowing for improved treatment planning.

Immediate changes in tissue perfusion as a result of cancer treatments have been closely studied and documented previously. In the context of RT, many studies have observed changes in vascular function in both clinical and pre-clinical studies. Park et al reported in an extensive review that lower dose treatments (<10 Gy) induced mild vascular damage, while larger doses (>15 Gy) resulted in significant vascular damage that was reflected in both vessel density and perfusion [30]. Long term vascular changes in higher-dose scenarios have been largely consistent. In another study, it was reported that 10 Gy radiation induced an increase in perfusion immediately after radiation, and then a significant decrease in perfusion 26 hours post treatment. Perfusion returned to normal levels 7-11 days after treatment [31]. Others have reported similar trends in blood perfusion: a sudden hyper-perfusion, followed by a sudden hypo-perfusion, and then gradual return to normal perfusion levels.

The correlation of these relatively short-term response trends to long-term outcome is an interesting question. Several studies have suggested that initial tumor vascular response may be a

predictor of long-term treatment response. It was reported by that immediate vascular volume and perfusion changes following high dose (>10 Gy) RT precede long term outcomes. Specifically, a marked increase in perfusion and neovascularization was a potential predictor of long-term tumor regrowth [32–34]. This was corroborated by Song et al, who also reported increased revascularization in tumors that regrew 15 days after 30 Gy treatment [30]. Interestingly, Maeda et al demonstrated early microvascular changes (within just 2 days) in response to a single dose of radiation in a mouse optical window chamber model suggesting that the tumor microvasculature is a highly dynamic and responsive system [35].

In addition to functional changes in tissue microvasculature, previous studies have reported changes in vessel structure in response to RT. Specifically, Bullitt et al demonstrated the use of vessel segmentation and tortuosity calculations from magnetic resonance angiography (MRA) images of the brain and correlated radiation treatment outcome with vascular normalization [36]. It was observed that increased tortuosity was associated with tumor recurrence, suggesting that the analysis of vessel shape may be an important biomarker for assessing treatment response.

# CHAPTER 2:

# Overview of Cancer Imaging

## 2.1 Modalities for Cancer Imaging

Cancer can be diagnosed using a variety of techniques including blood tests, physical examination, tissue biopsy, genetic tests, and imaging. Technology is rapidly improving in all of the diagnostic areas whether it is the development of antibodies that are more specific to blood serum antigens or advancements in Next Generation Sequencing/High-throughput Sequencing for personalized cancer screening [37–39]. Radiology plays an important role in the multidisciplinary approach to cancer diagnosis and disease management; it has dominated the area of cancer diagnostics for over half a century due to its non-invasiveness, standardized techniques, and versatility in application. Imaging is applied in a number of ways in oncology, including routine screening, biopsy guidance, and treatment monitoring to name a few. Nearly every imaging modality is currently used in cancer diagnosis (ultrasound, computed tomography (CT), magnetic resonance imaging (MRI), positron emission tomography (PET), single photon emission computed tomography (SPECT), bone scans, Optical Coherence Tomography (OCT), each with its unique strengths and weaknesses [40–42].

Anatomical imaging is best used for identifying solid masses in the body and is most commonly used in the clinic. Imaging modalities commonly used for anatomical imaging include ultrasound, MRI, and CT. Often a combination of these imaging modalities will be used

depending on the type and location of the tumor. Traditional grayscale ultrasound imaging is useful for imaging soft tissue tumors with high sensitivity which may otherwise be difficult to see with x-ray imaging. It is a real-time imaging modality, inexpensive, and globally accessible. CT and MRI excel at allowing physicians to perform 3D full body imaging of the body to visualize location, morphology, and size of lesions [43].

Functional imaging adds an additional dimension to cancer diagnosis by offering information regarding the molecular activity of the cancer. Two examples include PET and SPECT imaging, which can be used to identify regions of abnormal molecular activity (e.g. localized increase in radiolabeled glucose uptake is indicative of cancer). While PET and SPECT have high sensitivity and specificity to the radiolabeled compounds that are used for imaging, they lack resolution and anatomic detail. Development of multimodal imaging techniques, such as PET-CT or PET-MRI have made it possible to visualize anatomical and functional information simultaneously [43]. The fusion of anatomical and functional imaging has been the backbone of image aided cancer diagnostics, and the same theories can be applied to assessing cancer response to therapy as well.

## 2.2 Imaging for Assessing Response to Therapy

The long standing standard for assessing treatment response is quantifying changes in the size of the tumor mass. Since tumor measurements can be easily performed serially and noninvasively with traditional imaging modalities, imaging is typically the preferred method for assessing response to treatment. Traditionally, uni-dimensional or bi-dimensional measurements taken in the axial plane are used to represent tumor size; however, more recent studies have

demonstrated that volumetric measurements may provide a more accurate assessment. The Response Evaluation Criteria in Solid Tumors (RECIST) was published in 2000 as a guide of international standards for assessing tumor response to therapy using medical imaging, specifically CT and MRI. It is commonly used by physicians on a daily basis as part of their treatment monitoring (which also includes symptom surveillance and other tests). RECIST categorizes lesions as measurable and non-measurable. Measurable lesions are >20 mm on chest x-ray (or >10 mm on spiral CT) [27]. Measurable lesions are further categorized as complete response, partial response, stable disease, or progressive disease based on percent increase or decrease of the sum of the largest diameters. Non-measurable, or non-target lesions are also categorized as complete responders, stable disease, or progressive disease based on their disappearance or persistence, or the appearance of new lesions.

The advancement of new cancer drugs and targeted treatment strategies has warranted the development of a new method of assessing tumor response. At the time RECIST was published, many of the chemotherapeutics used were cytotoxic drugs which functioned by directly killing cancer cells. Therefore, a change in the number of cancer cells was represented by a change in the TV. New treatment strategies, such as anti-angiogenic drugs, or drugs that inhibit cancer cell proliferation by interrupting relevant cell signaling pathways, do not directly kill the cancer cells yet have still demonstrated sufficient tumor control and disease management [44]. Considering the effects of these new types of treatments requires a different biomarker that looks beyond the size of the tumor.

Nuclear medicine (PET and SPECT) and contrast imaging techniques for MRI, CT, and ultrasound have proven useful in assessing molecular changes and changes in physiological function. For example, FDG (Fluorodeoxyglucose) PET is the most commonly used radionuclide

for PET imaging to assess glycolytic metabolism of the tumor [45]. PET is often coupled with an anatomical imaging modality such as PET-CT or PET-MRI which registers the molecular (functional) information with the anatomy.

Dynamic contrast-enhanced CT and MRI enable quantification of contrast perfusion in the tissue of interest [46]. Depending on the type of therapy, blood perfusion in the tumor may be expected to increase or decrease. For example, a decrease in tumor perfusion might be expected after the delivery of an anti-angiogenic drug. Changes in tumor metabolism and blood perfusion are two of many alternative biomarkers that can be used for assessing response to therapy that may paint a more accurate picture of treatment effects than TV.

As discussed previously, angiogenesis plays a crucial role in tumor development and the resulting tumor vasculature has distinctive characteristics such as increased tortuosity, density, and permeability. Angiogenesis can be quickly triggered in response to physiological stimuli such as inflammation and hypoxia [47]. Since these changes have been shown to occur much sooner than the physical growth of the tumor mass itself, the ability to assess microvascular changes related to a particular disease would potentially increase the sensitivity of diagnostics and improve disease management.

## 2.3 Medical Ultrasound Imaging

Apart from x-ray imaging, ultrasound imaging is the oldest, most fundamental imaging modality used in medicine. There are many advantages of using ultrasound over other imaging techniques, such as MRI and CT. Ultrasound is a non-ionizing imaging technique and when used within clinical parameters, produces no adverse bio-effects. It is highly portable with a footprint

of less than 1 $m^3$, and requires just a small consult room. Recent advancements in ultrasound instrumentation have condensed the size of an ultrasound scanner to the size of a table or phone--in fact, there are now ultrasound apps that are available for the iPhone. This is in contrast to CT, MRI, and nuclear imaging, which require significantly more expensive equipment and dedicated facilities to house the scanners. These large imaging rooms are usually equipped with a procedure room and an external control room so that interference from ionizing radiation or magnetic fields do not affect bystanders or other unprotected equipment. Ultrasound is also significantly inexpensive. Standard diagnostic ultrasound and chest x-ray cost $150-300, while MRI, CT, and nuclear imaging can cost anywhere from $500-$2,500 depending on the application (prices based on no insurance coverage) [48].

Medical ultrasound is most commonly used for anatomical imaging. Unlike the full-body imaging capabilities of CT and MRI, ultrasound has an extremely limited field of view of ~2-7 cm laterally, and 15-20 cm axially. However, ultrasound offers higher resolution, anywhere from 100-1000 μm depending on the desired frequency and application. In terms of cancer imaging, traditional brightness mode ultrasound (b-mode or gray-scale ultrasound) can detect abnormal lesions with high sensitivity, however it has low specificity in lesion subtyping or assessing malignancy [49]. It is also difficult to visualize blood with conventional ultrasound, and standard Doppler techniques are limited and unable to detect smaller vessels due to limited scattering of blood components and a low impedance mismatch between blood and the surrounding tissue.

To improve the imaging specificity to tissue vasculature, a contrast agent is typically used. For example, iodinated or gadolinium based contrast agent is intravenously injected for contrast CT or MRI imaging, respectively. Similarly a microbubble contrast agent can be used

for contrast enhanced ultrasound imaging (CEUS) which provides sufficient contrast between blood and the surrounding tissue.

## 2.4 Ultrasound Contrast Imaging

Microbubble contrast agents are composed of an inert, high molecular weight gas core stabilized by a phospholipid or albumin shell. Other molecules may be incorporated with bubble shell. For example, polyethylene glycol (PEG) is often incorporated into lipid shell microbubbles, which acts as a stealth agent, reducing its visibility to the reticuloendothelial system. The bubbles are on the order of 1-3 μm in diameter, roughly the size of red blood cells [50]. This means that once introduced into the vascular supply, they remain strictly an intravascular contrast agent. This is in contrast to gadolinium and iodine based contrast agents for CT and MRI, which eventually diffuse out of the vasculature. As a pure intravascular agent, the microbubbles increase the specificity of microvessel detection using ultrasound. The half-life of the bubbles is on the order of 3-5 minutes, depending on the organism that is being imaged; for humans, it is approximately 3 minutes. The shell components are cleared by the body through the liver and spleen, while the core gas is transferred out through the lungs and simply breathed out.

Microbubbles possess very interesting properties which enable high contrast-to-tissue vascular imaging. Since the core of the bubble is gaseous, the acoustic impedance mismatch between the tissue/blood and microbubbles is very high, resulting in increased ultrasound scattering [51]. Further, the gas core expands and contracts as it is interrogated by an ultrasound pulse, resulting in a non-linear, harmonic oscillations, in contrast with highly linear tissue

reflections centered at the fundamental frequency with weak higher harmonic signal. Various ultrasound algorithms take advantage of the non-linear oscillations for contrast imaging. For example, pulse inversion is a technique where two consecutive pulses (the second pulse is inverted) are transmitted such that their echoes are summed, subtracting the odd harmonics and summing the resultant even harmonics [52]. This effectively removes the linear fundamental frequency, while retaining the non-linear, harmonic (primarily 2nd order) signals.

CEUS has been used heavily in echocardiography, and in the last decade, techniques such as perfusion imaging and molecular imaging have been tested in preclinical and clinical settings in a variety of organ systems and cancer types [50]. While the applications of CEUS are seemingly ubiquitous, the resolution of typical CEUS imaging schemes are limited and differentiation of individual vessels cannot be achieved. The ability to resolve small vessels allows for further quantification of the vascular environment within a tissue, such as vascular density and morphology. With traditional CEUS imaging, it is difficult to discern increases in contrast intensity as a function of increased microvasculature or local increase in perfusion. Higher ultrasound frequencies (>15 MHz) are required for higher resolution imaging, however the microbubble contrast agents resonate most effective when excited at low frequencies (microbubble resonance is approximately 1-5 MHz) [53]. Interestingly, the response of microbubbles when excited at low frequencies is significantly broadband relative to the surrounding tissue, and can produce energies that can be detected at high frequencies greater than 30 MHz [54,55]. The ability to excite microbubbles at their resonance frequency and receive super-harmonic content would enable significantly higher resolution CEUS.

# CHAPTER 3:

# Overview of High-Resolution CEUS

## 3.1 Acoustic Angiography

Acoustic Angiography (AA) is CEUS imaging technique developed by the Dayton Lab at the University of North Carolina at Chapel Hill that implements the concept of superharmonic imaging, which utilize the broadband microbubble response for high-resolution microvascular imaging [56].

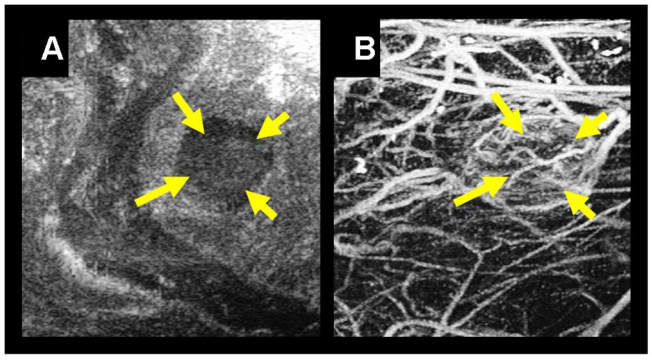


Figure 3. 1. Acoustic Angiography and B-mode images. A) B-mode image in the coronal view of a tumor located in the right flank of a rat indicated with yellow arrows. B) A coronal maximum intensity projection of 3D intensity data from a stack of 2D AA images in the same imaging area. Using AA we can visualize the tumor tissue and microvasculature with exceptional tissue rejection.

In this method, a low frequency transmit pulse at a moderate pressure (0.6-1.0 MPa) is delivered around the resonance frequency of the microbubble. The resulting broadband

microbubble response spans as high as the 8-10th order harmonics. The lower harmonics (mostly containing tissue signal) are filtered out using a high-pass filter. Since such broadband transducers do not exist that can perform both a low frequency transmit and a high frequency receive, a prototype confocal dual-frequency transducer was developed containing a low frequency (1-4 MHz, close to microbubble resonance) outer ring element for transmission and a high-frequency (25-30 MHz) inner element for receiving (Figure 3.2). The large bandwidth separation of the transmit and receive frequencies enables the detection of broadband microbubble signals while rejecting linear tissue signal. AA is significantly more sensitive to microbubble contrast agents resulting in a high contrast to tissue ratio (CTR) of up to 20 dB, and because such a high receiving frequency is used, the resolution is approximately 100-200 μm, higher than conventional contrast imaging techniques [54].

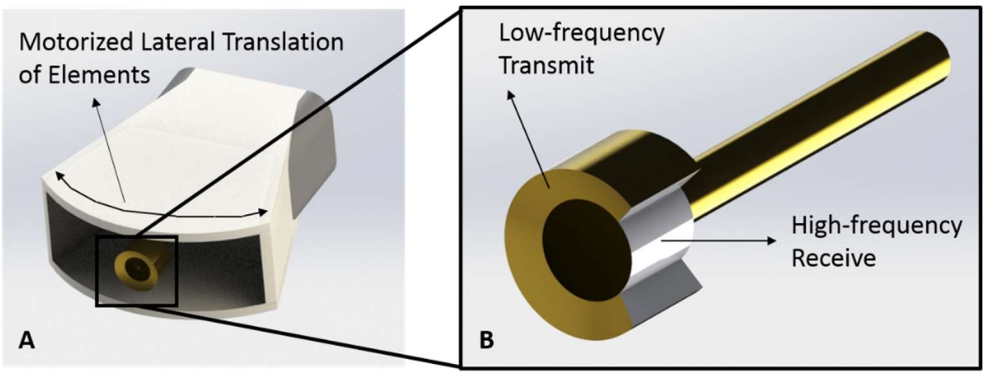


Figure 3. 2. The RMV prototype dual-frequency probe used for AA imaging. The low-frequency annulus is used for transmission, and the high-frequency inner element is used for receiving. The transducer "wobbles" laterally to produce a curvilinear type ultrasound image.

### 3.2 Vascular Metrics Derived from Acoustic Angiography

A stack of 2D images acquired by translating the ultrasound probe in the elevational dimension can be constructed into a 3D visualization of tissue microvasculature. There are several vascular metrics that can be derived from AA 3D data. Using the grayscale 8-bit raw intensity data, thresholding algorithms can be used to filter out weak microbubble contrast signal from slow-flowing unresolvable vessels, below the resolution limit of AA and binarize the remaining resolvable vessels (>100 μm) -- this is performed over the entire 3D volume. For instance, volumetric vascular density (VVD) can be measured with the binarized image by summing the number of pixels above the grayscale threshold and dividing by the number of pixels within the user defined region of interest (ROI) encompassing the tumor region [57].

Individual resolvable vessels can also be segmented using specialized segmentation software, which generates an array of 3D vectors representing the tubular centerline for each vessel enabling quantitative morphological assessment. As discussed previously in section 2.1, tumor vessels are often characterized as highly tortuous. Using AA and segmentation methods, we calculate vessel tortuosity using three metrics: distance metric (DM), sum of angles metric (SOAM), and total curvature metric (TCM) [58]. The DM is calculated by dividing the length of the extracted vessel path by the length of the end-to-end vessel secant. The SOAM is calculated by integrating the angular changes throughout the centerline of the vessel, divided by the length of the extracted vessel path. TCM is calculated by summing the total curvature of the vessel and dividing by total path length [58]. All three metrics are complementary to describing vessel tortuosity—for example, SOAM and TCM are more sensitive to tightly coiled vessels.

Tumor necrosis (or severely hypovascular regions) can also be detected and quantified. As discussed previously, tumor necrosis has been shown to correlate with angiogenesis and poor

prognosis. By reducing the frame-rate of imaging, we can increase our sensitivity to microbubble signal, including signals from smaller, slow flowing vessels (Figure 3.3). This results in an image similar to conventional CEUS, however the increased resolution and contrast sensitivity allows us to draw precisely defined lines of regions of necrosis and calculate percent necrosis (PN). Using a slower frame-rate image, we apply the same binarization algorithm used for VVD calculations and count the pixels below the grayscale threshold.

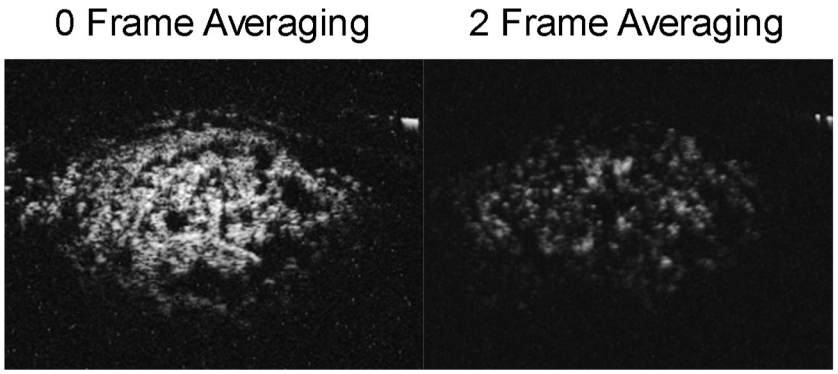


Figure 3. 3. The effect of frame averaging on AA images. The AA image on the left was acquired without frame averaging. Contrast signal from microvessels below the resolution limit can be detected. In this way, areas of no perfusion (considered severely hypoxic or necrotic) are easily discernable and can be extracted and measured using basic image processing. The image on the right is after 2 frame averaging. The signal intensity is significantly lowered since signal from small, slower flowing vessels is averaged out between frames. The result is that individual vessels can be visualized during 3D reconstruction.

## 3.3 Prior Studies with Acoustic Angiography

Previous work has largely focused on demonstrating AAs ability to quantify statistical differences in vascular tortuosity and density between normal and cancerous tissue. Gessner et al published results using segmented vessel tortuosity analysis from 438 vessels that demonstrated an increase in both DM (23.76% higher) and SOAM (50.73% higher) in rat fibrosarcoma (FSA) tumors compared to normal tissue [59]. Shelton et al later demonstrated that AA alone could

detect statistical increases in DM and SOAM in tumors as small as 2-3 mm [60]. This established the detection of "pre-palpable" tumors using quantification of microvascular features alone.

The work discussed in this dissertation builds upon this previous work and extends the application of AA to assessing tumor microvascular response to treatment, specifically RT. We investigate the quantification of various vessel features and evaluate their sensitivity to microvascular changes with the intent of developing a predictive measure of successful or unsuccessful response to treatment.

# CHAPTER 4:

# AA for Assessing Tumor Microvascular Response to RT[1]

## 4.1 Overview

Previously we have demonstrated the ability to discriminate healthy from cancerous tissue solely by quantifying abnormal microvasculature using AA. As tumors develop, their microenvironment become denser with tortuous and leaky vessels. Additionally, quickly growing tumors become hypoxic resulting in regions of severe hypovascularity and necrosis. We hypothesize that changes detected in the tumor microvascular microenvironment using AA in response to RT are correlated with long term survival. In this study, we longitudinally performed AA imaging on tumor bearing rats treated with a single dose of RT, measured five tumor vascular features at each time point, and determined the correlation with long term survival compared with TV measurements.

[1] This chapter previously appeared as an article in the Journal of Theranostics. The original citation is as follows*: Kasoji SK, Rivera JN, Gessner RC, Chang SX, Dayton PA. Early Assessment of Tumor Response to Radiation Therapy using High-Resolution Quantitative Microvascular Ultrasound Imaging. Theranostics. 2018;8(1):156-168.*

## 4.2 Materials and Methods

### *4.2.i Rat and Tumor Models*

All animal surgical and imaging procedures were reviewed and approved by the University of North Carolina at Chapel Hill Animal Care and Use Committee prior to conducting this study. Rat FSA tumor tissue was subcutaneously implanted in the right flank of 30 female Fisher 344 rats as previously described [61]. Rat FSA was originally induced and isolated from Fisher 344 rats injected with the carcinogen, methylcholantrene [62]. Rat FSA is characterized as a local, non-metastasizing tumor that is highly vascular and oxygen dependent [62,63]. Because of its high vascularity, it is an appropriate tumor model for AA imaging after RT, since we are specifically interested in the tumor vascular response to therapy. Because rat FSA is oxygen dependent, avascular regions typically undergo tissue necrosis [63].

### *4.2.ii RT and Monitoring*

Once the tumors reached their target treatment size of 5-10 mm in diameter in the longest dimension of the sagittal plane, the tumors were given a single dose of radiation. The rats were split into four different dose cohorts and received either 0 Gy (treatment control, n=9), 15 Gy (n=8), 20 Gy (n=5), or 25 Gy (n=8) of radiation. The dose levels were determined during a longitudinal pilot RT study (unpublished) that was conducted at 0, 5, and 20 Gy. We found that 5 Gy had no tumor control, and 20 Gy had roughly 50% complete response (tumor shrinkage and eventual disappearance) and 50% partial response (initial tumor shrinkage followed by a delayed tumor regrowth). We selected a dose level of 15-25 Gy as it allowed us to investigate the dose

dependent correlation between TV change and microvascular change for both complete response and partial response groups with similar statistics.

The rats were anesthetized using vaporized isoflurane and oriented in the left lateral recumbent position on a heating pad throughout the duration of the treatment with front and rear paws stabilized on the heating pad with medical tape. Positioning was performed using a rotatable rat positioning table (VisualSonics, Toronto Canada) so that the tumor was completely irradiated while minimizing exposure to the abdominal region (Figure 4.1). The rats were treated with a Primus II clinical linear accelerator (Siemens Healthcare, Malvern, PA) with a dose prescription of 6 MV photons, 2 cm x 2 cm collimated radiation field size at 100 cm source-to-skin-distance (SSD), and 1 cm of water-equivalent build-up material. All rats were monitored daily for the first 2 weeks following treatment, and then every third day thereafter. Additionally, the animals were all fed identical diets consisting of regular protein pellets and both calorie-rich and hydrating gels to mitigate excessive weight-loss and water-loss due to dehydration in the case of intestinal distress caused by radiation enteritis.

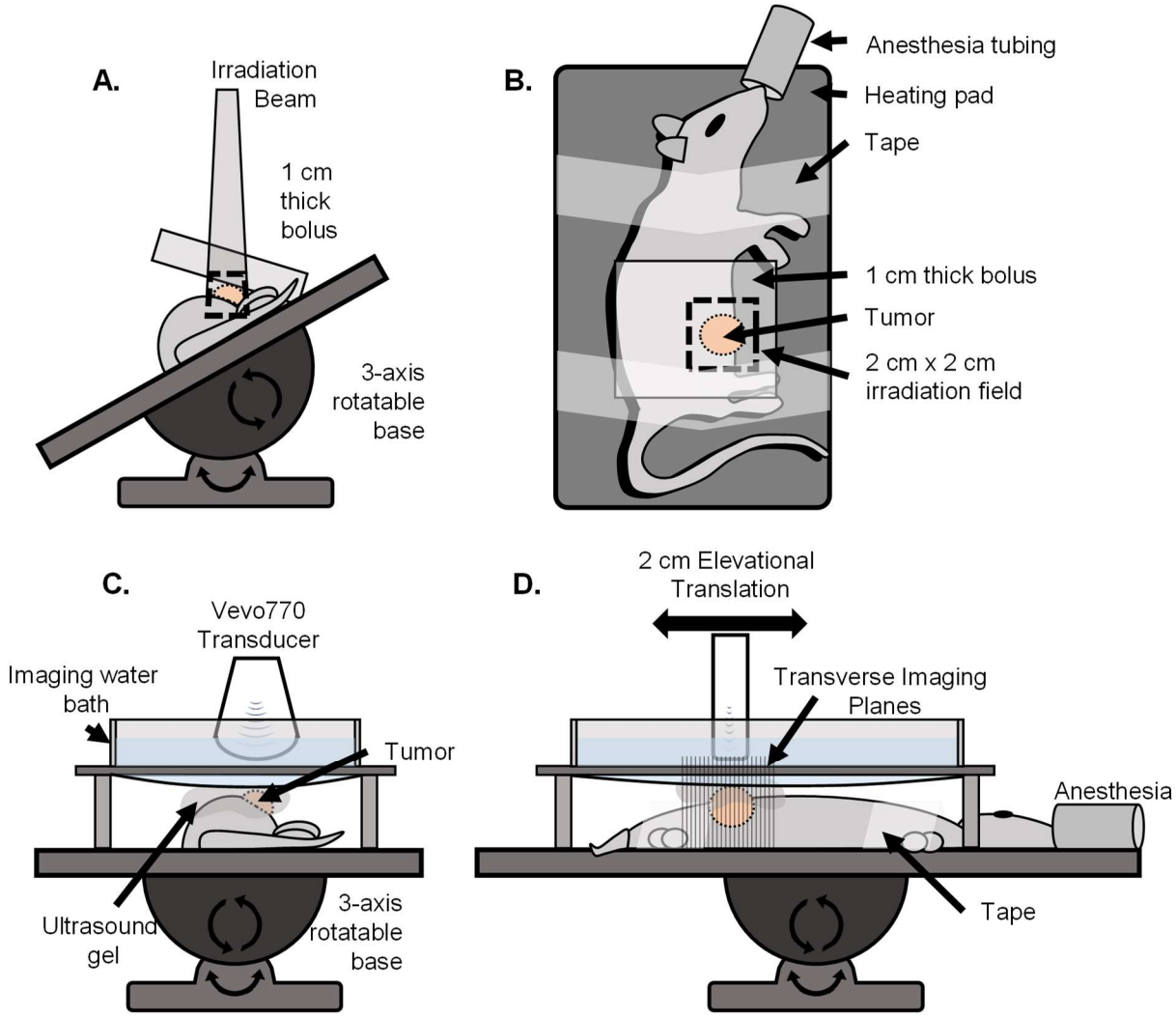


Figure 4. 1. Setup used for irradiation and ultrasound imaging. A) (Front view) For irradiation, the rat was positioned on a heating pad mounted to a 3-axis rotatable base. The heating pad was rotated to an angle such that irradiation beam was centered on the tumor while minimizing exposure to the abdominopelvic region. The 1 cm water-equivalent bolus was then placed on top of the tumor region. B) (Top view) The rat was secured to the heating pad using medical tape. A 2 cm x 2 cm irradiation field size was used. C) (Front view) For imaging, the rat was positioned on the same heating pad, oriented parallel to the floor such that the tumor was facing up. A custom designed water bath was used to separate the transducer from the gel while still being continuously coupled to the tumor, so that the mechanical translation of the transducer would not displace the gel causing decoupling and introducing air bubbles. D) (Side view) The transducer was mechanically translated in the elevational dimension for 2 cm for each scan.

### *4.2.iii Imaging Procedure*

Rats were imaged immediately prior to radiation for baseline measurements. After the radiation treatment, imaging was performed daily for 3 consecutive days and then every 3 days for approximately 30 days or until the tumors reached the maximum size of 2 cm in the longest diameter.

During each imaging session the rats were anesthetized using vaporized isoflurane and positioned on a heating pad as described above. A tail vein IV catheter was inserted for constant microbubble contrast infusion during AA imaging. Microbubble contrast agents were prepared in-house using sterile techniques, as previously described [61]. The contrast was diluted with 0.9% sterile saline in a 1:1 ratio. The contrast agent was administered as a small bolus of 50 μL immediately followed by a constant rate of infusion of 40 μL/min using a pre-clinical infusion pump. Contrast was infused for 30 seconds before imaging was initiated to allow contrast flow to achieve a steady state and then was continued for the duration of the imaging scan. A total contrast volume of approximately 180 μL was injected for one AA scan. The tumor region of the rat was shaved and depilated and ultrasound gel was applied onto the tumor region for ultrasound coupling. A custom imaging bath was used for all imaging to minimize gel decoupling during mechanical translation of the transducer (Figure 4.1). All imaging was performed on a Vevo 770 pre-clinical ultrasound scanner (VisualSonics, Toronto, ON, Canada) with a custom prototype dual-frequency transducer modified from a VisualSonics RMV707 probe, as previously described [64]. This transducer utilized a 4 MHz transmitter and a 30 MHz receiver, and was mechanically swept to acquire 2D images, and then translated in the elevational axis to acquire 3D data. A b-mode (anatomical) image volume was acquired over a 2 cm region, followed an AA scan over the same region. The elevational step size for each image was 100 μm. Two-frame

averaging with a frame rate of 3 frames/second was used for all AA imaging to improve the signal-to-noise ratio for producing optimal images.

### *4.2.iv Image Analysis*

The b-mode images were used to calculate TV. The caliper feature on the Vevo 770 imaging software was used to measure the longest tumor diameter in each image axis to approximate the ellipsoidal volume of the tumor. The AA images were post-processed using MATLAB (MathWorks, Natick, MA), TubeX, and VesselView to measure VVD, PN, and vessel tortuosity through the SOAM, DM, and the TCM [65,66].

It is important to identify and remove large hypoechoic regions to not overestimate the total perfused tissue volume [67,68]. We assumed that large hypoechoic regions were due to necrosis and hypoxia, based on tumor ex vivo observations and prior literature that describes rat FSA as a highly oxygen dependent tumor [63]. These hypoechoic regions will be referred to as "necrotic" for simplicity, which encompasses necrotic and perinecrotic regions. For identifying necrotic regions, a de-noising 2D median filter was applied to each frame of the AA image slices to smooth the image and then a threshold was used to create a volumetric binary mask which identified large dark regions. The ratio of the number voxels representing necrotic regions within the ROI and the number of voxels representing the entire tumor ROI was calculated as PN.

$$Percent\ Necrosis\ (PN) = \frac{\#\ voxels\ of\ identified\ necrosis}{\#\ of\ voxels\ in\ the\ tumor\ ROI}$$

The previous volumetric binary mask used for identifying PN was then reapplied to the original AA image followed by subsequent thresholding to identify the vessels using the local

Otsu threshold method [69]. VVD was calculated by dividing the number of voxels representing vessels by the number of voxels representing the tumor tissue sans necrosis (Figure 4.2).

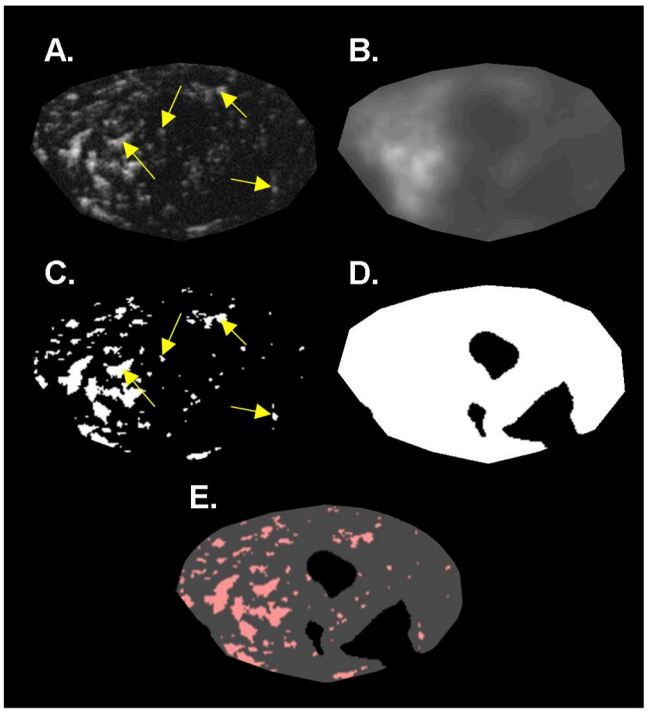


Figure 4. 2. Summary of the image analysis for calculating VVD. A single 2D slice of a 3D volume is shown in this figure. A) The original AA ROI. B) The original image, de-noised with a 2D median filter. C) The binary vessel image of the original ROI produced by applying an Otsu threshold. D) The hypoechoic mask made by applying a threshold on the de-noised image (B). E) The mask (D) applied to the binary vessel image (C). Arrows indicate resolvable vessels that have been converted into binary by thresholding.

For vessel tortuosity analysis, individual vessels were segmented using a custom segmentation software (Tubex) designed by Bullitt and Aylward et al which uses a ridge traversal method to extract tubular objects from 3D images [66]. Using the b-mode images, volumetric ellipsoidal ROIs were drawn encompassing the tumor and the surrounding tissue (each major axes was 1.5 times the radius of the measured tumor diameter). Only the tumor region and surrounding tissue was included in the segmentation analysis since including normal

vessels far from the tumor region reduces the sensitivity of detecting changes in tortuosity. The raw image ROI data was preconditioned into isotropic voxels prior to segmentation. The automatic, single vessel segmentation algorithm requires a manual definition of a seed point (performed by clicking a potential vessel in either the coronal or axial slice mode), which then automatically extracts the rest of the vessel by following the image intensity ridge representing the centerline of the calculated tubular structure (Figure 4.3). The algorithm performs a spatial up-sampling function which smooths the trajectory of each vessel. The radii of the vessel is also determined at each centerline point [66]. Initially for each image, approximately 100-200 vessels were segmented but were later filtered based on segment length to remove vessels that were too short to perform tortuosity metrics. A threshold vessel length of 500 points was used for all tortuosity analyses. The segmented data was imported into a second analysis software (VesselView) also developed by Bullitt and Aylward, which calculated SOAM, DM, and TCM (among other metrics) for each vessel.

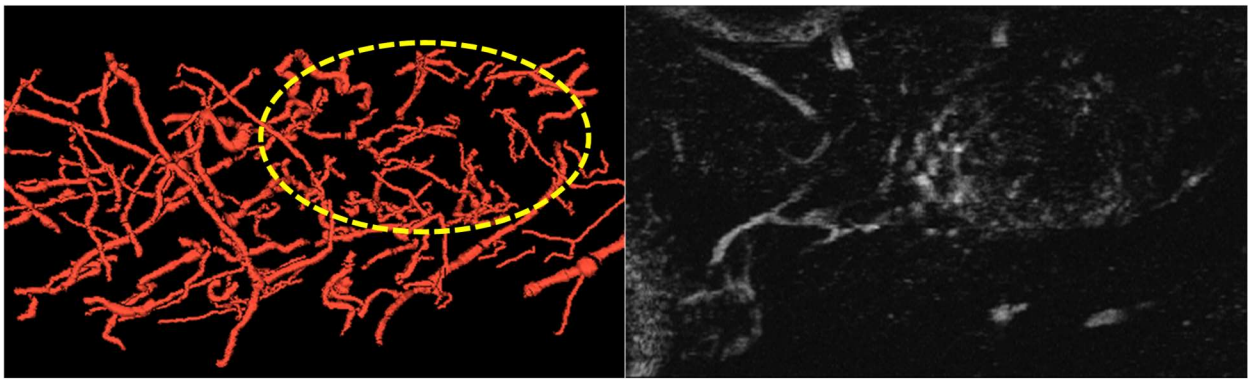

Figure 4. 3. An example of vessels segmented from an AA image. The yellow circle represents the location of the tumor, which is visible in the right AA image. The vessels inside the tumor are noticeably more bendy and irregular compared with the vessels far outside of the ROI.

### *4.2.v Data Analysis*

At the end of the study, treated rats were retrospectively categorized based on the treatment outcome as either partial response (initial treatment response followed by tumor recurrence) or complete response (full treatment response resulting in complete tumor disappearance). The 20 Gy study was terminated early at day 20 due to imaging schedule constraints. All complete responders were monitored for the duration of the study (30 days) for tumor regrowth, followed by an additional 30 days.

TV and all microvascular metric (MVm) (VVD, PN, SOAM, DM, TCM) growth curves for all individual rats were normalized by their respective baseline (pre-treatment) values. Initial TV growth curves (before tumor regression) and tumor recurrence rates were characterized by calculating their doubling times ($D_t$) using the equation:

$D_t = (T - T_0) \times (\log(2)/\log(V_f)) - \log(V_0)$ ($D_t$ – doubling time; $T_0$ – time of initial measurement; T – time of initial measurement; $V_0$ – initial volume; $V_f$ – final volume)

Similarly, TV regression was characterized by calculating the tumor halving times ($H_t$) using the equation:

$H_t = (T - T_0) \times (\log(1/2)/\log(V_f)) - \log(V_0)$ [70] ($H_t$ – halving time; $T_0$ – time of initial measurement; T – time of initial measurement; $V_0$ – initial volume; $V_f$ – final volume)

Different phases of the MVm (initial response, regression, and recurrence phases) were characterized using linear regression.

$TV_x$ represents the beginning of the recurrence phase identified using TV measurements for an individual tumor. Corresponding time points were labeled for each of the microvascular

metrics as well (labeled collectively as $MVm_x$). Statistical differences in growth curves and $TV_x$ and $MVm_x$ values were evaluated using the Mann-Whitney U-test, and differences observed between dose groups were evaluated with the Kruskal-Wallis test, followed by the Tukey Post-Hoc multiple comparison test ($\alpha = 0.05$). All statistical analysis was performed in MATLAB.

## 4.3 Results

### *4.3.i TV and VVD Results*

The treatment response statistics and sample sizes for each dose group are summarized in Table 1. Partial responders, complete responders, and untreated tumors in each dose group present distinctly different VVD and TV growth curves (Figure 4.4).

Table 4. 1 Treatment Response Statistics by Dose Group

| | **15 Gy** | **20 Gy** | **25 Gy** |
|---|---|---|---|
| **Partial Response** | 5 (63%) | 3 (60%) | 3 (38%) |
| **Complete Response** | 3 (38%) | 2 (40%) | 5 (63%) |
| **Total Treated Tumors:** | **8** | **5** | **8** |

Table 4. 1. Summary statistics of the treatment outcomes for each dose group. Partial response refers to tumors that initially responded but regrew and progressed, and complete response refers to tumors that completely disappeared after treatment.

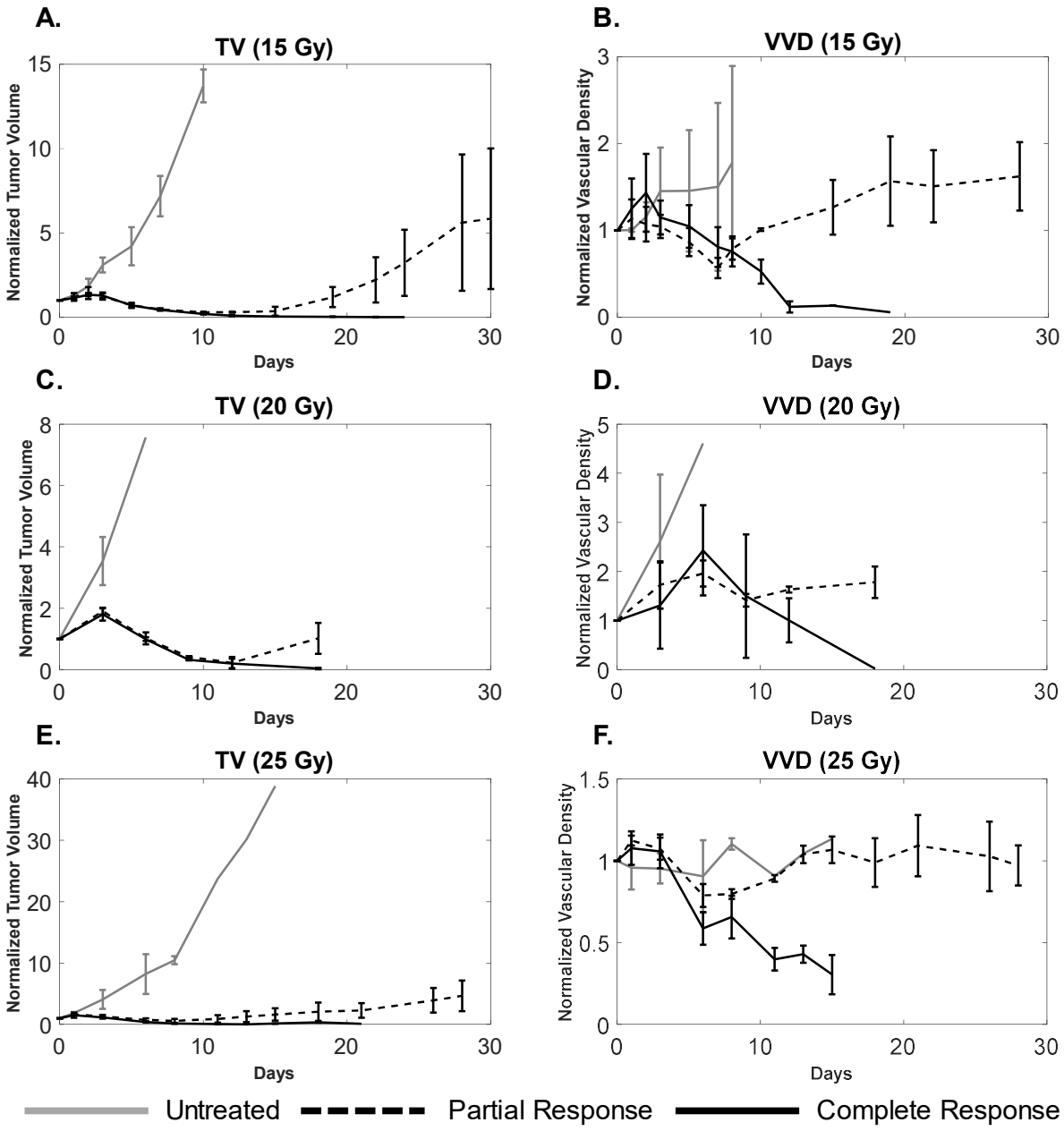


Figure 4. 4. A comparison of tumor volume (A, C, E) and tumor microvascular density (B, D, F) growth curves for complete responders (solid black), partial responders (dotted black), and untreated tumors (solid gray) for each dose group. Sample sizes for complete and partial responders, and untreated groups were 3, 4, and 2 for the 15 Gy group, 2, 3, and 5 for the 20 Gy group, and 5, 3, and 2 for the 25 Gy cohorts, respectively. Error bars represent standard deviation. Partial responders undergo a transient decrease in vascular density that correlates with tumor regression and eventually increases, correlating with tumor recurrence. For complete responders, both TV and VVD decrease. The large error bars in TV and VVD curves are expected due variability in tumor growth as well as heterogeneity of vascular supply.

*Initial Response*

Untreated tumors underwent normal, uninterrupted exponential volume growth with a mean doubling time of 1.9 ± 0.5 days (median: 1.9 days; range: 1.4 days; IQR: 0.6 days). All treated tumors presented delayed TV growth after the treatment (day 0) until day 3, at a growth rate significantly less ($p$=0.009) than compared to the untreated tumors with a mean tumor doubling time of 3.8 ± 2.6 days (median: 3.2 days; range: 11.7 days; IQR: 2.0 days). There was a non-significant decrease in the average tumor doubling time for treated tumors as RT dose increased. VVD of all treated tumors increased by an average of 18 ± 13%, significantly greater ($p$=0.023) than in untreated tumors, which increased by 4 ± 6%. There were no significant VVD or TV differences between partial and complete responders within each dose group (Table 2).

*Tumor Regression*

By day 5, all treated tumors experienced tumor regression where both TV and VVD decreased. There was no statistical difference in the regression rates of either TV or VVD between complete and partial responders in the 15, 20, and 25 Gy treatment groups. For complete responders, the tumors continued to shrink and completely disappeared between days 15 and 20, accompanied with decreasing VVD (Table 2).

Table 4. 2 Tumor Volume and Volumetric Vascular Density Growth Curve Statistics

| | Untreated | All Treated | 15 Gy | | 20 Gy | | 25 Gy | |
|---|---|---|---|---|---|---|---|---|
| | | | Complete Response | Partial Response | Complete Response | Partial Response | Complete Response | Partial Response |
| Tumor Volume Doubling time – Initial Response (days) | 1.9 ± 0.5 | 3.8 ± 2.6 *(p=0.009)* | 5.6 ± 3.4 | | 3.4 ± 0.5 | | 2.4 ± 1.4 | |
| | | | 5.5 ± 1.2 | 5.7 ± 4.7 | 3.6 ± 0.7 | 3.3 ± 0.3 | 2.3 ± 1.3 | 2.4 ± 1.9 |
| Volumetric Vascular Density increase – Initial Response (%) | 4.3 ± 6.1 | 18.1 ± 12.7 *(p=0.023)* | 21.0 ± 15.8 | | 26.5 ± 10.2 | | 10.0 ± 5.1 | |
| | | | 22.3 ± 21.3 | 20.5 ± 14.0 | 23.8 ± 15.3 | 28.3 ± 8.9 | 8.6 ± 5.9 | 12.4 ± 2.9 |
| Tumor Volume Halving time – Regression (days) | ~ | 3.0 ± 1.0 | 3.2 ± 0.7 | | 2.8 ± 0.3 | | 2.9 ± 1.4 | |
| | | | 2.5 ± 0.3 | 3.8 ± 0.5 | 3.0 ± 0.6 | 2.7 ± 0.1 | 2.1 ± 0.3 | 1.3 ± 1.6 |
| Volumetric Vascular Density Regression (%) | ~ | -12.8 ± 9.3 | -10.9 ± 4.9 | | -20.9 ± 14.7 | | -9.3 ± 5.0 | |
| | | | -10.4 ± 6.1 | -11.7 ± 3.5 | -26.0 ± 19.6 | -17.5 ± 14.1 | -11.1 ± 5.7 | -6.2 ± 1.0 |
| Tumor Volume Doubling time – Recurrence (days) | ~ | 4.7 ± 2.1 | 3.6 ± 0.8 | | 6.4 ± 3.4 | | 4.5 ± 1.2 | |
| Volumetric Vascular Density Recurrence (%) | ~ | 5.2 ± 3.2 | 7.2 ± 3.6 | | 4.7 ± 3.3 | | 3.2 ± 1.4 | |

Table 4. 2. Statistical analysis of tumor volume and volumetric vascular density growth curves for each dose group. Significant differences were observed in TV doubling time and VDD increase, immediately post-treatment. Treated tumors experienced delayed tumor growth (increased TV doubling time) immediately after treatment while VVD in treated tumors increased at a significantly higher rate than untreated tumors. There were no other statistically significant growth curve trends between treated and untreated, and complete and partial responders.

*Tumor Recurrence*

All partial responders rebounded and recurred between days 10 and 20 as indicated by their TV growth curves. VVD began to increase between days 7 and 11 and was also associated with tumor recurrence. Tumor recurrence occurred (non-significantly) earlier as dose increased as indicated by decreasing average $TV_x$; VVD recurrence (average $VVD_x$) was not statistically different between dose groups. When comparing TV and VVD curves for each individual tumor, the increase in VVD was observed earlier than the increase in TV (Figure 4.5). Figure 4.6 visually illustrates TV and VVD changes where VVD begins to increase while TV is still in the regression phase (Figure 4.6).

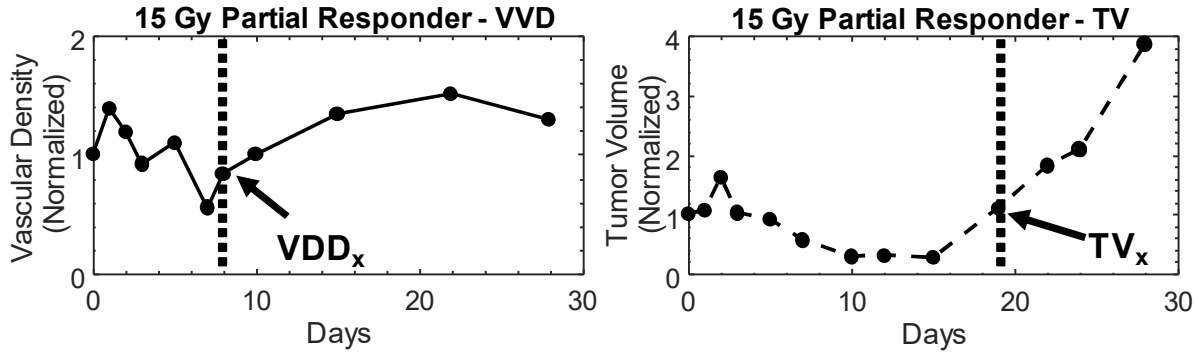


Figure 4. 5. Example of vascular density (left) and tumor volume (right) growth curves from a 15 Gy partial responder. All measurements were normalized to baseline values. In this particular partial responder failure, vascular density begins to increase as early as day 8, while tumor volume regrowth occurs later. The increase in the growth curve for both metrics demarcates the recurrence phase for partial responders, which is illustrated by the shaded region. The tumor volume and vascular density growth curves of partial responders in each dose group behaved similarly.

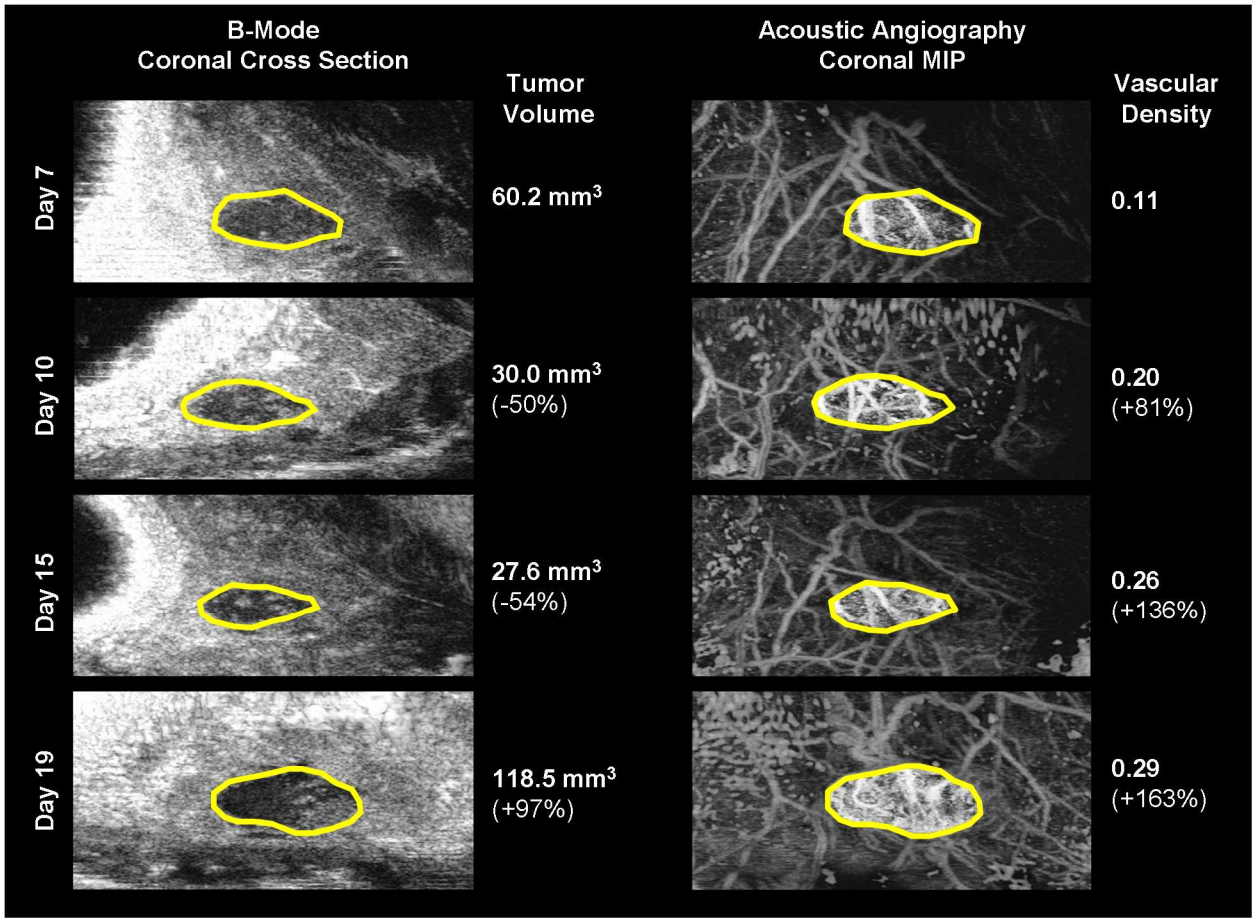


Figure 4. 6 A visual comparison of vascular density and tumor volume changes during the tumor regrowth phase of the same 15 Gy partial responder plotted in Figure 4. Vascular density (right) noticeably increases from day 7 to day 19, while tumor volume (left) size continues to decrease until day 19. The tumor boundary in the b-mode images is indicated by the solid yellow line. Note that microvascular data is shown as a maximum intensity projection but is actually a 3-D data set.

Increase in VVD for individual rats was observed 10.25 ± 1.5 days, 6 ± 0 days, and 4 ± 1.4 days earlier than increases in TV, in the 15 Gy*, 20 Gy*, and 25 Gy cohorts, respectively (Figure 4.7, *$p<0.05$). The initial TVs were 157.8 ± 5.9 $mm^3$, 182.9 ± 68.1 $mm^3$, 201.4 ± 77.4 $mm^3$, for the 15, 20, and 25 G groups, respectively. Variation in initial TVs between groups was due to tumor growth difficulties; specifically at the time of treatment, tumors either did not develop or grew too large (> 1 cm in diameter) to be continued in the study. There were non-

statistically significant differences in TV and VVD measurements between complete responders and partial responders; specifically, partial responders exhibited higher TVs and VVDs (Table 3).

Table 4.3 Average Initial TV and VVD Values

| Dose (Gy) | Average Initial TV ($mm^3$) (*p<0.05) | | Average Initial VVD (*p<0.05) | |
|---|---|---|---|---|
| | Partial Response | Complete Response | Partial Response | Complete Response |
| 15 | 171 ± 52 | 108 ± 40 | 0.25 ± .04 | 0.16 ± 0.10 |
| 20 | 230 ± 67 | 137 ± 110 | 0.26 ± 0.01 | 0.20 ± 0.05 |
| 25 | 290 ± 77 | 169 ± 39* | 0.27 ± 0.02 | 0.25 ± 0.04 |

Table 4. 3. Average initial tumor volume and initial vascular density values for each dose group. Larger initial tumor volumes were associated with partial response. While not statistically significant, the average initial vascular density for partial responders was greater than complete tumor response. This becomes less pronounced as dose increased.

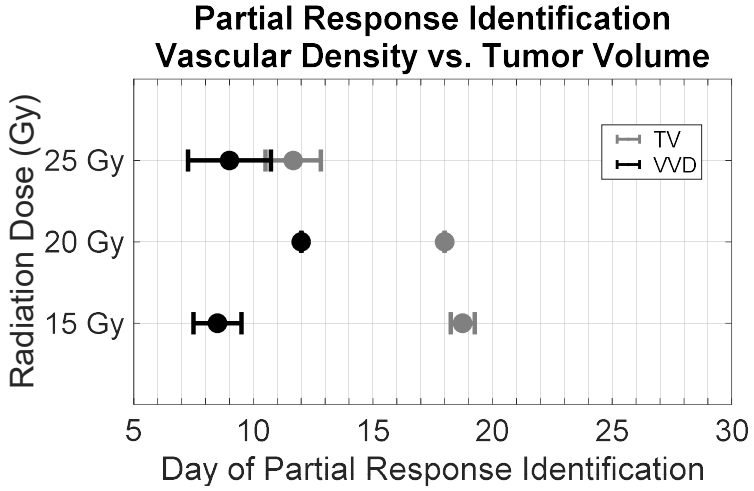


Figure 4. 7 Dose dependence of the early detection of treatment failure by tumor vascular density. Partial responder identification using vascular density (black) occurred earlier than using tumor volume (gray). With increasing dose, the difference in the time of identification between vascular density and tumor volume decreased. ([*] significant at $p < 0.05$).

No severe adverse health effects or significant weight loss were observed in any of the rats during the entirety of the study. The orientation of the rat during treatment minimized irradiation of the abdominopelvic region, resulting in less toxicity than in our previous studies where the rat was oriented perpendicular to the radiation beam. Mild radiation enteritis was experienced by less than 5 rats which resulted in loose stool and an average of 5 grams or 3% loss of body weight. This was mitigated with supplementary high calorie food and hydrogel water (Methods section). All rats with recurring tumors were euthanized at the end of the study. Rats with successfully treated tumors have been kept indefinitely (>180 days) since the end of the study and have not shown any signs of tumor recurrence.

### *4.3.ii PN, SOAM, DM, and TCM Results*

No significant differences in PN, SOAM, DM, and TCM growth curves were measured between partial responders, complete responders, and untreated controls at any time points. There were no dose dependent differences observed in any of the treatment groups. A summary of the growth curves is presented in Supplementary Figure C.1. There is an average increase in PN measured in the partial responders in all dose groups, however the average trends in PN for complete responders is inconsistent. Tortuosity measurements were compared at time points where VVD and TV clearly showed differences between partial and control responders, however no significant differences were found between groups. These data are summarized in Supplementary Figure C.2.

## 4.4 Discussion and Conclusions

We have previously demonstrated that AA can visualize microvasculature with high-resolution and various quantitative metrics are sensitive to certain abnormal microvascular structural properties (e.g. tortuosity, density) that allow us to discern cancerous tissue from normal tissue [59,60]. Based on previous research that has demonstrated that microvascular remodeling occurs within days after radiation exposure using optical imaging, we hypothesized that quantification of microvascular changes using AA may indicate response to therapy sooner than using TV alone, the current clinical standard for assessing response to treatment [35]. In this work we have demonstrated that quantitative AA is sensitive to changes certain microvascular features induced by RT and its feasibility as a tool for predicting treatment response.

We believe the clinical implications of our data are significant. In this tumor model, we have demonstrated that by quantifying the dynamic microvascular response to RT, tumor recurrence can be detected earlier than using TV measurements alone. In clinical practice, irradiated tumors often do not significantly change in size until 3-4 months after treatment and therefore post-treatment imaging is also not performed during this time [71]. For any cancer patient, early detection of cancer and early assessment of treatment response is critical for maximizing the chances for improving or maintaining quality of life. By decreasing the wait time between treatment and post-treatment evaluation, we may be able to increase the probability of successfully modifying an unsuccessful treatment strategy to one that is tailored to the patient. This is specifically important for RT, which by itself is often used with radical intent more than in a palliative setting.

The results in this study using a rat FSA model demonstrate that changes in VVD is a biomarker that presents differently in complete and partial responders in response to RT, and that

VVD regrowth associated with tumor recurrence in partial responders occurs significantly sooner than TV regrowth. In the tumors that present complete response, VVD and TV both decrease at similar rates until the tumor completely disappears.

We observe three phases after RT in both the VVD and TV curves, as described by Kozin *et al*: 1) initial treatment response presented by a continued increase in TV and VVD, 2) tumor regression phase presented by decrease in TV and VVD, and in partial responders, 3) tumor recurrence phase [72]. In the initial treatment response phase we observed an increase in VVD that occurred at a significantly greater rate than in untreated tumors, most likely due to short term inflammation and subsequent hypervascularization caused by the high-dose RT. This observation is supported by previous pre-clinical studies that observed hyperperfusion immediately after RT [30]. Days before TV recurrence ($TV_x$) is measurable in the partial responders, the tumors begin to undergo a rapid increase in VVD which can be visualized on imaging and quantitatively measured. While we do not have data supporting why VVD increases earlier than TV, prior evidence suggests that the tumor endothelium experiences stress induced expression of vascular endothelial growth factor (VEGF) and $\alpha_v\beta_3$-integrins, therefore evading cell death and possibly promoting revascularization and tumor cell proliferation [73,74].

In this study, we observed that the average TV in the partial responders was larger than the complete responders, in all dose groups, although the size difference was not significant due to variance. The increased likelihood of failure in RT treatment of larger tumors is consistent with radiation biology theory [75,76]. As expected, the TV threshold corresponding with complete response increased as a function of radiation dose (Table 3). We also observed that average initial VVD was greater in partial responders compared to complete responders; however, the differences were not significant and require further investigation (Figure 4.7).

Although a higher VVD at the time of treatment might be associated with an increase in tumor oxygenation and improved RT outcome, this hypothesis remains unanswered with conflicting reported results from previous studies [77]. Hypoxic tumors are known to be more radioresistant than normoxic tumors due to a number of reasons including the lower probability of reactive oxygen species produced by ionizing radiation forming fewer DNA strand breaks as well as the negative effect of hypoxia on the pathway for DNA damage repair resulting in a more radioresistant cell type [78]. While many previous studies have observed a positive correlation between VVD and therapeutic response, others have reported that VVD has no effect, or an inverse correlation with treatment response [77,79]. We speculate that in this particular tumor model, endothelial cells within the larger tumors, which inherently have a higher VVD, may undergo a smaller fraction of lethal radiation damage than smaller tumors and can eventually repair, possibly encouraging tumor regrowth. Due to the variability in tumor growth rates and unforeseen treatment scheduling complications, our initial size distribution was not comparable in all dose groups and is a confounding factor in explaining the effect of initial VVD on treatment outcome.

We observed earlier tumor recurrence with increasing dose; however, this requires further investigation. There are two possible explanations. First, as mentioned previously, the average initial (pre-treatment) TV was larger as dose increased, which may have resulted in a lower tumor cell kill fraction despite being treated with higher doses. Second, there is evidence that suggests that hypoxia induced by higher dose RT activates the unfolded protein response, protecting against hypoxia and resulting in the ability to more aggressively proliferate and metastasize [80]. However, further investigation is required to determine if FSA is affected by hypoxia induced stress.

We chose to use a simple, single high-dose fraction treatment to demonstrate feasibility of our imaging technique. Our dosage scheme was determined based on pilot study results (unpublished) of a longitudinal RT study performed at 0, 5, and 20 Gy in the same rat and tumor model. In the 20 Gy treatment group, approximately ~50% resulted in complete response. We chose doses between 15 and 25 Gy to investigate the TV and VVD differences between complete responders and partial responders while also determining any dose dependent responses. Conventional dose fractionation, or the division of the total radiation dose into multiple smaller doses over 7-8 weeks, is clinically used to reduce healthy tissue toxicity by allowing cellular repair in between successive treatments [81]. At this point, the effect of a dose fractionated scenario on tumor VVD is unclear and is an important, clinically relevant question that still needs to be answered. Our high-dose treatment conditions are more relevant to stereotactic body radiotherapy (SBRT) or stereotactic radiosurgery (SRS), and hypo-fractionated RT, which precisely deliver high dose radiation to the target tissue with just a single or few treatments [82]. Hypofractionation and SBRT/SRS, while relatively new and controversial in the field of RT, are promising techniques that may reduce toxicity while improving tumor control [82–84]. The results from this initial study motivate us to conduct further investigation under experimental conditions closer to more clinically relevant applications that incorporate conventional and hypo-fractionated RT.

The microvascular changes observed in this study are specific to the Fisher 344 rat FSA tumor model. Since this tumor strain has been shown to be highly oxygen dependent we made an assumption that areas of hypovascularity (hypoechoic regions) represented necrotic and perinecrotic regions [63]. The motivation for removing the hypoechoic regions was to prevent overestimation of the perfused tissue volume. However, histology was not performed to confirm

the hypoechoic regions as necrotic/perinecrotic to validate our analysis. This can be performed in future studies using the TUNEL assay and haemotoxylin and eosin staining [85].

As mentioned previously, tumor hypoxia and necrosis play an important role in tumor response to radiation [17,80]. However, no significant correlation between tumor necrosis and regrowth was observed. The reason for this may be two fold. First, tumor recurrence may not necessarily separate partial from control responders based on malignancy. Rather the data suggest that initial tumor size likely plays a role in treatment failure. While recurring tumors may develop necrotic regions, complete responding tumors are rapidly dying and exhibit loss in vascularity. Since PN is a fraction of the TV, any necrotic region measured in smaller, regressing tumors may account for a large percentage of the total volume.

Based on the previous studies by Bullitt et al, that demonstrated vascular normalization in response to successful RT response, a similar response trend was expected in our study. Interestingly, no significant changes in vascular morphology was detected using any of the metrics. The reason for this discrepancy is uncertain, but we suspect that the treatment conditions may have an effect on the microvascular response. The cancer treatment described by Bullitt et al was whole brain radiation [36]. Although treatment details were not shared, whole brain radiation is typically fractionated by 20-40 Gy/5-10 fractions, limiting a single fraction to 3-4 Gy [86]. This is in contrast to the treatment conditions used in this study which consisted of a single high dose of radiation in the range of 15-25 Gy, in a small rodent model. Revisiting vessel tortuosity changes is warranted with future studies with gentler treatment conditions (i.e. fractionated radiation, 15 Gy/5 doses).

In addition to the treatment conditions, the response may very well be tumor model dependent. The diversity of human tumors encompasses with a wide range of neovascularization

patterns, including both avascular (hypoxic) and vascular development [87]. Further investigation using this technique in different types of human-derived tumor models is warranted since the microvascular response after exposure to radiation will likely vary among different tumor types. Regardless, we are encouraged from these results that quantitative microvascular measurements using AA may significantly improve the current methods for treatment assessment.

In our study we retrospectively categorized the treated tumors as complete response or failure based on the final treatment outcome. The development of a predictive tool indicating treatment outcome based on repeated VVD (or other vessel morphological features) and TV measurements will be highly relevant to the clinical translation of this diagnostic technique.

# CHAPTER 5:

# Preliminary Functional Principal Components Analysis on Longitudinal Microvascular Imaging Data Sets

## 5.1 Overview

In the previous chapter, we demonstrated the feasibility of using AA to quantify changes tumor microvascular structure in response to a single dose of broad-beam RT. We investigated five metrics describing VVD, PN, and vessel tortuosity. We observed significant differences between partial and complete responders using the VVD metric only – PN, SOAM, DM, and, TCM did not yield any significant differences in any of the groups (within response groups and treatment cohorts). An increase in VVD preceded TV regrowth in partially responding tumors post- RT. This result suggests that we may be able to assess non-responsive tumors sooner using microvascular imaging, then compared to TV alone. In this chapter, we will explore functional data analysis (FDA) techniques to demonstrate the predictive potential of tumor microvascular imaging. The FDA model will be based on VVD data and will first be developed on a training set of rat tumor data, and later evaluated using a test data set. We hypothesize that by using FDA techniques on longitudinal data we may be able to discriminate partial responders from complete responders with significant sensitivity and specificity compared to TV. Our objective here is to demonstrate a proof-of-concept, clinically relevant tool for early assessment using quantitative microvascular imaging.

## 5.2 Functional Data Analysis on Biologically Relevant Longitudinal Data

FDA is a branch of statistics that characterizes data from repeated measures for a single test subject or condition [88]. The defining characteristic of functional data includes specifically curves and trajectories. Normal multivariate regression techniques are commonly performed on time series data, within discrete time points, however this ignores the time-varying behavior that actually describes the shape of a particular curve or trajectory [89]. The basic principle of FDA is that instead of expressing individual observations at a given time point as scalar values or vectors, they are represented as functions. For instances, in a very simplified context, a single observation can be described as a derivative function instead of a scalar value. The result of analyzing time series data in a functional manner is that the generated models are continuous and smooth, with reduced noise from the observed data [90]. FDA has been most commonly applied in econometrics, but can be applied to biologically relevant longitudinal data (specifically in the fields of bioinformatics and biostatistics). The difference between conventional "functional data" and "longitudinal data" is that the latter is typically described as sparse and irregular. FDA can be used to predict smooth trajectories even when the number of longitudinal data points is limited within each subject. One method of FDA for longitudinal data is functional Principal Component Analysis (fPCA). Traditional PCA is a versatile method of dimensional reduction for extracting linearly uncorrelated variables from a set of data potentially containing correlated variables. This can be applied efficiently to longitudinal data to reduce a high dimension of trajectories (for example from a large longitudinal data set containing multiple test subjects) into a lesser number of dimensions. Muller and Yoa et al describe in detail the techniques and applications for fPCA as well as other FDA methods [90–92].

Here we demonstrate the implementation of fPCA on longitudinal data derived from AA microvascular images for predicting the response of individual subject repeated measurements based on the trajectory analysis of many training subjects.

## 5.3 Methods

### *5.3.i Acquisition of Additional Data*

In order to increase our sample size, we treated 14 additional rats with 15 (n = 9) and 20 (n = 5) Gy doses of broad beam RT. Tumor models, imaging acquisition and analysis, and RT were consistent with what was previously described in Chapter 4. Since longitudinal measurements of PN, SOAM, DM, and TCM did not yield significant differences between partial and complete responders, only VVD and TV metrics were used for fPCA.

### *5.3.ii Data and Statistical Analysis*

The rats imaged in the second round of experimentation were categorized as partial or complete responders based on their final response outcome at the end of the study, same as previously described. After image processing and microvascular feature quantification, we ended with approximately 256 longitudinal time points from 35 rats treated with either 15, 20, or 25 Gy of radiation. Untreated, control rats were not used for data analysis.

For the prediction model, fPCA was used for longitudinal data analysis for sparse and irregular data sets. fPCA was performed on a training set, which consisted of 60% of all the longitudinal data from the *treated* rats (the percentage was applied to both partial responders and

complete responders, indiscriminant of the treatment conditions). Typically ratios such as 80/20 or 70/30 are used, but due to the relatively small sample size, a 60/40 split was preferred, which would allow us to perform statistics on the testing set (the remaining 40% of the data). The principal components (PCs) fitted values from the training set were then applied to the testing set. fPCA scores from two eigenvectors were used for performing binomial logistic regression with a logit link to estimate coefficients $\beta_1$ and $\beta_2$. Then, a linear predictor, in the form of:

$$\eta = \alpha + \beta_1\xi_1 + \beta_2\xi_2$$

was used for binary classification of partial (1) and complete responders (0), where $\eta$ is the predicted value from the logistic regression, $\alpha$, $\beta_1$ and $\beta_2$ are estimated coefficients from the logistic regression, and $\xi_1$ and $\xi_2$ are the eigenvectors from the fPCA. For TV and VVD, one and two eigenvectors (PCs) are used, respectively. The number of PCs required for the model was determined by achieving a threshold of 90% variance explained by the sum of the first *n* number of PCs [93]. The fPCA and functional longitudinal analysis techniques have been adopted from Müller et al [90]. Receive operator characteristic (ROC) curves were then constructed for presenting true and false positive rates. The validation using the test set was performed at varying time point durations in order to assess the change in sensitivity and specificity of the prediction over time. The shortest assessment duration was from day 0 to day 7, and ranged to day 0 to day 30. Twenty-three sets of ROC curves were constructed for both TV and VVD and a plot of the area-under-the-curve (AUC) was created for each metric against the time point at which the peak AUC was achieved (representing the highest true positive rate and the lowest false positive rate).

fPCA was performed for both VVD and TV separately. P-values and estimated errors, as well as the F-statistic and p-value of the overall regression were calculated for each assessment

duration and for each metric at the assessment duration iterations 1 (days 0-8), 6 (days 0-13), and 23 (days 0-30). The fPCA testing was repeated with the exclusion of days 1-5 in all data sets. These days were excluded to remove the effect of initial tumor size as well as the complex initial delayed growth response immediately after irradiation in both TV and VVD growth curves.

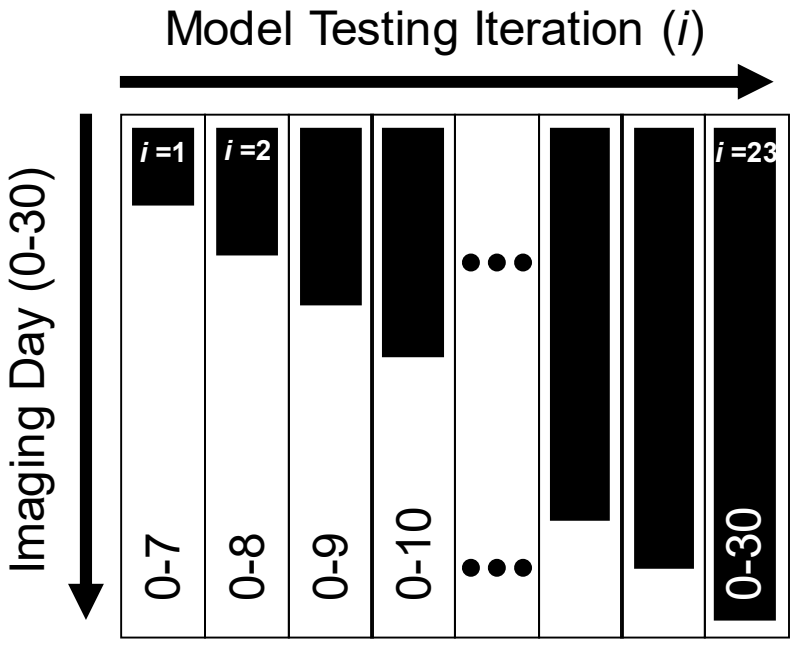


Figure 5. 1. The 23 iterations of fPCA testing included systematically varied assessment durations ranging from day 0 to days 5-30. These iterations were repeated with days 0-5 excluded from analysis.

All fPCA analysis was performed using the Principal Analysis by Conditional Expectation (PACE) package for MATLAB [90,92,94]. Logistic regression and ROC curve generation were performed separately, also using MATLAB.

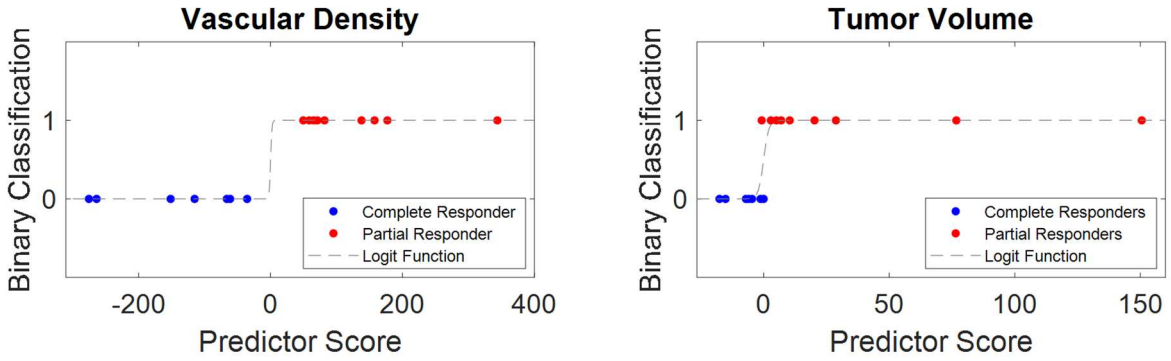


Figure 5. 2. Example results from the binomial logistic regression and fit to a logit curve from day 14. Better lateral separation is evident between the two groups with VVD (left) compared to TV (right).

## 5.4 Results

The scree plot for TV calculated that the first two PCs account for 97.035% of the variance in the data and for VVD, the first three PCs account for 95.634% of the variance in the data. The number of PCs describes how many orthogonal modes of variation are required to best explain the data.

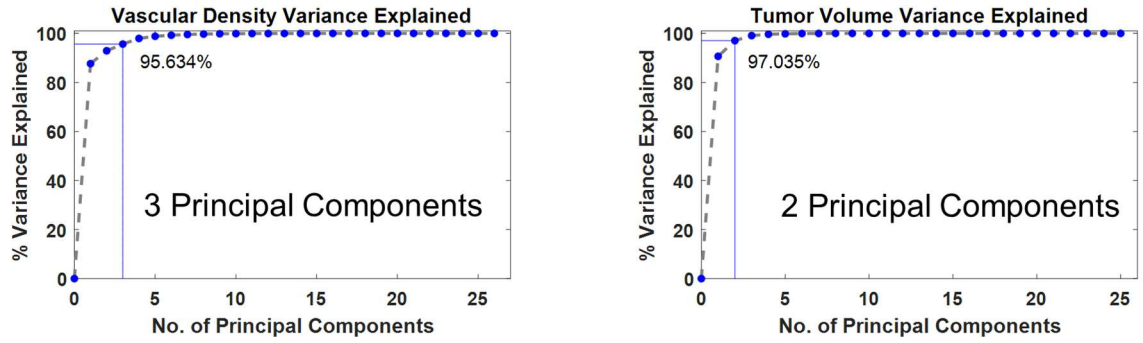


Figure 5. 2. Scree plots for TV and VVD. The cut-off for Variance explained was set at 95%. 2 PC was chosen for TV and 3 were chosen for VVD in order to satisfy the cut-off condition.

Figure 5.3 illustrates the change in AUC over the assessment duration iterations for both TV and VVD.

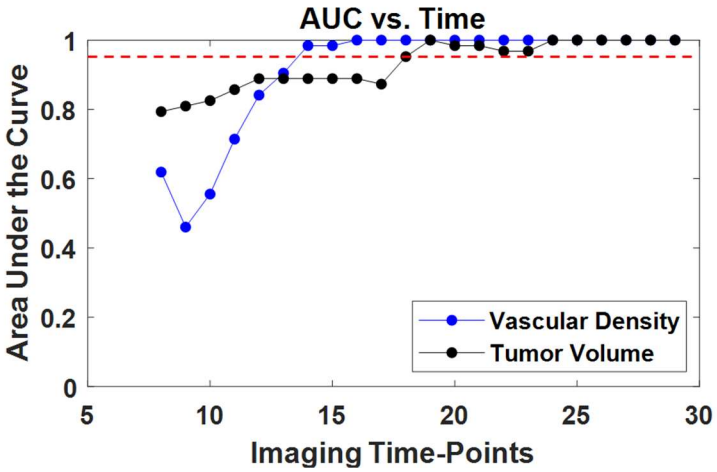


Figure 5. 3. Plots of AUC of ROC curves over the different testing iterations.

The peak AUC for TV was calculated to be 0.95 (maximum specificity and sensitivity of 100% and 89%, respectively) at day 18, and the peak AUC for VVD was calculated to be 0.98 (maximum specificity and sensitivity of 100% and 89% respectively) at day 14. VVD has a higher AUC value of 0.98 at day 14 compared to TV, which has a value of 0.89. From day 18 to 30, AUC for both TV (mean AUC = 0.98 ± 0.02) and VVD (mean AUC = 1 ± 0.0) are comparable and above 95%.

## 5.5 Discussion and Conclusions

Previously, retrospective analysis of longitudinal AA data showed significant differences in VVD as a function of time between partial and complete responders occurred earlier than using TV. The objective in this study was to develop a proof-of-concept predictive tool using existing statistical methods for assessing tumor response to RT for an individual test subject with limited longitudinal data points. We have demonstrated the application of fPCA on AA data for analyzing group trajectories of treated tumors for discriminating partial from control responders and then applying them in an untested set of longitudinal data for treatment response classification. Using exploratory longitudinal analysis in Chapter 5, we were able to identify key features differentiating partial and control responders and untreated tumors. Key features included initial TV and VVD, and regression and recurrence growth rates. We also observed a dose dependent response that affected the time at which recurrence occurred. The high dimensionality of the trajectory data (growth rates, initial values, inflection points and local minima and maxima, etc) is difficult to analyze using normal linear regression models. fPCA helped to reduce the number of trajectory dimensions into 2 dimensions for TV and 3 dimensions for VVD (given by the number of PCs used for each metric).

An FDA type approach for longitudinal AA data is very beneficial as it focuses on the trajectories rather than the absolute values of the measurements. The large error bars calculated within groups is expected due to varying initial tumor sizes and overall intrinsic variability in individual tumor behavior. By using only the mean response trajectory of the entire group, response classification is inefficient and prone to large errors because of these variabilities. Normalization remedies this effect only slightly, as it is still dependent on the initial absolute

measurement. The result using mean trajectory analysis or linear regression is that at any given time-point, the correlation between the metric and response is low.

The results from the fPCA analysis suggests that VVD can classify partial from complete responders earlier than TV, although the specificity and sensitivity for both metrics are comparable. The difference between the two metrics is much more pronounced with days 0-5 included in the analysis. Specifically, the shape of the curves between days 0-5 has a significant effect on the predicted trajectories. The reason for the drastic decrease in TV performance while VVD performance slightly improved is still unclear, but may likely be a function for the variance explained cut-off and the low sample size of this study.

Sparsity and irregularity in longitudinal data sets may first seem to be an insufficiency for statistical analysis, but this strongly depends on the type of data being acquired. In our case, measurement error manifested in the form of noise in our growth curves. TV measurement growth curves are straightforward and well understood. This is in contrast to VVD which is a noisy metric, and measuring with too high of a frequency (in terms of number of days between imaging time points) will add unnecessary low-level noise. This is evident in our earlier imaging experiments where imaging was performed on 5-7 consecutive days post- RT. Sparse measurements reduces this noise. The opposite extreme is also not beneficial, however this can be counteracted by increasing the sample size and irregularity of the time points.

Other techniques for removing noise that were trialed but not used or discussed in this chapter included binning of time points that were too close together, reducing measurement noise, and smoothing of data points that were far apart using cubic spline interpolation. Both techniques were used coincidentally for performing multivariate linear regression on the derivatives of the growth curves, however this was abandoned due high error and over estimation

of the slopes. Curve smoothing using splines and derivative analysis should be revisited in future studies, considering appropriate samples sizes and conditions, as it is related to fPCA techniques and has also been shown to be a suitable method for longitudinal data analysis [95].

There are several limitations to the structure of the analysis that should be accounted for. With each test iteration, the number of points added to the test were decreased since complete responders had no data once the tumor was immeasurable (typically around day 25). Adding more data points did strengthen the result, however this only affected the partial responders' scores. Additionally, we used a small sample size relative to previous studies that demonstrate the use of fPCA. Many FDA type studies incorporate measurements that are automatically recorded by instrumentation resulting in hundreds of data points, or are performed retrospectively on large data sets [96]. The sample size (n=35 treated test subjects) was further decreased since the data set was split into training and testing sets. Accumulating more data is necessary for performing robust fPCA. Also, in the study in Chapter 5, we observed a significant dose dependent response, specifically in TV growth rates. In fPCA analysis, we grouped all dose groups together (excluding untreated tumors). Owing to the small sample size, it was not feasible to split training and testing sets within dose groups. Treatment dose was added as a secondary predictor for logistic regression, however it did not add any value in improving the response classification. In the future, a cross-validation method can be used for testing with small data sets.

Finally, only one vascular metric (VVD) was used. Other microvascular metrics discussed in the previous chapters were not included since no significant differences between groups were measured at any time point. As discussed previously, additional investigation is required to better understand the behavior of vessel tortuosity and tumor necrosis in response to

RT, and should not be necessarily excluded from future studies. Specifically, the effect of the radiation treatment conditions on vessel tortuosity should be revisited since prior work has demonstrated clinical relevance of vessel tortuosity on assessing RT outcome. Adding additional predictors (including variables such as treatment dose, and weight as a marker for treatment toxicity) to the model improves the fit of the prediction model, assuming an appropriate increase in sample size and observations.

# CHAPTER 6:

# Extensions, Limitations, and Future Directions

## 6.1 Molecular Imaging for Assessing Response to Radiation Therapy

### *6.1.i Overview*

Ultrasound molecular imaging (USMI) is a branch of CEUS that employs microbubbles that are specially designed to bind to biomarkers expressed on the endothelium for targeted imaging [50,61,97]. Certain angiogenic specific biomarkers (i.e. VEGF, $\alpha_v\beta_3$) are highly expressed in tumor situated endothelium, and since angiogenesis is a key characteristic of tumor growth, these biomarkers are ideal candidates for targeted imaging of cancer. There is already a considerable amount of literature demonstrating the use of USMI for detecting cancers and assessing response to therapy (Figure 6.1) [98–101]. To our knowledge, no one has reported a longitudinal study using USMI for early assessment of tumor response to RT.

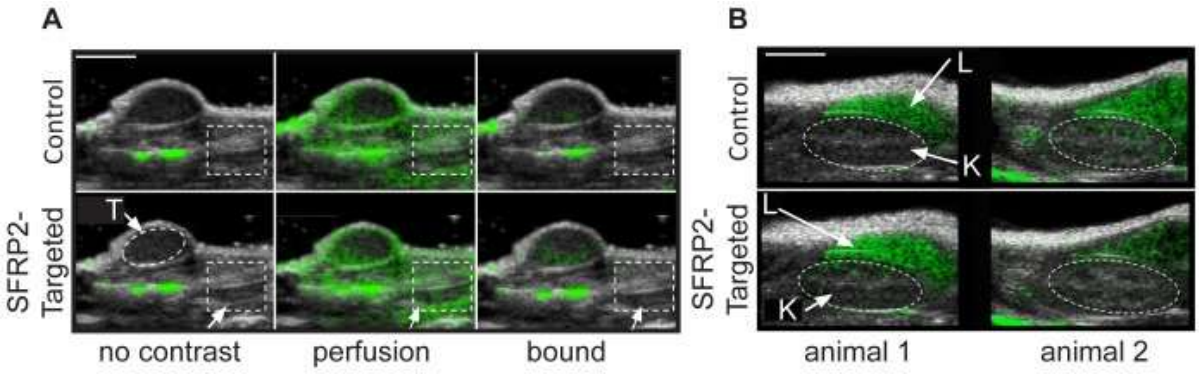


Figure 6. 1. USMI of a murine angiosarcoma model, using SFRP-2 targeted microbubbles. USMI was demonstrated as a non-invasive method for monitoring angiosarcoma response to therapy. Figure reprinted with permission from [101] (Copyright © 2014 Tsuruta et al).

In our previous results, we observed increases in VVD prior to TV regrowth in partially responding tumors. The growth of new vessels implies that the tumor conditions are favorable for angiogenesis. We hypothesize that even prior to measurable increases in VVD using AA, USMI may be able to detect early expression of angiogenic biomarkers (Figure 6.2).

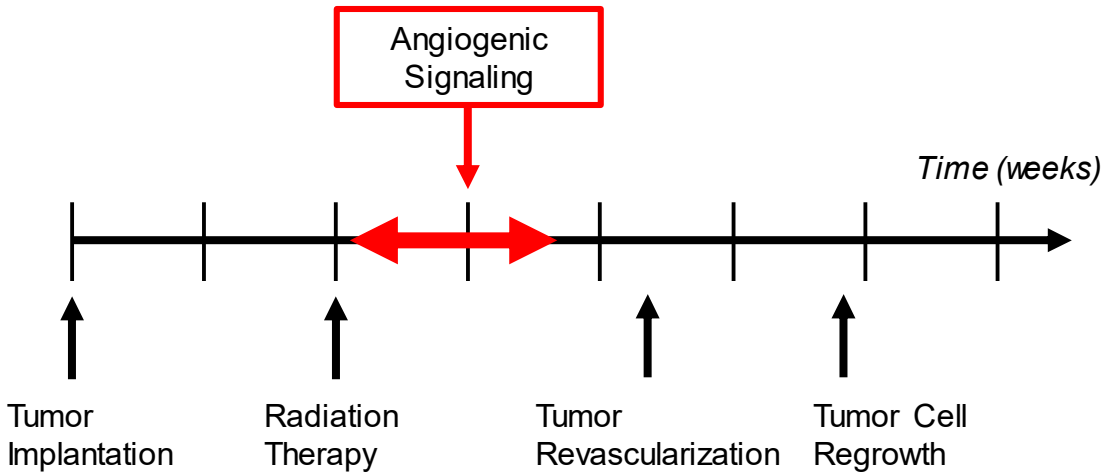


Figure 6. 2. The black features represent the standard treatment and imaging schedule, and the red feature represents the hypothesized period of angiogenic signaling. Since expression of VEGF stimulates angiogenesis, it is theorized that USMI can detect tumor regrowth even sooner than VVD.

### *6.1.ii Methods*

A pilot study was conducted consisting of 10 tumor bearing rats, 8 of which were treated with a single 15 Gy dose of RT. Animal preparation, tumor models, imaging schedules, and radiation procedures were consistent as what was described in Chapter 4.

A very similar longitudinal imaging study was performed using USMI instead of AA on a Siemens Acuson Sequoia 512 scanner with a 15L8 linear array transducer. All imaging was performed using Cadence Pulse Sequencing (CPS) mode, a CEUS technique employing both pulse inversion and amplitude modulation [102]. Targeted microbubble contrast agents were prepared with biotinylated sc-VEGF and were designed to target to VEGFR-2 [103]. Briefly, the methods for USMI are as follows. The size distribution and concentration of the prepared targeted microbubble contrast agents were measured prior to imaging at each time point using a particle sizing system (AccuSizer, Particle Sizing Systems, Port Richey, FL). An appropriate volume of microbubbles were pipetted into 100 uL of sterile saline so that the final microbubble count was approximately $4x10^7$ bubbles (this number of bubbles was determined by previous calibration tests). Prior to contrast injection, the ultrasound probe was positioned over the tumor using the same imaging apparatus described in Figure 4.1, and a 3D b-mode scan was acquired followed by a baseline scan in CPS mode.

The contrast agent was then injected intravenously as a bolus via the tail vein. The initial contrast wash-in was captured as a cine clip in the midplane, and once the tissue was fully perfused, a 3D scan of the entire tumor was acquired. Microbubbles were allowed to circulate up to 7 minutes before a second 3D scan was acquired to capture the bound targeted bubbles. The 7 minute wait time allowed for microbubble binding to the targeted sites and clearance of unbound bubbles. After the second 3D scan was acquired, a series of high MI pulses were delivered to

clear all bound bubbles, followed by an additional minute of wait time to allow for reperfusion of any remaining microbubbles in circulation. A third 3D scan was then finally acquired to capture any free flowing bubbles that may be considered as background noise (Figure 6.3).

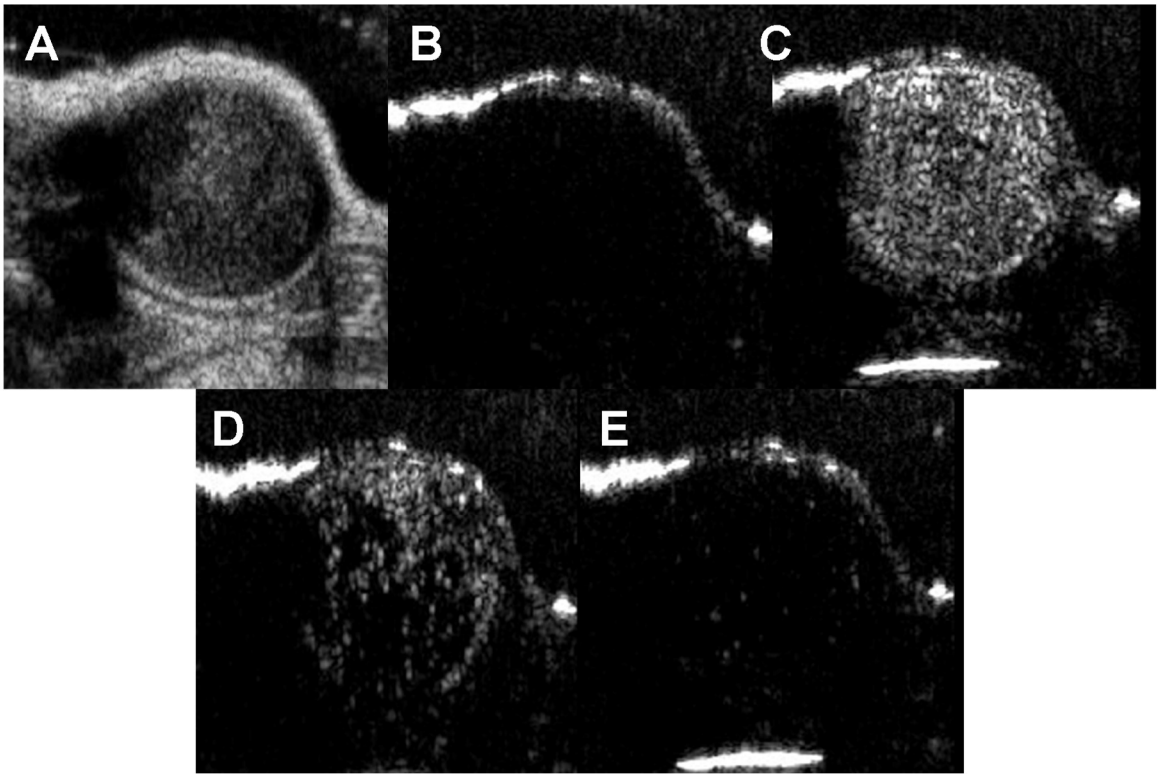


Figure 6. 3. Sample 2D images from 3D scans from a single tumor. A) a b-mode image used for measuring the tumor volume, B) a baseline image for quantifying tissue background noise, C) the fully perfused tumor used for detecting potential regions of necrosis, D) the targeted contrast image after 7 minutes, and E) the post microbubble destruction image for detecting residual free flowing bubbles.

The first 3D scan which captured the fully perfused tumor was used to detect any necrotic regions of the tumor. These regions were subsequently subtracted from the molecular targeted scans to prevent underestimation of molecular targeting. The average intensity of the post-destruction scan was subtracted from the intensity of the targeted scan, and a single intensity

value as recorded for each animal and at each time point. TVs were also measured by estimating the ellipsoidal volume based on three orthogonal diameters of the tumor.

### *6.1.iii Results and Discussion*

Tumors were classified as partial responders and complete responders at the end of the study. Of the eight treated tumors, 6 displayed complete response while 2 displayed a partial treatment response. As expected, there was a greater average initial TV in the partial responders compared to the complete responders, however this difference was not significant. All treated tumors underwent similar response phases as described in Chapter 4. Interestingly, the measured USMI signal trends was similar for all treated tumors and was characterized by an initial decrease in signal intensity and then from day 8, molecular targeted signal begins to increase (Figure 6.4). In complete responders, this increase in molecular targeted signal occurs despite decreasing TV. In depth analysis of this data set was not performed because there were several limitations and confounding variables that were overlooked.

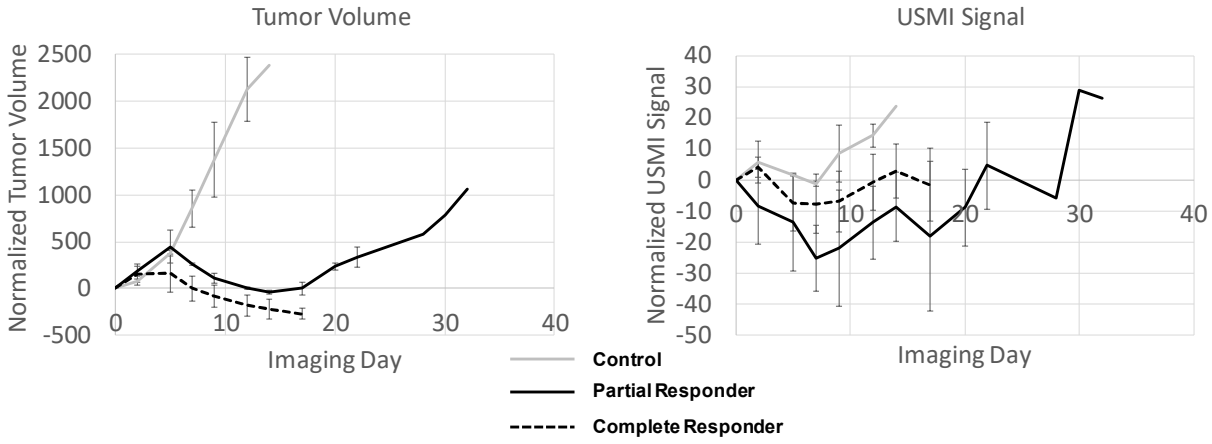


Figure 6. 4. Summary of average longitudinal curves of TV (left) and USMI (right). USMI suggests there may be some underlying differences between partial and complete responders, however the results are not statistically significant. The dip in the USMI signal for the control group around day 7 is an example of the potential ACB effect on microbubble targeting.

First, the accelerated blood clearance (ABC) of PEGylated particles significantly affects the clearance of microbubble contrast agents in longitudinal studies [104]. Specifically, the production of PEG-specific antibodies in response to the PEG found on the microbubble shell, promotes faster clearance, and the rate of clearance has been recently shown to increase with successive microbubble doses. One of the potential solutions to the ABC effect is to pre-dose the rats with PEGylated lipid solution to "prime" the antibody production before the start of the study. In this way, the measurements are more consistent throughout the duration of the actual study.

In this study, we captured only one time point after the bolus injection. An alternative method is to capture a time-intensity curve (TIC) of the bolus injection and calculate the area under the curve for each TIC as a measure of molecular targeted signal [103]. This also ensures that any lasting ABC effect after pre-dosing is accounted for. Other variables that need to be

carefully considered in future experiments is the accuracy of the microbubble concentration and selecting a dose that is sufficient for maximum microbubble binding, yet low enough for to allow for efficient clearance of unbound bubbles. The disadvantage of using a high microbubble dose is that the wait time for unbound bubble clearance is too long, risking the shearing or dissolving of already bound bubbles which eventually results in lower targeted signals. The microbubble dose of $4x10^7$ bubbles was based on previous work. However, due to the ABC effect, the clearance was too fast. The optimum concentration will need to be reassessed before the next iteration of the study.

While in this study we used the Sequoia 512 for contrast imaging, USMI and AA can be performed simultaneously using the same RMV transducer. Shelton and Lindsey et al previously demonstrated molecular imaging with high contrast sensitivity and SNR, by implementing AA imaging with targeted microbubbles [105]. While the results from our pilot study were inconclusive and the usefulness of USMI for assessing tumor response to RT is still uncertain, the possibility of performing both high-resolution microvascular imaging and USMI using the same system allows us to correlate functional and anatomical imaging of microvasculature simultaneously.

## 6.2 Current Limitations of Acoustic Angiography and Improvements

The current dual-frequency prototype transducer used in the studies described in Chapter 4 and other preclinical studies suffers from resolution and imaging depth limitations. The resolution of AA is between 100-200 μm, which places a limitation on the smallest size tumor that can be accurately quantified in terms of microvascular features. For example tumors less

than 1 mm in diameter may inaccurately measure VVD as high as 20-50% due to the resolution limitation. Despite this limitation, it is a significant improvement to conventional contrast imaging techniques.

Additionally, due to the fixed focus of the dual-frequency transducer, our depth of field was limited to approximately 1.0 cm axially with a maximum depth of penetration of ~2 cm. Tumors near 2 cm in diameter were clipped at the top and bottom in order to maintain the focus of the transducer in the center of the tumor. Decreasing the transducer receiving frequency will improve the imaging penetration depth and depth of field, however the signal-to-noise ratio is compromised due to the reduced separation between tissue signal and higher harmonic contrast signal. Conversely, increasing the receiving frequency will improve resolution, but at the cost of decreasing contrast sensitivity, penetration depth, and depth of field. It is worth noting that new super-resolution imaging techniques may provide an alternative solution to imaging angiogenic vasculature with an order of magnitude better resolution once the technology matures. However, super resolution imaging still requires tens of minutes to acquire a 3D volume of data due to data acquisition and processing limitations [106]. Despite these limitations, AA has remarkably high resolution and contrast sensitivity relative to clinically available CEUS techniques. Further, development of a linear array dual-frequency transducer will enhance AA with increased depth of field and faster image acquisition required for clinical translation [107,108].

### 6.3 CEUS and Radiomics

There has been a recent surge of interest in developing models for predicting a patient's outcome to cancer therapy. The field of Radiomics, for example, has been established to use

large sets of minable MR, CT and PET imaging data to extract quantitative features such as tumor sphericity, homogeneity, and volume. When combined with other patient medical data, it can be analyzed using advanced bioinformatics statistical techniques to determine correlations to tumor behavior and treatment response [109]. Similarly, with AA image data, we can extract additional quantitative features that describe microvascular characteristics of certain tumors and their response to therapy. We plan to continue investigating changes in vessel morphology and molecular expression in response to RT in future studies. Contrast-enhanced ultrasound imaging is a safe, inexpensive, and highly accessible imaging modality with many applications in all fields of oncology, and with on-going technical improvements, AA is a promising and clinically translatable imaging technology.

While the biological basis for the variation of tumor response to radiation is still not entirely understood, there is a growing body of evidence that suggests that the tumor microvascular environment plays a significant role in radiation treatment efficacy. Our objective in these studies was to assess tumor response to radiation by quantifying changes in vascularity that may be associated with treatment outcome. Our results demonstrated that vascular changes, specifically increases in VVD, are a potential biomarker for assessing long-term tumor response to RT. We believe that providing a more timely and reliable method for assessing treatment response may enable clinical treatment decisions to be made earlier than the current standard of care, therefore improving cancer patient outcomes.

# CHAPTER 7:

# In-vitro and In-vivo Testing of a Prototype Dual-Frequency Array Transducer

## 7.1 Overview

### *7.1.i Development of a Dual-Frequency Linear Array for Acoustic Angiography*

AA uses a low frequency transmit and high frequency receive at significantly separated bandwidths. An ultra-broadband transducer centered at a single frequency capable of efficiently transmitting at low frequencies near microbubble resonance and receiving high frequencies (8-10th harmonic difference), currently does not commercially exist. Capacitive micromachined ultrasonic transducers (CMUTs) may potentially be able to accomplish this, however the technology is still in its infancy. As a solution, a dual-frequency probe was developed, with two separate and co-aligned elements mechanically translated in the lateral dimension. As a prototype transducer, this "wobbler" type probe has been sufficient for many significant preclinical studies to demonstrate feasibility of AA for microvascular imaging, as demonstrated in Chapter 4. The current transcutaneous prototype dual-frequency transducer for AA is limited to imaging from outside the body at a single focal depth (limited to ~1.5 cm), due to the confocal single element design. Additionally, due to the single element design, more advanced imaging

schemes such as angular compounding, multi-focal imaging, and dynamic receive beam forming cannot be performed.

Current clinically available transducers are either linear, curvilinear, or phased array transducers containing up to hundreds of individually excitable elements, which allows for more advanced beamforming and imaging techniques. The major advantages of using linear array transducers over a single element wobbler type transducer include the ability for electronic focusing, improved lateral resolution and sensitivity, parallel scan lines which form a uniform image in depth, as well as increased frame-rate and depth of field. Also clinically speaking, linear arrays are more ergonomic as they are easy to couple against the human body and can be easily designed into form factors for various imaging applications. The current challenge in adapting linear array imaging to AA is the requirement for a dual-frequency transmit and receive. Starting in 2002, Bouakaz et al and Van Neer et al reported the design of an interleaved dual-frequency phased-array for superharmonic imaging which consisted of alternating elements with center frequencies of 2.8 MHz and 900 kHz (Figure 7.1) [110–113]. While this transducer design was a significant step towards clinical superharmonic imaging, due to the interleaved element scheme, the kerf for the high-frequency elements would include the width of the low frequency elements as well, reducing receive sensitivity and increasing sidelobes (resulting in image blurring). Over the years there have been many other reports of dual-frequency transducers for imaging and imaging/therapy applications [114].

Recently Kim et al and Li et al developed a novel proof-of-concept dual-frequency, co-linear array with a stacked design approach of low-frequency (2-3 MHz) transmit and high-frequency (10-20 MHz) receive (Figure 7.1). This design overcomes the kerf limitations of the interleaved design hence reducing the sidelobes. While the lower receive frequencies compared

to the RMV probes (4/30 MHz) enables greater depth of penetration and may be suitable for transcutaneous imaging, the frequency range is ideal for intracavitary (i.e. transvaginal, transrectal) applications, specifically for prostate imaging [108,114].

### *7.1.ii Dual-frequency Transrectal Ultrasound for Prostate Cancer Imaging*

Prostate Cancer (PCa) is the second most commonly diagnosed cancer in men worldwide. The American Cancer Society estimates over 220,000 new cases and 28,000 deaths (12% death rate) in the United States alone in 2015 [115]. Currents methods of diagnosis and clinical staging have been shown to have low sensitivity and specificity, limiting early detection and intervention. Early diagnostic blood work for abnormal levels of prostate specific antigen (PSA) is clinically recommended for men over the age of 50, followed by digital rectal examination (DRE). Since increases in PSA levels and enlargement of the prostate are not specific to PCa, both preventative measures have poor specificity and suspicious masses felt during physical examination often require follow up biopsies. Moreover, DRE is only sensitive to tumors that are in the peripheral and lateral regions of the prostate. Prostate tumor biopsies, which typically consist of 10-12 cores (Sextant biopsy scheme), have false-negative rates of 20-30%. Increasing the number of biopsy samples improves the diagnostic sensitivity, but suffers a trade-off with increasing patient discomfort and risk of infection and hemorrhage [116–119].

For PCa detection and prostate tumor biopsy guidance, traditional gray scale ultrasound cannot adequately identify diseased tissue if it is isoechoic with the surrounding healthy parenchyma. Unfortunately, up to 32% of all prostate tumors are isoechoic. The classical presentation of solid tumors on ultrasound is hypoechoic with the surrounding tissue; however only 17-57% of biopsy cores extracted from hypoechoic masses are diagnosed as PCa. To date,

the use of traditional b-mode ultrasound is limited to biopsy guidance of the needle to the different anatomical locations of the prostate [120]. MRI and MRI-TRUS fusion guided biopsies have increased the accuracy of needle core biopsies, but require substantially more expensive equipment and the use of two different imaging modalities [121].

Contrast enhanced transrectal ultrasound (CE-TRUS) has been tried as a method for targeting areas with higher perfusion within the prostate for extracting biopsy cores. However, results have shown that while CEUS targeted biopsy significantly improves the detection of high grade/high volume PCa, its accuracy of identifying malignant lesions is confounded by the enhancement of benign tissue [122]. Additionally, CE-TRUS lacks the contrast resolution to resolve individual vessels for measuring vessel morphology and density within the tumor, which may be a more sensitive measure of malignancy [123]. Currently using imaging alone, CT, MRI, and gray scale TRUS are not sensitive to small tumors (<5 mm) and do not improve the detection of PCa over tissue biopsies, which remains the gold standard [124]. AA has since been demonstrated to detect tortuous microvasculature that correlate with cancer growth in preclinical models, which suggests that AA may potentially be more sensitive to detecting malignant PCa than conventional CE-TRUS. To test this hypothesis, Li et al designed and developed a dual-frequency transrectal ultrasound (DF-TRUS) transducer using the stacked-type configuration discussed previously.

The current DF-TRUS transducer prototype was designed and dimensioned specifically for transrectal imaging of the prostate. The normal prostate is within 5 mm from the rectal wall and approximately 30 mm x 25 mm in size, however enlarged prostates can grow as large as 50 mm x 45 mm. The frequency selection was based on an approximate imaging depth of 20-40 mm. The array consists of 64 low-frequency transmit elements and 128 high-frequency receive

elements with center frequencies of 3 and 15 MHz, respectively. The stacked element design consists of two high-dielectric constant PZT active layers, separated by an isolation layer and flexible circuit. The pitch of the low-frequency transmitting and high-frequency receiving elements are 240 μm and 140 μm, respectively. The transducer design was modeled using the Krimholtz–Leedom–Matthae (KLM) model finite element analysis, and acoustic field simulations were performed using Field II [125,126]. The aperture length is 18 mm, comparable to current commercially available TRUS transducers (i.e. Siemens EV-8C4).

Our hypothesis is that the DF-TRUS transducer can demonstrate comparable SNR and CTR compared to a commercially and clinically available prostate transducer, the Siemens EV-8C4. Our objectives are to perform in-vitro and in-vivo experiments with the DF-TRUS to assess the feasibility of AA for PCa imaging.

## 7.2 Methods

### *7.2.i Verasonics Coding*

All DF-TRUS imaging was performed on the Verasonics Vantage 256 system. A custom connector was designed and fabricated to adapt the prototype transducer with the Verasonics scanhead interface and MATLAB Verasonics scripts were developed for linear array imaging. Transmit and receive frequencies were selected at 3.125 MHz and 15 MHz, based on their respective center frequencies, and the maximum sampling rate of the Vantage (62.5 MHz) was used. 128 transmit ray lines were specified, with 128 corresponding receive events. The synthetic aperture size for each transmit ray line was calculated based on the specified focal depth (between 10-30 mm) and the F-number (1), and ranged from 10-30 elements.

### *7.2.ii DF-TRUS Development*

A detailed explanation of the DF-TRUS design and fabrication process has been reported previously [127]. Briefly, the design consisted of a dual-layer stack structure with the bottom layer containing the low-frequency transmit elements and the top layer containing the high-frequency receive elements. The high-frequency array can exist on top of the low frequency array due to the thin size of the elements, which minimally interferes with acoustic transmission. The two layers were separated by an E-Solder 3022 isolation layer to prevent degradation in transmit and receive bandwidths due to aliasing echoes. A transmit frequency of 3 MHz was chosen to match the resonance frequency of the microbubble contrast agents, and a receive frequency of 15 MHz was chosen based on the thickness of the element, which minimizes interference with the transmit pulse as well as well providing a sufficient bandwidth separation from the transmit elements. Field II and the Krimholtz-Leedom-Matthaei (KLM) model were used for testing and design of both transmit and receive apertures, as well as the matching and isolation layers.

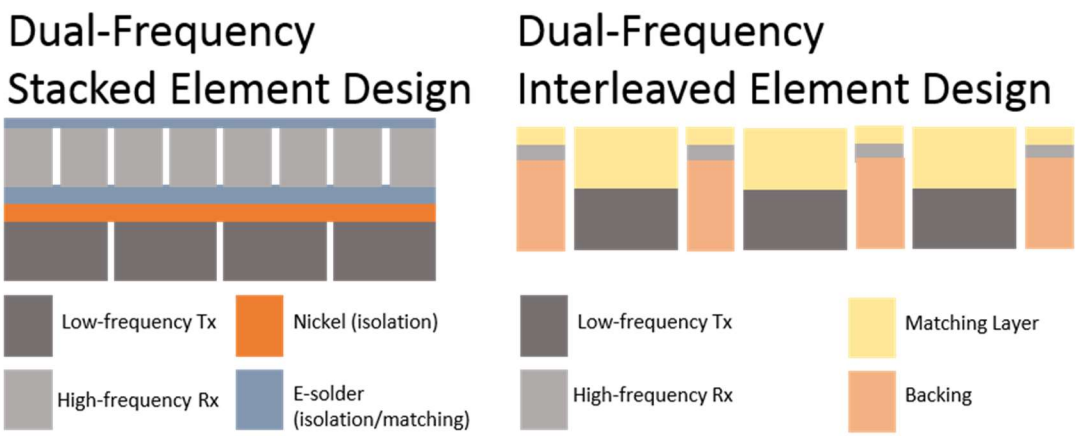


Figure 7. 1. Stacked element design proposed by Li and Kim et al for the dual-frequency linear array design. The design consists of high frequency elements stacked on top of the low frequency elements, with a matching and isolation layer in between. This is in contrast to the dual-frequency interleaved element design proposed by Bouakaz et al.

Briefly, for fabrication, a 500 µm PZT plate for the low frequency transmit was attached with a top electrode using conductive epoxy. After curing, the epoxy was lapped precisely to 30 µm in thickness, followed by the bonding of the PZT 2-2 composites receive elements using Epo-Tek non-conductive epoxy. The receive layer was then lapped to 100 µm to achieve a 15 MHz resonance frequency, and then received a top coated of Ti/Au as a conductive layer. After dicing the low and high frequency elements to a 280 µm and 140 µm pitch, respectively, the array stack was bonded to a flex circuit on both sides and then connected to a printed circuit board which would be later used to connect to the Verasonics scanhead interface (Figure 7.2) [127].

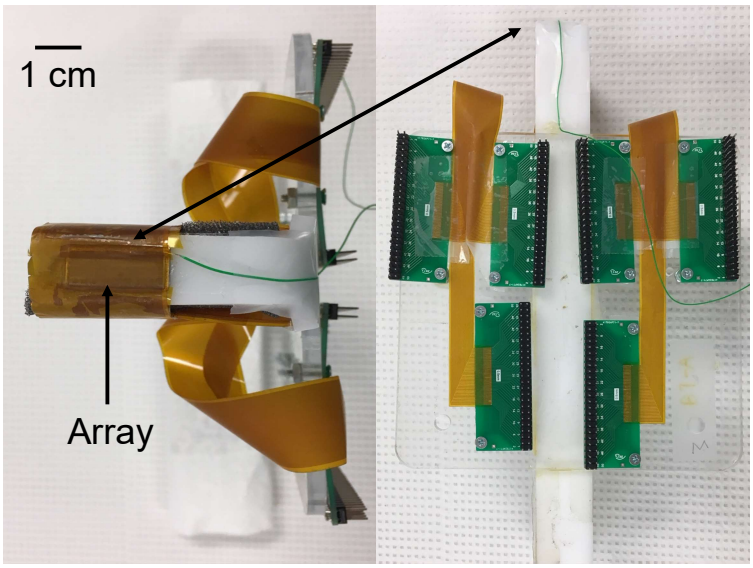


Figure 7. 2. Bottom (left) and side (right) views of the DF-TRUS prototype transducer. The array is located on the bottom indicated by the black arrow. A flex circuit couples the array elements to printed circuit boards, which connect to a custom adapter cable for the Verasonics Vantage.

### *7.2.iii Acoustic Characterization*

The transmit waveforms, pressures, and acoustic beam maps were measured for the DF-TRUS transducer. Measurements were recorded using a needle hydrophone (HNA-0400, ONDA, Sunnyvale, CA) connected to an analog-to-digital converter with a sampling rate of 200 MHz. A custom LabVIEW program was used to acquire 100 A-lines for measuring the transmit waveform and performing voltage vs. pressure calibrations. For beam mapping, the hydrophone was mounted to a motorized 3-axis motion stage, and a custom LabVIEW program was built to translate the hydrophone in the lateral-axial or the elevational-axial planes. The dimensions of the beam maps (axial x lateral) were (1 cm x 1 cm) for both transmit and receive for the DF-TRUS probe. All beam maps were performed with a step size of 0.125 mm in both dimensions. The transmit beam map was measured for the synthetic aperture, and the receive beam map were measured for the full aperture. The maximum resolution of each transducer was considered to be

the -6 dB full-width half-max (FWHM) of the receive beam maps. Since beam maps could not be measured for the EV-8C4 transducer, resolution comparisons were also made measuring on imaging the width of a 200 µm cellulose tube (see Section 7.2.vii).

### *7.2.iv In-Vitro Imaging*

Two in-vitro models were used for measuring SNR and CTR. All measurements were repeated with the Siemens EV-8C4 for benchmarking and comparison. The first in-vitro model consisted of a 200 µm diameter microcellulose tube bonded to polyethylene (PE20) tubing and mounted to an aluminum rod. The tube was suspended in de-ionized water and positioned at the focal depth of the transducer (Figure 7.3). The transducer was mounted to and positioned using a motorized 3-axis motion stage and controller.

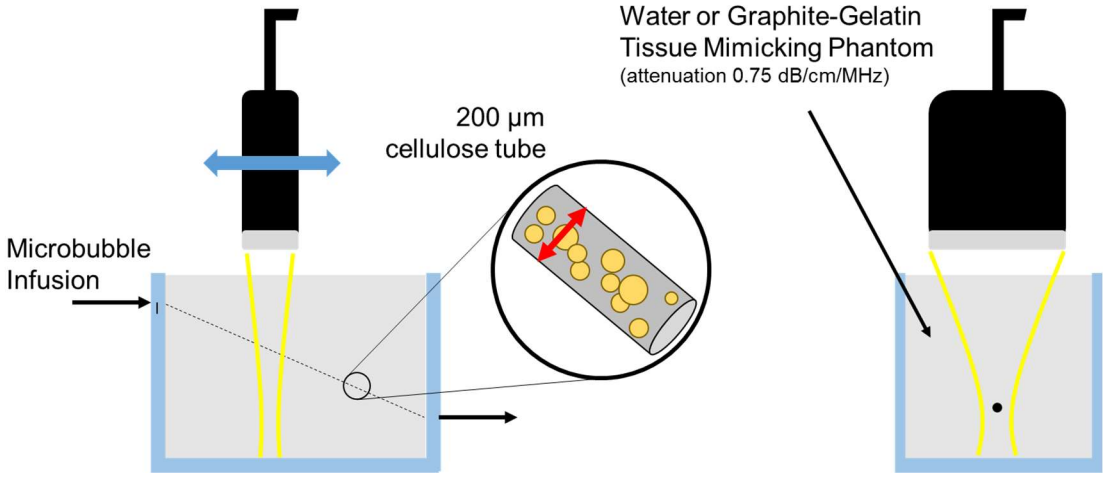


Figure 7. 3. Setup for in-vivo imaging. A 200 µm cellulose tube was suspended in either water or tissue mimicking phantom material for measuring SNR or CTR, respectively. The tube was infused with microbubble contrast agents.

SNR measurements were first recorded at varying transmit pressures ranging from 500-1000 kPa and calculated based on the unfiltered radio frequency (RF) data using the equation:

$$SNR_{dB} = 20 \times \log_{10}\left(\frac{V_{signal}}{V_{noise}}\right)$$

For comparisons between the DF-TRUS and EV-8C4 transducers, SNR was also measured based on the image data and normalized to the EV-8C4, as the standard for comparison. This second SNR calculation was performed since RF data for the EV-8C4 transducers were not available. The following equation was used:

$$SNR_{img} = \frac{Intensity_{signal}}{Intensity_{noise}}$$

All SNR measurements were acquired with microbubbles infused in the microcellulose tube.

Similarly, the second in-vitro model also consisted of a 200 μm diameter microcellulose tube, but was instead embedded in a tissue-mimicking graphite-gelatin phantom (Figure 7.3). An acrylic mold was fabricated and the cellulose tube was positioned across the length of the box at an angle to make a depth varying (10-25 mm) tube phantom. Once the tube was secured, the phantom filler was made and poured into the mold. The phantom filler consisted of 92.5% mL DI water, 5% mL n-propanol, and 2.5%  mL Kodak Photo-Flo 2000 (acts as a surfactant to produce formation of bubbles), and then 7.5% g/mL of laboratory grade porcine gelatin and 9.5% g/mL of graphite (acts as ultrasound scatterers). The attenuation of the phantom was approximately 0.75 dB/cm/MHz, close to reported values of attenuation for the human prostate [128]. A custom imaging bath was used to couple the transducer to the phantom and enable translation of the transducer with minimal application of ultrasound gel (Figure 4.1). Images

were acquired at varying transmit depths ranging from 5-25 mm and a constant pressure at approximately 1.1 MPa, which has been shown previously to produce sufficient superharmonic content for AA imaging [56].

CTR measurements were calculated similarly to the first in-vitro experiment, using two equations:

$$CTR_{dB} = 20 \times \log_{10}\left(\frac{V_{microbubble}}{V_{tissue}}\right)$$

$$CTR_{img} = \frac{Intensity_{microbubble}}{Intensity_{tissue}}$$

The equation for $CTR_{dB}$ was consistent with previous work published by Lindsey et al and Gessner et al [54,129]. All CTR measurements were made with microbubble contrast agent infused in the microcellulose tube. Microbubble contrast agent was diluted 100-fold to an approximate concentration of $1x10^8$ bubbles/mL.

### *7.2.v In-Vivo Imaging*

In-vivo animal imaging was performed with Fisher 344 rats with subcutaneous FSA tumors. Please refer to Section 5.2 for details on animal tumor implantation and imaging preparation methods. Microbubble contrast agent was diluted in a 1:1 ratio with sterile saline and infused at a rate of 40 μm/min, consistent with what was described previously.

The DF-TRUS transducers was mounted to a 3-axis motion stage (Newport, Irvine, CA) which was controlled using a custom LabVIEW program. The rat was positioned underneath the

transducer, and coupled with the transducer using ultrasound coupling gel and a custom imaging water bath.

Due to time limitation issues related to data transfer on the Verasonics, a larger step size (0.25 mm) was used for the DF-TRUS transducer, compared to what is normally used (0.10 mm) with the RMV VisualSonics transducer for AA. This was decided to limit the imaging and anesthesia time for the rat while maintaining a 2 cm scan length. A constant transmit pressure of approximately 1.1 MPa was used for in-vivo studies. Unprocessed radio-frequency (RF) data were removed off of the Verasonics, filtered, and then beamformed offline using Delay-and-Sum beamforming.

## 7.3 Results

### *7.3.i Acoustic Characterization Results of DF-TRUS Transducer*

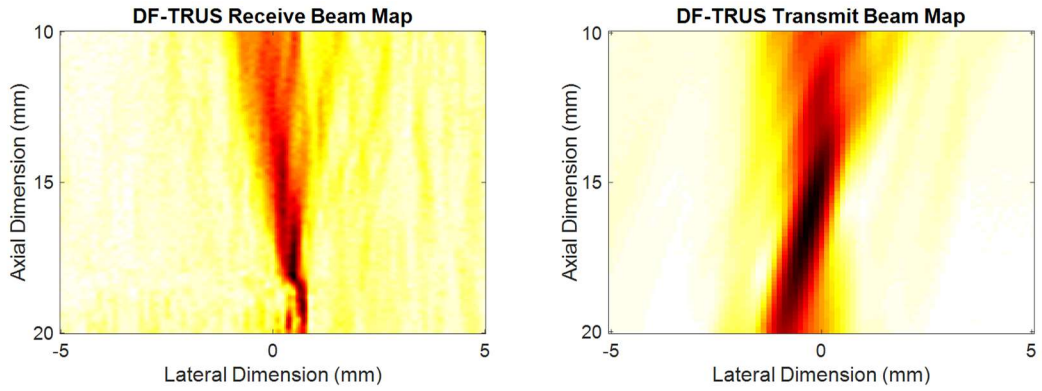


Figure 7. 4. Transmit (left) and receive (right) beam maps from the DF-TRUS transducer. The resolution of the transducer (210 µm) was determined by the FWHM of the receive lateral beam width.

The receive resolution of the DF-TRUS transducer, based on the -6 dB point on the receive lateral beam profile was measured at 210 µm, and the transmit beam width was measured at 640 µm. This is compared to the 130 µm resolution of the RMV probe, reported previously [56]. Using the Verasonics Vantage, a transmit voltage of 21.1 V was required to output a pressure of 1.07 MPa. Figure 7.5 shows the measured transmit waveform, centered at 3.125 MHz. For comparison, the RMV probe transmit waveform is provided (Supplemental Figure C.3). We can see that the pulse duration is significantly longer.

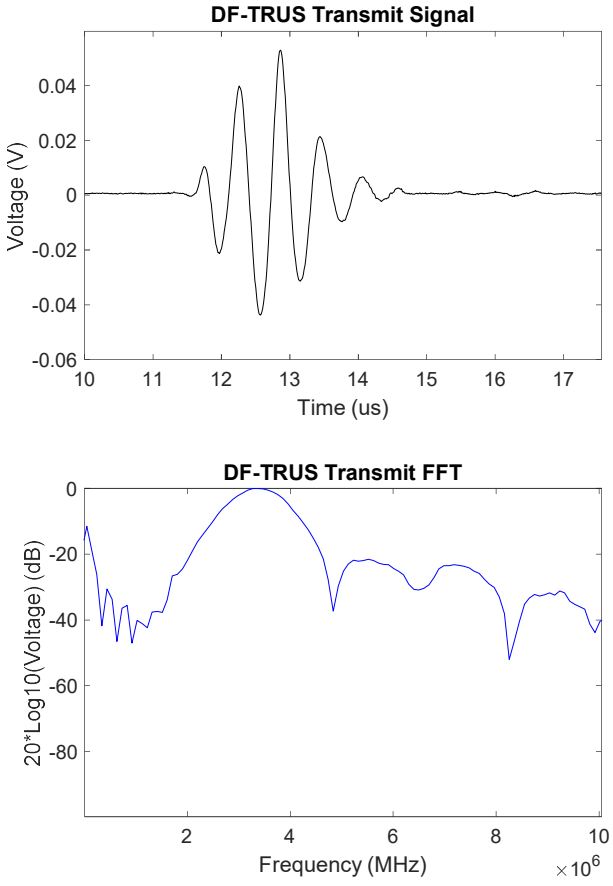


Figure 7. 5. The transmit waveform of the DF-TRUS centered at 3.125 MHz and the corresponding frequency spectrum.

### *7.3.ii In-vitro Experiment Results*

All resolution measurements were made using the -6 dB FWHM of the tube cross-section. The $SNR_{dB}$ of the DF-TRUS 19.25 dB. $SNR_{Img}$ was measured to be 0.86.

$CTR_{dB}$ measurements from the in-vitro tissue mimicking phantom experiment were measured to be 6.9 and $CTR_{Img}$ was measured to be 0.3 (Figure 7.7). The DF-TRUS probe had comparable $SNR_{Img}$ compared to the EV-8C4 probe, but considerably lower $CTR_{Img}$. Additionally, the DF-TRUS suffered from poor CTR at depths beyond 1.5 cm (Supplemental Figure C.5). All SNR and CTR values are summarized in Supplemental Table D.1.

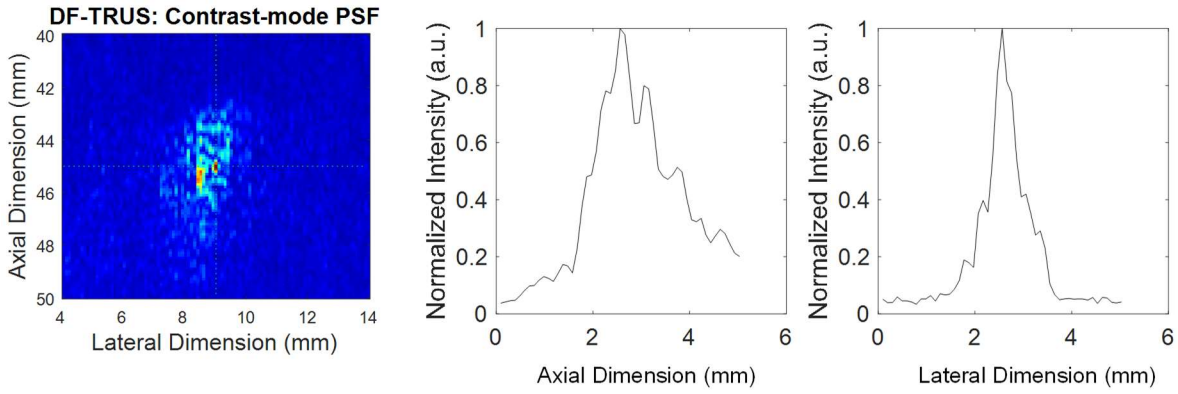


Figure 7. 6. Lateral and axial resolution measurements of a 200 µm cellulose tube in water measured by the DF-TRUS transducer. Dimensions were measured at 1400 µm and 600 µm, for the axial and lateral dimensions, respectively.

The axial resolution is considerably low compared to the lateral resolution, and is likely to be caused by the long pulse length of the transmit waveform (Figure 7.4). The DF-TRUS resolution is a slight improvement to the EV-8C4, primarily in the lateral dimension. (Figure 7.6).

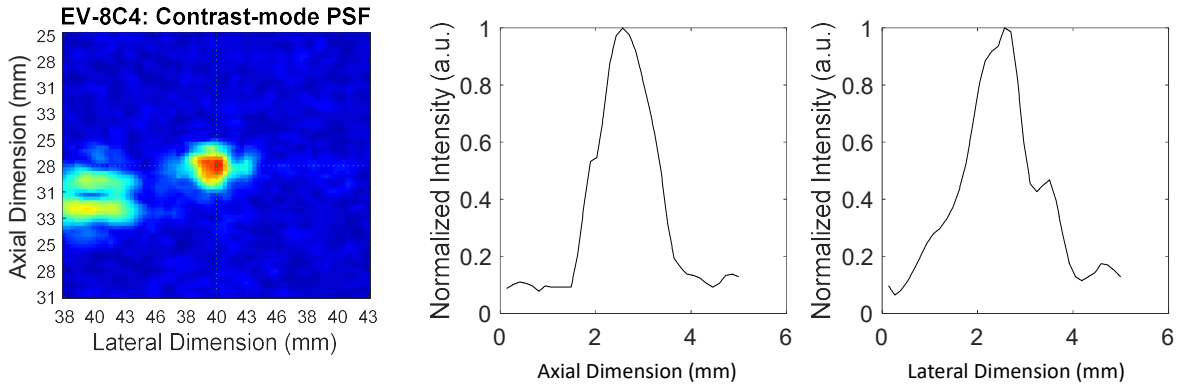


Figure 7. 7. Lateral and axial resolution measurements of a 200 µm cellulose tube in water measured by the EV-8C4 transducer. Dimensions were measured at 1500 µm and 1300 µm, for the axial and lateral dimensions, respectively.

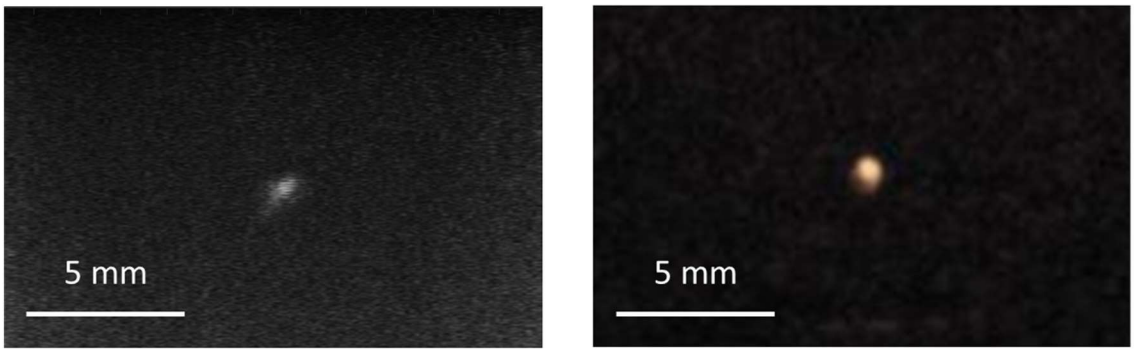


Figure 7. 8. Images of a 200 µm cellulose tube in a graphite tissue mimicking phantom. The bright signal in the lower part of the EV-8C4 image (right) is a specular reflection from the bottom of the acrylic mold. The CTRImg measured for the DF-TRUS transducer (left) is 0.3.

### *7.3.iii In-Vivo Results*

The DF-TRUS transducer was able to detect some microbubble superharmonic signal in-vivo, with a $CTR_{dB}$ of 3.2 dB (Figure 7.11). The in-vivo model that was used was the inguinal area of a rat, a highly vascular region, however the DF-TRUS was only able to detect signal from

the largest vessels in the area. While we detect some signal in-vivo, it is below an acceptable CTR compared to the EV-8C4. The contrast sensitivity is quite low shown by the inability to capture signal from smaller vessels. The vessels measured at approximately 1 mm x 1 mm in the axial and lateral dimensions.

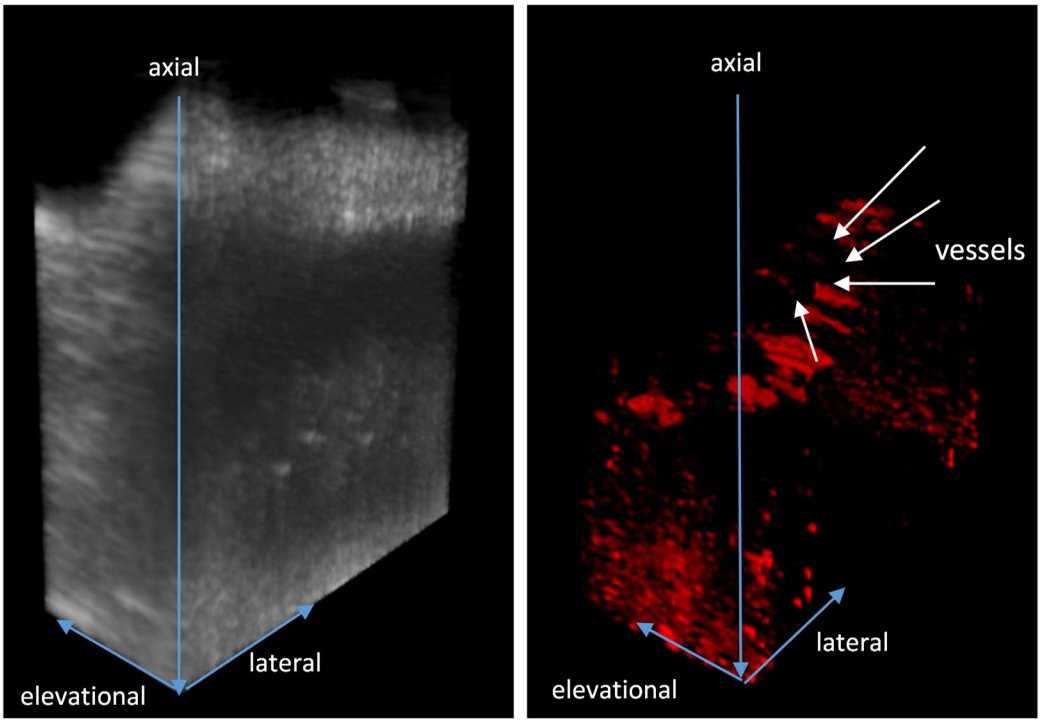


Figure 7. 9. 3D representation of the 3D image volume. Left is the B-mode reconstructed image, and right is the Acoustic Angiography reconstructed image. Vessels are identified with the white arrows. The imaging field was 25 mm x 10 mm x 10 mm (axial x lateral x elevational).

## 7.4 Discussion

The dual-frequency linear array prototypes described herein, has been demonstrated to detect superharmonic microbubble contrast signal in both in-vitro and in-vivo models. However, significant improvements are still needed to improve the overall performance. The CTR measured in-vivo was less compared to the in-vivo results. There are several potential reasons for this which will be discussed. The inguinal area that was imaged is a highly vascular region, however we were only able to detect a small number of large vessels, suggesting a very low contrast sensitivity. Additionally, a significant amount of tissue signal was present despite 10 MHz high-pass filtering, suggesting that the improvements can be made to reduce the bandwidth of the transmit pulse.

There are several design limitations that may have affected the imaging performance which can be improved in future studies. The array prototype was originally constructed without a full backing layer which we suspect affected the transmit bandwidth. From Figure 7.5, we can also see that the pulse length of the DF-TRUS transducer is significantly longer (2x) than the RMV (Supplemental Figure C.3) probe, reducing axial resolution and transmission sensitivity. Adding a backing layer will likely decrease harmonic content while shortening the pulse.

The reason for the discrepancy between the in-vitro and in-vivo CTR is likely that the microbubble concentration used for in-vitro experiments was greater than what was used in-vivo. Additionally, the elevational foci of the transmit and receive arrays were largely separated (~40 mm separation), reducing the alignment of the focused beams. This mismatch results in a wider elevational beam and may have affected vessel detection of less linear vessels in-vivo (in

contrast to the straight tube used in-vitro). The electrical wiring may have also contributed to system and image noise. Since a custom Verasonics adapter was manually soldered, many of the wires were not completely shielded and unconnected wires were sealed but not insulated. It was hypothesized that the Verasonics pulse driving sequence could be improved to reduce the pulse length of the transmit waveform, however no improvements could be made. A shorter single cycle pulse was both simulated and achieved, however this produced even higher frequency content than before.

A linear array design was preferred for the DF-TRUS prototype since it is easier to design and implement. However one of the disadvantages for linear array imaging is a limited field of view for imaging. The current design has an aperture size of approximately 18 mm. This field of view is significantly limited and is not sufficient for imaging prostates that are frequently enlarged beyond 200 cc (4-6 cm) from BPH or PCa. The aperture is comparable to the EV-9C4 transducer, however the Siemens probe operates as a curvi-linear array. Phased array imaging may be a better alternative for enlarged prostate imaging. Additionally, a lower transmit and receive frequency combination can be used for increased penetration. In fact, Lindsey et al determined that maximum superharmonic energy is generated with a transmit frequency of 2 MHz and a maximum CTR is achieved with a receive frequency of 10 MHz [129]. Future iterations of the DF-TRUS design will be improved upon based on these recommendations.

While the image quality of the DF-TRUS cannot yet be compared to the commercially available EV-8C4 transducer, the initial in-vitro results coupled with the fact that there are achievable improvements that can be made to in future design iterations are promising for significantly improving the performance.

## 7. 5 Conclusions

There is a potential need for improved PCa detection and biopsy guidance using ultrasound imaging. Current ultrasound techniques (b-mode and CEUS) suffer from low specificity to PCa malignancy. AA is sensitive to measuring differences in tumor microvasculature compared to normal tissue and it is also sensitive to measure *changes* in certain microvascular features. This technology has the potential to improve the specificity of diagnosis and ultrasound guided prostate biopsy.

Despite many successful preclinical studies, clinical translation of AA requires the transition to an array-format type transducer for increased depth of penetration and faster image acquisition. The prototype DF-TRUS transducer is the first dual-frequency transducer of the stacked configuration type for superharmonic imaging and the results from the first design iteration of the array are promising. The work described in this chapter intends to bring AA one step closer to clinical use.

# CHAPTER 8:

# Proof of Concept Dual-Probe/Dual-Frequency Transducer for AA

## 8.1 Overview

We previously demonstrated the feasibility of using a stacked type design for linear arrays for performing AA. Although initial in-vivo results demonstrated low CTR and contrast sensitivity, there is significant room for improving the design and imaging performance in future iterations. However, since linear array transducer manufacturing is challenging in a laboratory setting, it is difficult to fully assess the potential of dual-frequency, linear array AA and its benefit over conventional CEUS. Difficulties in array fabrication and electrical shielding of the electronic components results in lower SNR and potentially can be avoided in a commercial setting. In order to better assess this advantage, we will demonstrate a proof-of-concept dual-probe/dual-frequency (DP-DF) for superharmonic imaging using two separate commercially available linear arrays transducers. This new proof-of-concept may help in modifying design and imaging specifications for the future redevelopment of the DF-TRUS transducer described previously. Therefore, the primary objectives are 1) to demonstrate the full potential for linear array dual-frequency for superharmonic imaging in in-vitro and in-vivo model and 2) compare the performance to both the Siemens EV-8C4 transducer, and the RMV probe used previously for all pre-clinical AA imaging.

## 8.2 Methods

### *8.2.i Verasonics Coding*

For DP-DF imaging, two Verasonics systems were used. First, a Verasonics V1 system was used for the low frequency transmit, and a Verasonics Vantage 256 was used for the high-frequency receive. The transmit and receive frequencies were selected at 2.5 MHz and 15.625 MHz, respectively, with a maximum sample rate of 62.5 MHz. 77 transmit ray lines were specified based on the lateral transmit beam width, with 77 corresponding receive events. The transmit coordinate system was based on the high frequency transducer aperture. The synthetic aperture size for each transmit ray line was calculated based on the specified focal depth (between 10-30 mm) and the F-number (1), and ranged from 10-30 elements. The linear array imaging sequence was the same for both DF-TRUS and DP-DF. MATLAB Verasonics scripts were developed for linear array imaging using both transducers.

### *8.2.ii DP-DF Set-up*

The DP-DF transducer consisted of two commercially available transducers, mechanically clamped so that their transmit/receive beams overlapped at a specified acoustic focus. An ATL P4-1 linear phased array transducer was used as the low frequency transmit array, and a VisualSonics MS250 linear array transducer was used for the high frequency receive array.

Each transducer was digitally scanned using a NextEngine 3D laser scanner (NextEngine, Santa Monica, CA), and then custom molded clamps were designed using the computer-aided design software (SolidWorks, Dassault Systèmes, Waltham, MA) and 3D printed on a uPrint SE

(Stratasys, Prairie, MN). The transducers were angled at 30.78° in order to converge their transmit/receive beams at approximately 25 mm (Figure 8.1).

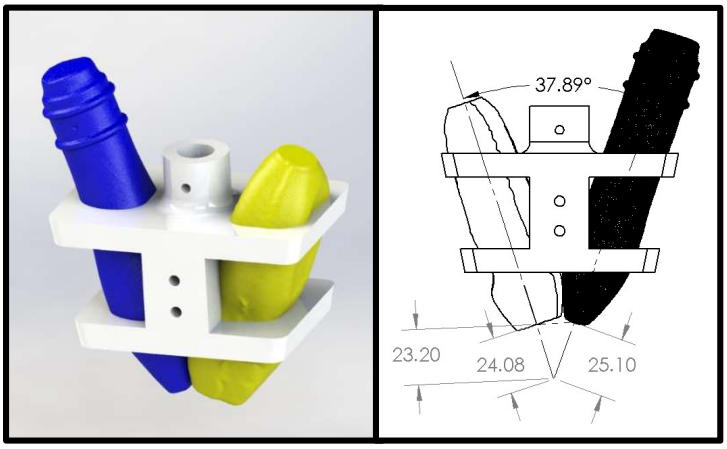


Figure 8. 1. 3D modeling of the transmit and receive transducers for the DP-DF configuration. An angle of approximately 38 degrees ensured the foci of both transducers overlapped around 2.5 cm in depth. The design is programmed to be adjusted for any desired depth imaging. In the future, additional depths will be trialed (>5-6 cm).

The P4-1 and MS250 transducers have 96 and 256 elements, respectively. Due to the large number of elements, two Verasonics systems were necessary for DP-DF imaging; a Verasonics V1 system was used for low frequency transmit, and a Verasonics Vantage 256 system was used for high frequency receive. A Universal Transducer Adapter (UTA) with 360 pins was used to interface the MS250 with the Vantage system.

### *8.2.iii Acoustic Characterization*

The transmit waveforms, pressures, and acoustic beam maps were measured for the DP-DF transducers. Waveform measurements and beam mapping were recorded using a needle hydrophone, similar to what was described in Section 7.2.iv. The dimensions of the beam maps (axial x lateral) were (1 cm x 3 cm) and (0.5 cm x 0.5 cm) for transmit and receive, respectively, for the DP-DF probe. All beam maps were performed with a step size of 0.125 mm in both

dimensions. The transmit beam map as measured for the synthetic aperture, and the receive beam map was measured for the entire aperture. The maximum resolution of the transducer was considered to be the -6 dB FWHM of the receive beam width. All measurements were repeated for the RMV probe. Since beam maps could not be measured for the EV-8C4 transducer, resolution comparisons were also made measuring on imaging the width of a 200 μm cellulose tube (see Section 8.2.vii).

### *8.2.iv In-Vitro Imaging*

Two in-vitro models were used for measuring SNR and CTR. All measurements were repeated with the Siemens EV-8C4 and Vevo 770 RMV transducers for benchmarking and comparison. The first in-vitro model consisted of a 200 μm diameter microcellulose suspended in water, and the second model consisted of a second microcellulose tube suspended in a tissue mimicking graphite-gel phantom (consistent to what was described previously in Chapter 7). $SNR_{dB}$ and $CTR_{dB}$ measurements for the DP-DF transducer were calculated by the filtered RF data, and was compared to $SNR_{Img}$ and $CTR_{Img}$ measured by the EV-8C4 and RMV image data, as previously described.

All SNR and CTR measurements were made with microbubble contrast agent infused in the microcellulose tube. Microbubble contrast agent was diluted 100-fold to an approximate concentration of $1x10^8$ bubbles/mL.

### *8.2.v In-Vivo Imaging*

In-vivo animal imaging was performed with Fisher 344 rats with subcutaneous FSA tumors. Please refer to Section 5.2 for details on animal tumor implantation and imaging preparation methods. Microbubble contrast agent was diluted in a 1:1 ratio with sterile saline and infused at a rate of 40 μm/min, consistent with what was described previously. Imaging was performed on two consecutive days (DP-DF on the first day, and EV-8C4/RMV on the second day) as to limit the total contrast dose and anesthesia time for the rat.

The EV-8C4 and DP-DF transducers were mounted to a 3-axis motion stage (Newport, Irvine, CA) which was controlled using a custom LabVIEW program. The RMV probe was controlled using the Vevo 770 system which has its own precision motion stage (VisualSonics, Toronto, CA). The rat was positioned underneath the transducer, and coupled with the transducer using ultrasound coupling gel and a custom imaging water bath. Table 7.1 summarizes the imaging parameters for each imaging system.

Table 7. 1 In-vivo Imaging Parameters

| | ***RMV*** | ***DP-DF*** | ***EV-8C4*** |
|---|---|---|---|
| ***Elevtational Step Size (mm)*** | 0.100 | 0.25 | 0.25 |
| ***Scan Length (mm)*** | 20 | 20 | 20 |
| ***Frame Averaging*** | 2 | 2 | 0 |
| ***Frame Rate (Hz)*** | 3 | 7 | 14 |
| ***# of Tx Ray Lines*** | | 77 | unknown |
| ***Tx Focus (mm)*** | 16 | 25 | 25 |

Due to time limitation issues related to data transfer on the Verasonics, a larger step size (0.25 mm) was used for DP-DF transducers compared to the RMV transducer (0.10 mm) to limit the imaging time while maintaining a 2 cm scan length. A constant transmit pressure of

approximately 1.1 MPa was used for both the DP-DF and RMV transducers (except for the EV-8C4—the transmit pressure was unknown). The DP-DF unprocessed radio-frequency (RF) data were removed off of the Verasonics, filtered, and then beamformed offline. Image data was directly taken from the Vevo 770 and Sequoia scanners for the RMV and EV-8C4 transducers, respectively.

### *8.2.vi Image Processing and Analysis*

DP-DF RF data were filtered using a finite-impulse response high-pass filter with a cut-off frequency at 10 MHz and beamformed using the Delay-Multiply-And-Sum (DMAS) technique [130]. Since RF data was not available for the RMV and EV-8C4 probes for signal based CTR measurements, CTR was alternatively measured based on image intensity dividing the signal intensity of contrast perfused tissue by the baseline tissue noise, and normalized to the EV-8C4, which was used as the standard for comparison.

## 8.3. Results

### *8.3.i Acoustic Characterization Results*

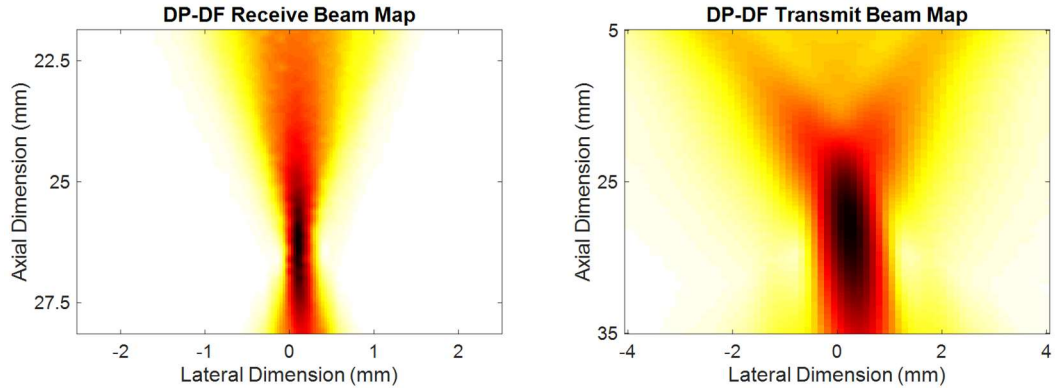


Figure 8. 2. Transmit (left) and receive (right) beam maps from the DP-DF transducer. The resolution of the transducer (220 µm) was determined by the FWHM of the receive lateral beam width.

The receive resolution of the DP-DF transducer was measured at 220 µm, and the transmit beam width was measured at 950 µm (Figure 8.2). Using the Verasonics V1, a transmit voltage of 28.2 V was required to output a pressure of 1.04 MPa. A co-alignment beam map shows that the beams intersect approximately at 35 mm (Figure 8.3).

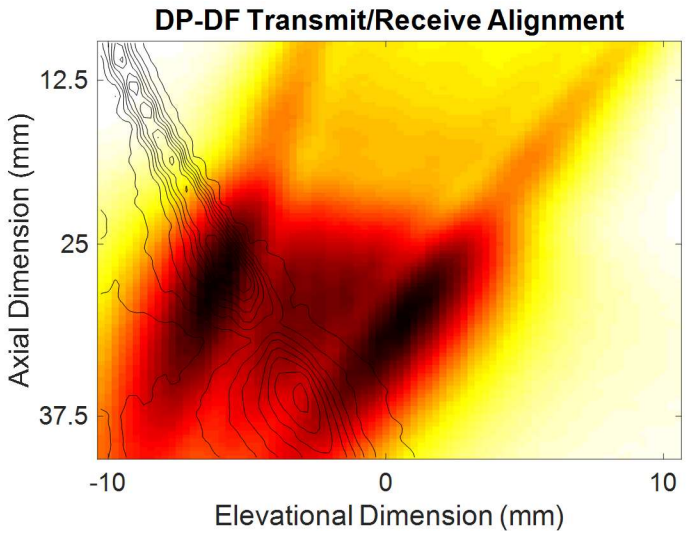


Figure 8. 3. An alignment beam map of the DP-DF transducer in the elevational-axial plane. The true focus of the transducer is closer to 35 mm from the faces of the transducers. The wide elevational beam width is apparent.

From the co-alignment beam map, we can see that the elevational beam profile of the low frequency P4-1 transducer has two significant side lobes, with slightly less pressure in the main lobe (1.5 dB less). The transmit waveform of the DP-DF transducer, centered at 2.5 MHz is shown in Figure 8.4.

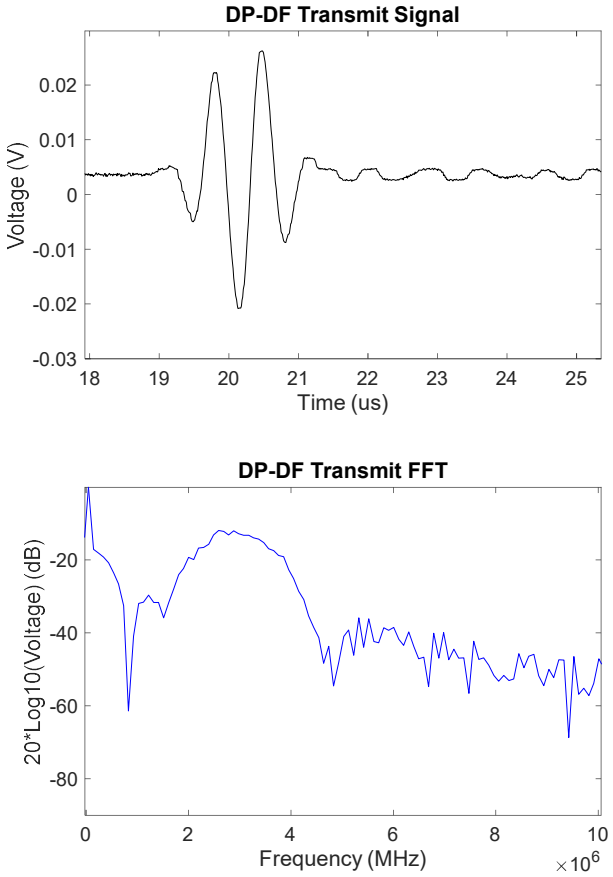


Figure 8. 4. The transmit waveform of the DP-DF transducer centered at 2.5 MHz and the corresponding frequency spectrum.

### *8.3.ii In-vitro Experiment Results*

In the first in-vitro setup while in contrast imaging mode, the 200 µm cellulose tube was measured [laterally, axially] to be [1400 µm, 600 µm], [500 µm, 500 µm], and [1300 µm, 1500 µm] by the DP-DF, RMV, and EV-8C4 transducers, respectively. All measurements were made using the -6 dB FWHM of the tube cross-section. The $SNR_{dB}$ of the DP-DF transducer was measured to be 24.05 dB, respectively. $SNR_{Img}$ was measured to be 3.66 and 2.6, for the DP-DF and RMV probes, respectively.

$CTR_{dB}$ measurements from the in-vitro tissue mimicking phantom experiment were measured to be 16.6 dB with the DP-DF transducer. $CTR_{Img}$ was measured to be 1.1, and 2.2 for the DP-DF, and RMV transducers, respectively. The DP-DF transducer measured the highest SNR compared to the other three transducers and displayed comparable CTR with previously reported $CTR_{dB}$ values for the RMV probe. All SNR and CTR values are summarized in Supplemental Table D.1.

### *8.3.iii In-vivo Results*

Tumor images from the DP-DF, RMV, and EV-8C4 transducers are shown Figures 8.5 and 8.7). The RMV transducer produce an image consistent with previous studies, with vessels as small as 200 μm being detected and a $CTR_{Img}$ of 4.5. The EV-8C4 image shows exceptional contrast sensitivity as seen by the ability to detect contrast signal in the center of the tumor, however lower CTR, as seen by the baseline (non-contrast) image (Figure 8.5). The DP-DF also showed high contrast sensitivity and low tissue signal, with a $CTR_{Img}$ of 1.53. The DP-DF images showed in Figures 8.5 and 8.7 are temporally compounded with 2 frame averaging. When we compare frame averaging with a single, no averaged slice, we see significant contrast sensitivity, specifically in the middle of the tumor, comparable to the EV-8C4 transducer (Figure 8.6).

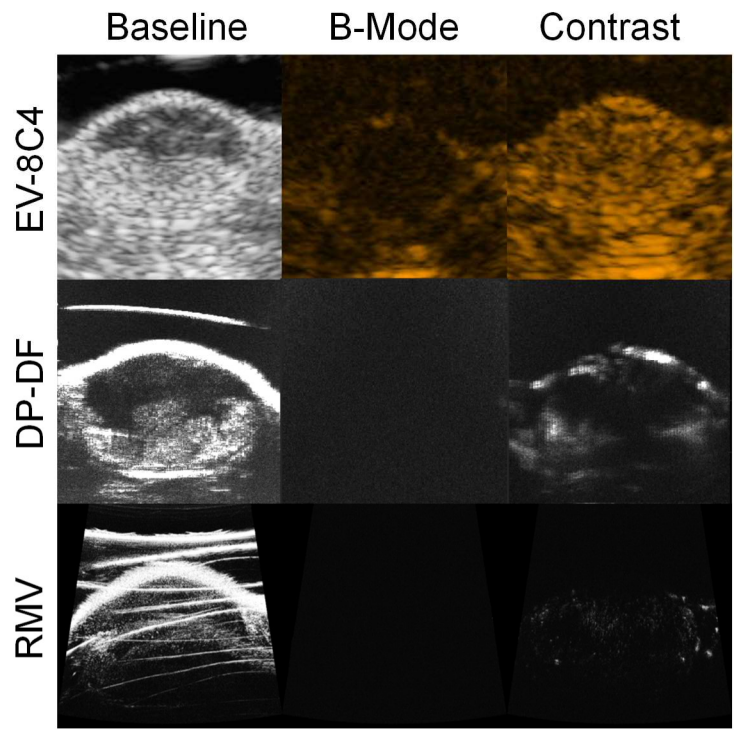


Figure 8. 5. In-vivo images from the DP-DF, RMV, and EV-8C4 transducers. B-mode, baseline, and contrast infused images are shown to compare differences in CTR and contrast sensitivity.

3D reconstruction and maximum intensity projection (MIP) of the image stacks acquired by the DP-DF transducer shows clear vessel structure that agree with the RMV images. The smallest vessel detectable by the RMV and DP-DF transducers was 175 µm and 320 µm, respectively. Upon closer examination, we can clearly identify common vessels in both coronal MIPs.

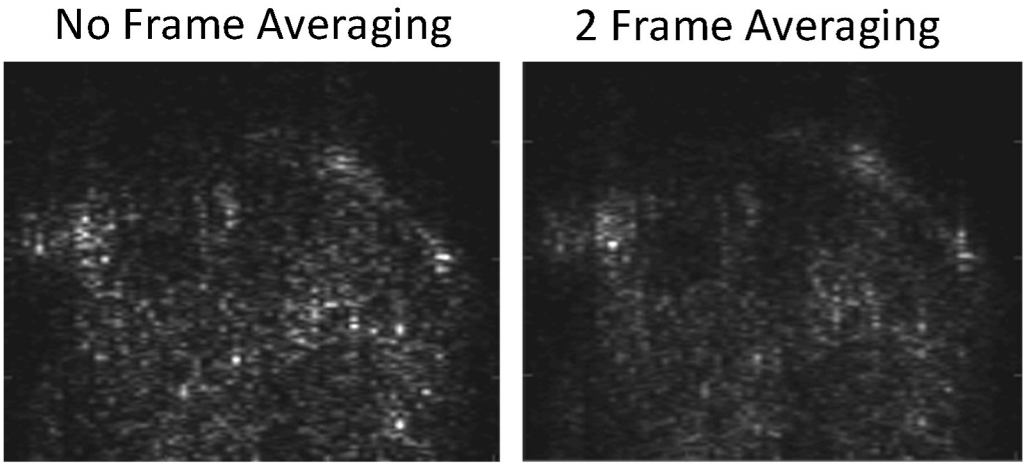


Figure 8. 6. A Comparison of frame averaging versus no frame averaging using the DP-DF transducer. The 0-frame averaging image shows comparable contrast sensitivity to in regions not detected after significant frame averaging or by the RMV probe.

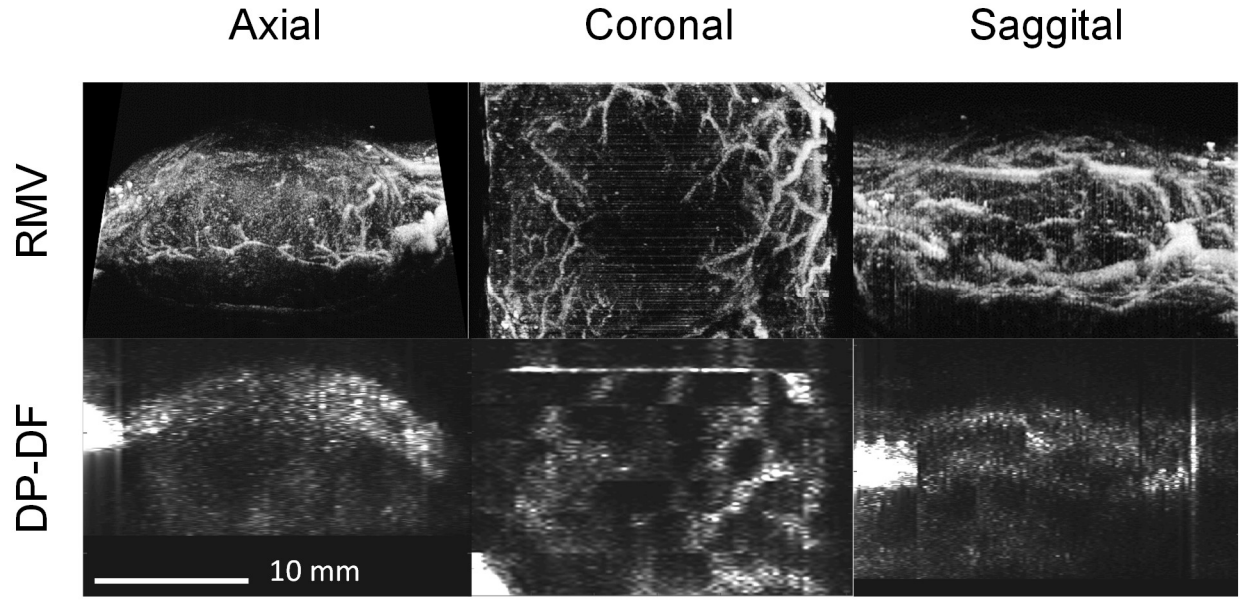


Figure 8. 7. MIPs of the DP-DF probe compared with the RMV probe of the same FSA tumor. Identical vessels can be identified in both of the coronal MIPs. The elevational resolution is significantly less for the DP-DF transducer due to the larger step size (0.25 mm vs 0.1 mm), and the wide transmit beam width.

## 8.4 Discussion and Conclusions

Since many of the manufacturing limitations in a laboratory environment described in Chapter 7, which likely impacted the performance of the DF-TRUS transducer, can be solved in a commercial environment (i.e. application of a lens to account for varying elevational foci, design of a small form-factor electrical adapter, etc) it is difficult to fairly assess the full benefit of linear array superharmonic imaging. As a supplement to the DF-TRUS probe, we demonstrated a proof-of-concept "dual-frequency linear array" by using two separate commercially available transducers. The usefulness of this approach is that we can better assess the capability of linear array imaging by removing manufacturing limitations out of the equation.

The frequencies for the DP-DF transducer were selected similarly to the DF-TRUS, except with a lower transmit frequency (2.5 MHz) to maximize the transmit sensitivity of the P4-1 transducer. The center frequency of the receive transducer was approximately 6 harmonics above the transmit frequency. The configuration of the transducers was such that a single fixed focus was required (which made multi-focus imaging impossible with the current design). A focus of 2.5 cm was chosen to so that we can demonstrate deeper imaging capability compared to the RMV probe, which is limited to 1.5 cm. We have yet to demonstrate feasible imaging depths relevant for prostate imaging. However, the alignment beam map showed that the true aligned depth of both transducers was closer to 3 cm, deeper than we had designed for. At these imaging parameters we were able to detect and resolve vessels in-vivo, which to our knowledge, has not been previously demonstrated using linear array superharmonic imaging. While we stayed fixed within 3 cm for DP-DF imaging, we can clearly see improved depth of field compared to the RMV transducer, specifically at the top and bottom regions of the tumor (Figure 8.7).

As a proof-of-concept, these results are very promising and certain fundamental limitations in the design can be easily improved upon in future iterations to achieve higher resolution and greater CTR. First, the low frequency transducer was a linear phased array probe programmed to image in linear array mode. Since it is designed for phased array imaging, the natural focus is significantly deeper compared to the high frequency receive. The alignment beam map clearly shows the wide elevational beam width with large side lobes. This significantly reduces the transmit sensitivity at the desired focus of 25 mm. Additionally, for deeper imaging we lose receive sensitivity of the high frequency transducer due its shallow elevational focus. It will be challenging in future iterations to find both low and high frequency, commercially available transducers with matched elevational foci. A potential solution might be to offset the low frequency transducer to match the maximum elevational focus of the high frequency transducer, however this will further increase the transmit beam width laterally, reducing contrast sensitivity.

The Verasonics imaging scripts can also be improved to drastically speed up the imaging procedure, allowing us to capture more slices with a finer elevational step size, and more frames per slice for temporal averaging and/or angular compounding. This amendment will improve elevational and lateral resolution, as well as CTR. While we have demonstrated preliminary capabilities that this proof-of-concept dual frequency array can perform microvascular imaging, for prostate imaging the challenge still exists that both sets of arrays eventually will need to be co-aligned and in the form factor for transrectal imaging.

As mentioned previously, while the stacked type configuration is a novel approach for superharmonic imaging that holds promise for realizing linear array AA, an alternative approach to AA for high-resolution microvascular imaging is ultrasound localization microscopy. This

CEUS approach requires only a single linear array and promises resolution beyond the diffraction limit of ultrasound [106,131]. While the design specifications for super resolution imaging may be simpler, the disadvantages lie in the significantly long image acquisition times for volumetric imaging due to the large number of frames (>1000) required for a single slice. Until the image acquisition times can be shortened for super resolution imaging (either by faster frame rates or development of higher resolution 2D arrays for CEUS), the dual-frequency linear array approach appears to be the most promising for clinical translation of high-resolution microvascular imaging.

While high-resolution microvascular imaging may be beneficial for prostate imaging, due to the required depth of penetration (4-6 cm), we begin to be challenged by the trade-off between imaging depth and imaging frequency. With increased imaging depth we require lower transmit and receive frequencies and therefore sacrifice resolution. Fortunately, with AA, there is only one-way high frequency attenuation (on receive) since the transmit frequency is designed to be low and experiences less attenuation. Based on preliminary data that we can detect microbubble signal as deep as 6.5 cm using the DP-DF configuration at 15.625 MHz, we can theoretically achieve imaging depths of up to 9.75cm if we reduce our receive frequency to 10 MHz. As mentioned previously, maximum superharmonics are generated with a transmit frequency of 2 MHz and a maximum CTR is achieved with a receive frequency of 10 MHz [129]. In the future, choosing two transducers within these frequency combinations might allow us to further improve microbubble detection at depth.

To date, the ability to achieve resolutions for detecting individual vessels at depths greater than 4 cm is yet to be determined. Even so, the technique for superharmonic imaging is inherently more sensitive to microbubble contrast signal than conventional CEUS techniques,

which may prove to be beneficial in detecting changes in tissue perfusion with higher sensitivity even without the resolution of what we are used to seeing with AA.

## 8.5 Future Work

In addition to reiterating of the DF-TRUS prototype design, investigating a clinically relevant prostate tumor model with AA will give insight into what types of microvascular information is most important for both prostate lesion detection and malignant cancer diagnosis, and may help tailor the development of DF-TRUS. A pre-clinical tumor model, the Dunning R3327-AT2 rat prostate tumor grown in Copenhagen rats, is a slow growing, androgen dependent tumor model which has been shown to be an appropriate model for PCa research [132,133].

As stated previously, increased depth of penetration using AA imaging has yet to be demonstrated. Current work is in progress for determining the maximum depth (>6.5 cm) at which the DP-DF configuration can detect microbubble contrast signal with relevant SNR and CTR values.

# APPENDIX A:

# A Quantitative Approach to Characterizing Malignant Renal Cell Carcinoma Using Contrast Enhanced Ultrasound[2]

## A.1 Introduction

Renal cell carcinoma (RCC) affects approximately 1 in every 100 American individuals, with an estimated 62,000 new cases to be diagnosed in 2016 in the United States alone [134]. Classification of RCC has evolved over the last three decades, leading to four main subtypes: clear cell, papillary type I, papillary type II, chromophobe. Clear cell RCC is the most common (~75%) type of RCC, followed by papillary (~16%) and chromophobe (~7%). Each of these tumors has been recently characterized genetically by the cancer genome atlas, underscoring the unique biology of each disease type [135–137]. RCC classification is a critical diagnostic step since clinical management is based on the varying prognoses and therapeutic pathways of each subtype [138]. Clear cell and papillary type II RCCs have a higher probability of metastasizing even after nephrectomy for organ-confined tumors, while the prognosis for papillary type I and chromophobe RCCs are significantly better and are therefore managed more conservatively compared to clear cell RCC [139,140]. Radiographic distinction between these malignant RCC subtypes is inherently difficult due to molecular aberrations and structural contributions that lead to shared tumor morphology [141].

[2] This chapter previously appeared as an article in the Journal of Ultrasonic Imaging. The original citation is as follows: *Kasoji SK, Chang EH, Mullin LB, Chong WK, Rathmell WK, Dayton PA. A Pilot Clinical Study in Characterization of Malignant Renal-cell Carcinoma Subtype with Contrast-enhanced Ultrasound. Ultrason Imaging. 2017;39(2):126-136.*

Traditional gray-scale ultrasound is effective for differentiating solid from cystic kidney lesions, but lacks the sensitivity to further classify solid masses according to histologic type. Contrast-enhanced computed-tomography (CT) and magnetic resonance imaging (MRI) are the standard imaging exams used to assess the malignancy of solid masses and to characterize perfusion patterns; however, the contrast sensitivity does not adequately resolve histologic characteristics of many types of tumors arising in the kidney, including hypovascular and cystic lesions, necrosis, debris and hemorrhagic areas in tumors [142]. Additionally, the nephrotoxicity of the contrast agents often limits their use [143]. Thus, tissue analysis, often post-nephrectomy, has remained the gold standard for identifying RCC subtypes despite the invasive nature of the procedure.

Recent clinical studies have shown that contrast-enhanced ultrasound (CEUS), a non-nephrotoxic and non-ionizing imaging modality, has the ability to assess malignancy of solid and cystic kidney lesions based on qualitative enhancement and perfusion patterns [144]. Only a few studies, however, have considered quantitative approaches to further characterize RCC subtypes [140,145–148]. In this study, we quantify perfusion patterns in 12 patients diagnosed with kidney masses and correlate specific metrics with pathologic findings.

## A.2 Materials and Methods

### *A.2.i Patient Recruitment and Initial Tests*

University of North Carolina's Institutional Review Board approved this study and written informed consent was obtained from each patient prior to the study. Over a two-year period, twenty-four individuals diagnosed with kidney lesions were recruited for the study and imaged with contrast-enhanced ultrasound (CEUS). All patients were imaged using traditional ultrasound and either CT or MRI prior to CEUS, and tissue biopsy or resection was performed on 22 of the 24 patients post-CEUS. Histologic analyses were performed on all 22 patients and classified by expert clinical pathologists as clear cell RCC (ccRCC, n=15), papillary RCC (pRCC, n=3), chromophobe RCC (chRCC, n=2), angiomyolipoma (AML, n=1), or oncocytoma (OCT, n=1). AMLs and OCTs were excluded from the study as benign tumors. Eight of the twenty-two patients were excluded from quantitative analysis due to poor video quality caused by excessive out-of-plane motion (displacement greater than half the size of the lesion of interest) and inadequately visible parenchyma (less than a 5 $mm^2$ ROI). Therefore, the remaining 12 were included in the final analysis. Two patients underwent core biopsies, while the remaining 10 underwent partial or complete nephrectomy.

### *A.2.ii Contrast-Enhanced Ultrasound*

CEUS imaging was performed on a Siemens/Acuson Sequoia 512 (Mountain View, CA, USA) by a trained sonographer. Traditional b-mode ultrasound clips were first recorded for each patient to determine the anatomical location and dimensions of the lesion. The transducer was optimally positioned so that the lesion and normal parenchyma (renal cortex) were clearly visible

and so that breathing motion was maintained within the plane. After the sonographer localized the lesion of interest and was able to maintain a consistent image along with patient breathing, a mechanical stereotactic clamp was fixed to maintain the transducer position. The clamp was introduced to help minimize sonographer hand motion during acquisition of the cine loop and to alleviate physical cramping of the wrist during the long imaging period. The depth and spacing of the imaging foci were adjusted to the center on the lesion based on the lesion size and depth. Cadence Pulse Sequence (CPS) mode was used for contrast imaging at a mechanical index (MI) of 0.19. A 5 mL bolus injection of the diluted microbubble contrast agent, Definity (Lantheus, North Billerica, MA, USA), was administered through the antecubital vein over 15 seconds, followed by a 5 mL flush of 0.9% saline. Contrast dose was based on patient weight (0.5 mL for <125 lb, 0.65 mL for 125-185 lb, 1.0 mL for >185 lb). Image acquisition was initiated immediately prior to the bolus injection and ended after 3 minutes, capturing contrast wash-in and at least 2 minutes of contrast wash-out.

### *A.2.iii CEUS Time-Intensity-Curve Analysis*

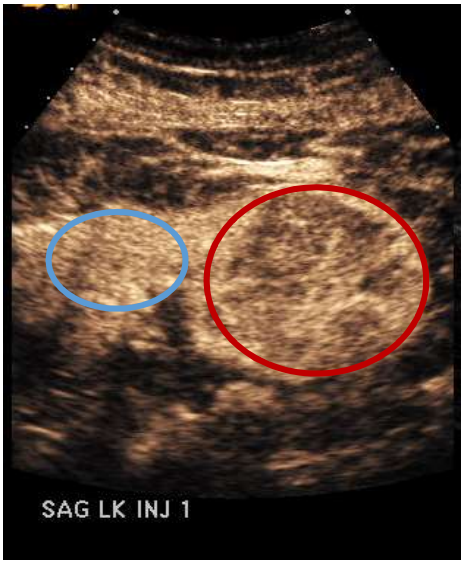


Figure A. 1. Ellipsoidal ROI selection of both the lesion (red) and normal renal cortex (blue). ROIs were draw with a minimum diameter of 5mm, and parenchyma and lesion ROIs were drawn at approximately the same depth (±1 cm).

DICOM files containing the b-mode and contrast clips were copied from the Sequoia 512 and converted to audio-video interleave files for subsequent analysis using ImageJ (National Institutes of Health, Bethesda, MD, USA) and MATLAB (MathWorks, Natick, MA, USA). Clips that contained severe out-of-plane breathing and body motion were omitted from quantitative analysis. In the instances where breathing motion was regular and cyclic, a targeted ROI for the lesion and parenchyma was selected whenever it appeared in plane. Rigid image registration was performed using the StackReg plugin for ImageJ to correct in-plane breathing motion. Ellipsoidal regions-of-interest (ROI) with a minimum diameter of 5 mm were selected for the lesion and the renal cortex separately at approximately the same depth (±1 cm) (Figure A.1).

Lesion ROIs were selected to encompass the entire lesion excluding the normal parenchyma. Time-intensity-curves (TIC) were generated for all ROIs. Any cystic and necrotic regions that were present were excluded in the ROI selection. Residual breathing motion was further removed by filtering the TICs in MATLAB using a low pass filter ($f_{-3dB}$ = 0.025 Hz). Ten metrics were applied to each of the TICs, including peak contrast intensity (PI), time-to-peak (TPk), time-to-peak ratio (TPk-r), time-to-80% on wash-out (T80%), time-to-80% on wash-out ratio (T80%-r), wash-in slope (WIS), wash-out slope (WOS), wash-in ratio (WIS-r), wash-out ratio (WOS-r), and wash-in/wash-out ratio (WIWOS-r). The metrics are described below and graphically summarized in Figure A.2 and Table A.1. Time-to-80% was estimated based on the inflection point of the decay phase of the gamma variate function ($y = A \cdot t \cdot \left(1 - e^{-\beta t}\right) + C$), which is approximately at 75% of the peak intensity. Peak contrast intensity was measured with non-normalized data, which is not shown in Figure A.2.

Table A. 1. Definitions for metrics used for TIC analysis.

| Metric | Definition |
|---|---|
| Peak contrast intensity ratio | Ratio of peak intensity (lesion/parenchyma) |
| Time-to-peak | Time to peak intensity of lesion |
| Time-to-peak ratio | Ratio of time to peak intensity (lesion/parenchyma) |
| Time-to-80% | Time from peak intensity to 80% on wash-out for lesion |
| Time-to-80% on wash-out ratio | Ratio of the time from peak intensity to 80% on wash-out (lesion/parenchyma) |
| Wash-in slope | Wash-in slope of lesion |
| Wash-out slope | Wash-out slope of lesion |
| Wash-in ratio | Ratio of wash-in slopes (lesion/parenchyma) |
| Wash-out ratio | Ratio of wash-out slopes (lesion/parenchyma) |
| Wash-in/Wash-out ratio | Ratio of wash-in to wash-out of lesion |

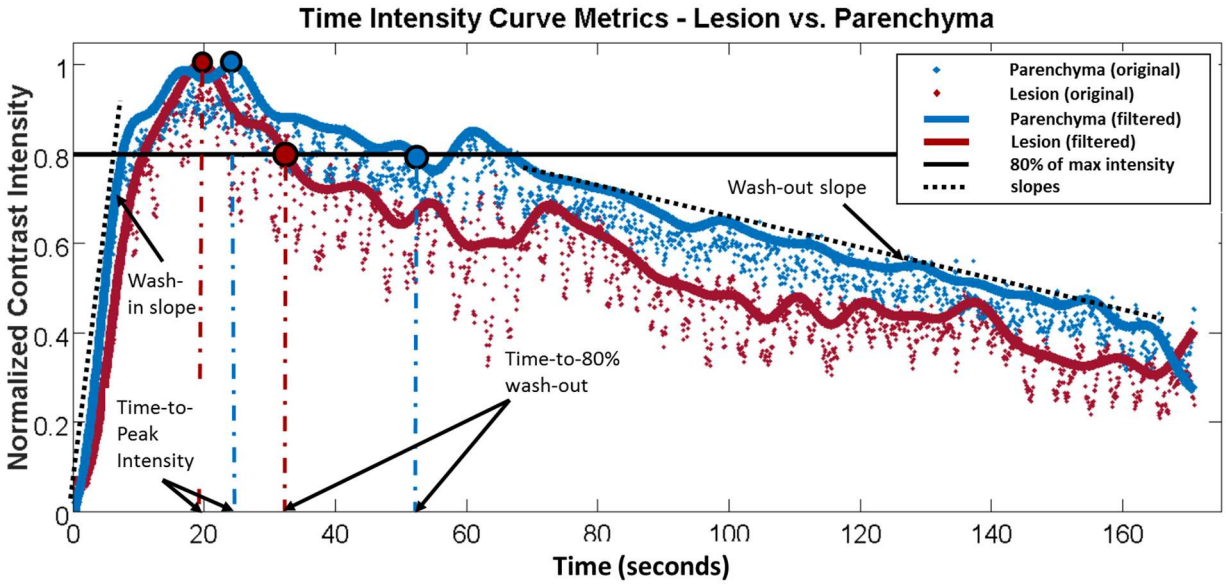


Figure A. 2. Sample TICs of a lesion (red) and renal cortex (blue). The raw data is filtered and smoothed through software filtering. Wash-in/wash-out slopes are calculated, and time-to-peak and time-to-80% wash-out are calculated based on the filtered curves.

### *A.2.iv Histological Analysis*

Histologic tissue diagnoses for resected (N=10) or biopsied (N=2) tissues were obtained through routine clinical reports at the University of North Carolina at Chapel Hill, Department of Surgical Pathology. Diagnosed lesion subtypes included chromophobe RCC, clear cell RCC, and papillary RCC.

### *A.2.v Statistical Analysis*

Statistical analyses were performed using MATLAB (MathWorks, Natick, MA, USA) and R-Studio (R Foundation for Statistical Computing, Vienna, Austria)[149]. For each metric, results were grouped by cancer type. One-way ANOVA was performed for each metric and the

Tukey-Kramer multiple-comparison test was used to determine significant differences between each group.

## A.3 Results

Twelve final CEUS clips qualified for TIC analysis based on image quality—clips with excessive out-of-plane motion or clips with inadequately visible parenchyma were excluded. The pathological findings for the twelve patients showed presence of 2 papillary RCC, 8 clear cell RCC, and 2 chromophobe RCC. Lesion sizes ranged from 1.72 cm to 7.50 cm in the longest dimension (3.75 cm ± 1.57 cm).

One-way ANOVA statistical test results for each metric are summarized in Table 2. Significant differences with a 95% confidence interval between groups were observed using the peak intensity ratio (Figure A.3) with $p=0.001$ ($p=0.001$ between clear cell and papillary RCCs, and $p=0.04$ between chromophobe and papillary RCCs) and time-to-80% ratio metric (Figure A.4) with $p=0.004$ ($p=0.020$ between chromophobe and clear cell RCCs, and $p=0.003$ between chromophobe and papillary RCCs). The PI metric measured the lowest lesion-to-parenchyma ratio for papillary RCC (0.57 ± 0.24), followed by chromophobe RCC (0.92 ± 0.03), and clear cell RCC (1.1 ± 0.1). The time-to-80% ratio metric also measured the lowest lesion-to-parenchyma ratio for papillary RCC (0.35 ± 0.33), followed by clear cell RCC (0.68 ± 0.16), and chromophobe (1.14 ± 0.05). All other metrics did not measure significant differences ($p>>0.05$) (Table 2).

Table A. 2. Results from ten metrics derived from lesion and parenchyma TICs

| **Metric** | **P-value (*p<0.05)** | **P-value (cc v p)** | **P-value (cc v ch)** | **P-value (p v ch)** |
|---|---|---|---|---|
| Peak Intensity ratio (PI) | 0.001* | 0.001 | 0.18 | 0.04 |
| Time to Peak (TPk) | 0.851 | --- | --- | --- |
| Time to Peak ratio (TPk-r) | 0.978 | --- | --- | --- |
| Time to 80% (T80%) | 0.065 | --- | --- | --- |
| Time to 80% ratio (T80%-r) | 0.004* | 0.08 | 0.02 | 0.003 |
| Wash-in Slope (WIS) | 0.957 | --- | --- | --- |
| Wash-out Slope (WOS) | 0.910 | --- | --- | --- |
| Wash-in Slope ratio (WIS-r) (lesion/parenchyma) | 0.890 | --- | --- | --- |
| Wash-out Slope ratio (WOS-r) (lesion/parenchyma) | 0.155 | --- | --- | --- |
| Wash-in/Wash-out Slope ratio (WIWOS-r) | 0.866 | --- | --- | --- |

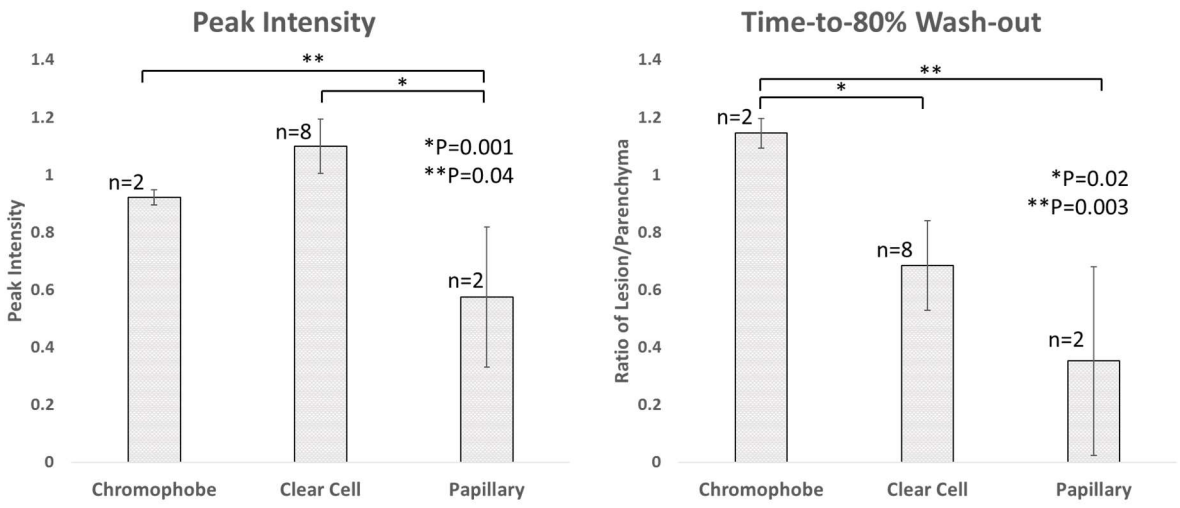


Figure A. 3. (left) Peak intensity ratio results. Papillary RCC measured 0.57 ± 0.24, chromophobe RCC measured 0.92 ± 0.03, and clear cell RCC measured 1.1 ± 0.1. The papillary RCC PI ratio was significantly different from clear cell (p=0.001) and chromophobe (p=0.04) ratios. (right) Time-to-80% ratio results. Papillary RCC measured 0.35 ± 0.33, chromophobe RCC measured 1.14 ± 0.05, and clear cell RCC measured 0.68 ± 0.16. The chromophobe RCC time-to-80% ratio was significantly different from clear cell (p=0.02) and chromophobe (p=0.003) ratios.

## A.4 Discussion

Previous studies have demonstrated the utility of qualitative and quantitative CEUS perfusion analysis (including TIC analysis) for distinguishing solid from cystic kidney masses and malignant from benign solid masses [145,146]. Solid masses, including most RCCs, and oncocytomas, typically appear hypoechoic on traditional b-mode ultrasound. Other solid lesions, such as angiomyolipomas typically appear hyperechoic due to their fatty content, but may sometimes also appear hypoechoic. CEUS has been shown to be a viable option in these cases where malignancy is unclear and contrast MR/CT are contraindicated. The focus of our study is to further discriminate between RCCs given the varying prognoses and treatments for each subtype. Pre-surgical knowledge of the suspected histological type of tumor would benefit

patients and health-care providers in making decisions about interventions, therapy, or clinical management approaches that incorporate careful observation. Several studies have recently emerged that quantify perfusion patterns of RCC subtype [140,143,145,146,150].

King et al. reported a similar TIC analysis and concluded that some metrics are better suited for certain types of kidney lesions [146]. For example, ccRCC enhances more than the surrounding parenchyma and has a faster time-to-peak (TPk), while pRCC enhances less than the parenchyma and has a slower TPk. chRCC was shown to have intermediate peak enhancement and TPk between ccRCC and pRCC. Metrics such as homogeneity of enhancement and rate of de-enhancement were shown to be more relevant to angiomyolipomas and oncocytomas [146].

Results for wash-in slope, wash-out slope, and TPk analyses have largely been inconsistent across previously published studies. This may be due to technical variations of the imaging and analysis technique and physiologic differences in the tumor. In all cases, lesion perfusion characteristics were compared to the renal cortex. Consistency in imaging depth has a significant impact on relative enhancement measurements between normal and diseased tissue due to attenuation. Also, heterogeneity of RCCs at different stages of development may induce user error by choosing a cross-section that is not entirely representative of the entire mass. It is also important to consider that many studies do not distinguish between histologies and are focused instead on the feature that distinguish benign from malignant disease. Some results report that all malignant RCCs display a fast wash-in, while others describe pRCC with a slower wash-in [143,145,146,150]. We observed that many TICs, especially for pRCC, exhibited a bi-phasic wash-out—a steeper initial wash-out of the contrast bolus injection, followed by more gradual clearance of the recirculating contrast. The gamma-variate fit is commonly used to model kidney perfusion, which is estimated by a left-skewed Gaussian curve with an

exponentially decaying tail [151]. The point of inflection on the downslope occurs approximately at 75% of the peak intensity, which happened to be near the beginning of the second phase of wash-out. Although our TICs did not conform to the gamma-variate fit as well as other studies have shown, we chose 80% to be our threshold to measure the start of the second phase of contrast wash-out. Cai and King used 60% and 50%, respectively, which we observed to be during the second phase of wash-out [145,146]. We believe that the bi-phasic wash-out pattern is of clinical importance, and measuring the time interval between phases may be a method of describing this pattern. Other perfusion models (e.g. Karshafian et al.'s lognormal perfusion model) that describe contrast replenishment during destruction-reperfusion imaging, can extrapolate information related to the distribution of flow speeds, vascular size and morphology, and blood volume. Burns et al. exquisitely describe the value of choosing an appropriate perfusion model for enabling versatile and reproducible measurements [152,153].

Interestingly, the two cases of pRCC we observed exhibited a statistically significantly fast decrease in contrast intensity compared to the surrounding renal cortex, opposite to what has been reported in other studies [145,146]. No significant differences were observed when measuring slopes for wash-in and the second phase of wash-out. While it is difficult to suggest why pRCC and chRCC display a steep and near constant wash-out, respectively, these may be clinically relevant perfusion patterns specific to pRCC and chRCC and should be further investigated. Peak-intensity results agreed with previous studies reporting that ccRCCs present as hyper-enhancing, while chRCC and pRCC, generally present iso or hypo-enhancing. ccRCC has been reported to be a faster growing, metastatic, and more vascular cancer relative to chRCC and pRCC, which supports the hypo-enhancing presentation of pRCC on CEUS [154–157].

Lu et al. recently published results from a large sample size study using a different quantitative approach to differentiate various RCCs. Their TIC analysis consisted of a temporal comparison between the lesion and renal parenchymal enhancement that included four distinct dynamic vascular patterns: unipolar positive (hyper-enhanced lesion through wash-in/wash-out), unipolar negative (hypo-enhanced lesion through wash-in/wash-out), bipolar positive (hyper-enhanced lesion through wash-in and hypo-enhanced through wash-out), and bipolar negative (hypo-enhanced lesion through wash-in and hyper-enhanced through wash-out). They concluded that unipolar and bipolar positive flow patterns were indicative of ccRCC and unipolar negative was indicative of pRCC and chRCC. While rates of wash-out were not included in their analysis, our lesion-to-cortex peak enhancement results agreed with these findings [140].

This study has several limitations. Our sample size was limited to only 12 patients. Out-of-plane breathing motion, obstruction of the lesion and parenchyma from rib and bowel shadowing, and lack of diagnostic pathology eliminated approximately half of the available data sets. For some patients, ideal transducer placement (i.e. wedging under the ribs) was sacrificed due to patient comfort, which is a significant limitation of CEUS for focal kidney imaging. We believe that standardized CEUS sonography training that describes how to handle the above limitations will significantly improve imaging quality.

A technical improvement made in this study was the use of a stereotactic clamp to hold the transducer for the 3-minute clip. This not only alleviated sonographer hand and wrist cramping, but maintained steady positioning throughout the clip. This was only feasible if the breathing motion was maintained within the imaging plane. For instances where out-of-plane movement persisted, manual placement by the sonographer was preferred to track the breathing motion. Occasionally, the patient body movement would displace the positioning of the clamp

and re-adjusting the position was difficult. While the stereotactic arm by itself may not add significant value to the quality of the ultrasound clips, we believe it can be used as an aid in positioning of the transducer for longer scans to alleviate sonographer discomfort.

Of the 12 lesions, there were only 2 pRCC and 2 chRCC, which greatly limited our statistical power. Given the small sample size, we were still encouraged by the trends observed with the time-to-80% metric and, especially, the peak enhancement ratio, which agreed with previous studies. There was only one angiomyolipoma and one oncocytoma, which were not included in the final results.

The TICs in this study were generated from a single cross-section through the kidney that captured both the lesion and normal parenchyma. For some patients, anatomic constraints made it difficult to orient the transducer directly in the center of the kidney parenchyma to visualize wash-in/wash-out in both the cortex and medulla. Kogan et al. reported differences in perfusion measurements between parasagittal and coronal planes due to varying amounts of cortical and medullary tissue in each plane [158]. While the ROI for the kidney parenchyma was placed over the cortex for image analysis on all of the images, the exact position of the ROI undoubtedly was inconsistent. The heterogeneity commonly associated with some RCCs is not adequately represented in a single cross-section perfusion analysis [159]. Three-dimensional destruction-reperfusion analysis offers holistic representation of kidney function. Feingold et al. reported standard deviations as high as 22% between individual cross-sections of the kidney and concluded that the accuracy and repeatability of overall kidney perfusion measurements significantly increase with 3-D imaging [160]. Unfortunately, 3-D destruction-reperfusion imaging requires a single-array transducer to scan stepwise elevationally and can only capture contrast wash-in. The advent of a two-dimensional array transducer capable of high-resolution,

real-time 3-D CEUS will allow the calculation of 3-D TICs, which will revolutionize kidney perfusion analysis and provide a more precise and accurate representation of the vascularity of diseased kidneys and solid kidney lesions. Based on our experience, we recommend a second contrast dose to acquire a wash-in/wash-out clip (after waiting the prescribed amount of time between doses) with the transducer centered sagittally over the kidney for more consistent perfusion measurements of the parenchyma.

Other limitations of this study are a result of the inherent variability in perfusion imaging. Cosgrove et al. describe factors of variability in perfusion imaging, including contrast type, circulation profiles of the contrast agent, infusion rate, breathing motion, attenuation, imaging settings, etc [161]. Overcoming these sources of variability is critical for the widespread clinical use of perfusion imaging. Despite these factors, CEUS has been shown to characterize kidney lesions with high sensitivities and negative predictive values (89-100% and 86-100%, respectively) [144].

## A.5 Conclusion

This study suggests that quantitative TIC analysis can be a feasible method for identifying subtypes of malignant solid renal masses. We explored different TIC characteristics that may be perfusion signatures for clear cell, papillary, and chromophobe RCC subtypes. Specifically, peak intensity and time-to-80% on wash-out metrics showed significant differences in perfusion patterns between the major RCC subtypes. The bi-phasic wash-out pattern may be a clinically important feature that should be further investigated. While very few studies have examined the utility of quantitative CEUS for RCC differentiation, there is general agreement

with several enhancement metrics. Further validation of these techniques, coupled with the ease and safety of CEUS, indicate that CEUS may be a powerful tool for improving diagnostic efficacy for RCC clinical management.

# APPENDIX B:

# Efficient DNA Fragmentation in a Bench-Top Ultrasonic Water Bath Enabled Through the Use of Cavitation Enhancing Microbubbles and Nanodroplets[3]

## B.1 Introduction

Next-generation sequencing is an attractive technology for detecting genetic disorders and characterizing the underlying molecular signature of disease to determine therapeutic options. It is not yet, however, a routine diagnostic tool due to a lack of standardization in DNA sample preparation, cost, and difficulties in data interpretation [162,163]. Specifically, random, unbiased fragmentation of DNA is a bottleneck in next-generation sequencing sample preparation pipelines due to serial processing of samples, cost limitations, poor DNA sample quality, and lack of reproducibility of fragment size between sample types [164,165].

Methods for fragmentation of DNA include enzymatic digestion, nebulization, hydrodynamic shearing, and sonication. Enzymatic digestion using DNase I, MNase, or restriction enzymes is very efficient, but introduces an enzyme bias. Regions of transcriptionally silent, tightly packed (heterochromatic) DNA and DNA with high G-C content can be refractive to enzymatic digestion and many enzymes only create nicks in the DNA instead of cutting completely though both strands [166–172]. The nebulization process shears solubilized DNA by forcing it through a pressurized nozzle (atomization). This method is fast, but requires large quantities of DNA and often results in a large distribution in the DNA fragment size and cross-

[3] This chapter previously appeared as an article in the Public Library of Science. The original citation is as follows: *Kasoji SK, Pattenden SG, Malc EP, et al. Cavitation Enhancing Nanodroplets Mediate Efficient DNA Fragmentation in a Bench Top Ultrasonic Water Bath. PLoS ONE. 2015.*

contamination between samples [173–175]. Hydrodynamic shearing involves forcing solubilized DNA through a mesh. It has the advantage of rapidly producing small DNA fragments of nearly uniform length. This method, however, is costly and the screen used for shearing is prone to clogging and cross-contamination between samples [176,177]. Finally, acoustic sonication uses ultrasound to mechanically shear DNA by cavitation. This method typically produces inconsistent results and is time consuming since DNA extracted from cells or tissue must be optimized each time to ensure that fragmentation occurs to the desired size range [164,178]. Also, similar to enzymatic digestion, heterochromatic DNA or DNA with high G-C content are very difficult to shear, which creates a bias toward better shearing efficiency in euchromatic and A-T rich regions [164,179–181]. Dedicated high-intensity focused sonicators such as a Covaris Adaptive Focused Acoustics™ instrument, or the lower-intensity Diagenode Bioruptor™ instrument, produce more consistent DNA fragmentation results than a single probe sonication device, however they can be financially inaccessible for many laboratories.

We investigated whether a biologically inert agent could be added to DNA samples to amplify cavitation in a sonication device and improve the consistency and speed of genomic DNA fragmentation. We initially tested lipid-encapsulated microbubbles, which are bubbles that are typically in the 1-10 micron (μm) diameter size range, and have been used in medical diagnostics as contrast agents for ultrasound imaging for approximately two decades [182]. The highly compressible core of a gas filled microbubble enables it to compress and expand in a pressure field in a process called inertial cavitation [183,184]. It has been shown through the use of high-speed photography that expansion and compression wall velocity of microbubbles in an acoustic field can be on the order of 700 meters per second even at only moderate acoustic pressures (1.2 MPa, 2.4 MHz) [185]. At even higher acoustic pressures, which are typical of a

commercial sonicator, microbubble cavitation is very unstable and results in a violent collapse, locally releasing a great amount of mechanical energy.

As an alternative to microbubbles, we designed a novel formulation of phase-change nanodroplets [186,187]. These phase-change nanodroplets are composed of a volatile, liquid perfluorocarbon core stabilized with a phospholipid monolayer shell with a diameter on the order of 200-400 nm [188]. These excipients are biologically inactive when combined with genomic DNA samples. When subject to sufficient acoustic energy and temperature, the nanodroplets vaporize into microbubbles that have approximate diameters of 1-5 μm. The phase-change nanodroplets are more stable than microbubbles and require energy to first vaporize and then to cavitate, therefore prolonging the cavitation enhancing effect longer than that of bubbles under certain conditions. The increased stability of nanodroplets compared to microbubbles has been demonstrated by Sheeran et. al. in an in vivo animal model circulation time study [189]. We show that nanodroplets perform as an effective cavitation enhancement agent for the fragmentation of gDNA, decreasing sonication time while preserving DNA fragment size distribution and yield.

## B.2 Methods

### *B.2.i Genomic DNA preparation*

Genomic DNA was prepared from a 10 mL saturated culture of the Saccharomyces cerevisiae wild type haploid strain, BY4741 (MATa his3Δ1 leu2Δ0 met15Δ0 ura3Δ0). Genomic DNA was purified using the MasterPure™ Yeast DNA Purification Kit (epicenter #MPY80200), according to manufacturer instructions. Quantitation of purified DNA was performed on a Qubit® 2.0 Fluorometer.

### *B.2.ii Microbubble and Nanodroplet Preparation*

Microbubbles consisting of a gas core and an encapsulating lipid monolayer were generated by mechanical agitation of a lipid solution in the presence of decafluorobutane (DFB). The lipid solution composed of 1,2-distearoyl-sn-glycero-3-phosphocholine (DSPC) (Avanti Polar Lipids, Alabaster, AL, USA) stabilized by 1,2-distearoyl-sn-glycero-3-phosphoethanolamine-N-methoxy (polyethylene-glycol)-2000 (DSPE-PEG2000) (Avanti Polar Lipids, Alabaster, AL, USA) in a 9 to 1 molar ratio. The lipid solution was then emulsified in a phosphate-buffered saline solution containing propylene glycol (15% v/v) and glycerol (5% v/v) with a final lipid concentration of 1.0 mg/mL. 1.5 mL aliquots of the lipid emulsion were dispensed into 3 mL vials and sealed with a rubber cap. The air-filled headspace in the vial was exchanged with DFB (C4F10, boiling point: -2°C) gas (Fluoromed, Round Rock, TX, USA). The vial was vigorously shaken for 45 seconds using a high-speed mixer (Vialmix, Bristol-Myers Squibb Medical Imaging, North Billerica, MA, USA) to form the microbubble solution. The solution contained approximately 1010 bubbles/mL with a diameter of 1.07 ± 0.9 μm,

measured with an Accusizer 780 (Particle Sizing Systems, Santa Barbara, CA, USA).

Nanodroplets were formed by cooling and compressing the microbubble solution to induce a gas-to-liquid phase transition of the DFB gas. Dry ice was used to cool approximately 100 mL of N-propanol to -9° C in a beaker. A 20-gauge needle connected to a fully-drawn 60 mL syringe was inserted into the DFB-headspace through the rubber cap of the vial. The vial was then submerged into the 2-propanol and swirled while simultaneously increasing the pressure inside of the vial by depressing the syringe plunger, eventually condensing the bubbles into droplets. The nanodroplet solution was stored at -20° C when not in use. 20 µL of nanodroplets were dispensed in each DNA sample for sonication.

### *B.2.iii DNA Fragmentation: Covaris E110 Sonicator*

Five µg of BY4741 gDNA was added in duplicate to either Covaris microTUBEs (#520045), or borosilicate glass vials in a final volume of 100 µL in TE (10 mM Tris-HCl, pH 8.0, 1 mM EDTA). Ten µL of nanodroplets was added to the borosilicate glass vials. Sample tubes were submerged up to the cap in a water bath and sonicated for 2 minutes each at 20% duty cycle, Intensity 8, and 200 cycles per burst. After fragmentation, 20 µL of DNA was combined with 10X loading buffer (50% glycerol with Orange G and SYBR green) and loaded onto a 1.5% agarose gel and subjected to gel electrophoresis. For high throughput sequencing preparation, each sample was concentrated in a Zymo Research ChIP DNA Clean & Concentrator column (#D5201), followed by quantitation on a Qubit® 2.0 Fluorometer. DNA fragment quality and size was assessed using an Agilent D1000 ScreenTape system.

### *B.2.iv DNA Fragmentation: Branson Sonifier Bath*

Five µg BY4741 gDNA was added in quadruplet to 0.2 mL PCR strip tubes (Genesee Scientific #27-104) in a 150 µL volume in TE (10 mM Tris-HCl, pH 8.0, 1 mM EDTA). Ten µL of microbubbles or nanodroplets were added to each of two of the samples. The samples were placed in a linear acrylic tube holder (0.5" spacing) and positioned in the center of the ultrasonic bath such that the sample tubes were submerged up to the cap in water. The water bath was either cooled to 3-4° C using a circulating refrigerated bath chiller followed by sonication for 5 minutes, or chilled ice water was added just prior to sonication. Following fragmentation, 20 µL of DNA was combined with 10X loading buffer (50% glycerol with Orange G and SYBR green) and loaded onto a 1.5% agarose gel and subjected to gel electrophoresis. Densitometry was performed using Image J software. For high throughput sequencing preparation, each sample was concentrated in a Zymo Research ChIP DNA Clean & Concentrator column (#D5201), followed by quantitation on a Qubit® 2.0 Fluorometer. DNA fragment quality and size was assessed using an Agilent D1000 ScreenTape system.

### *B.2.v Next-generation Sequencing*

Yeast gDNA samples sonicated in the Covaris E110 were prepared using Kapa DNA Library Prep Kit for Illumina (#8234). Libraries were prepared using both agarose gel size selection (Sage Science Pippin Prep Targeted DNA Size Selection System) and magnetic bead selection (Magbio HighPrep™ PCR beads (#AC-60500), with 0.45 and 0.2 ratios for the first and second step of size selection, respectively) to ensure that the size selection method did not influence sequencing result comparison.

Yeast gDNA samples fragmented in the ultrasonic bath were prepared using the Illumina TruSeq Nano DNA LT Sample Preparation Kit (#FC-121-4001). Each sample was prepared with either 200 ng or 100 ng of DNA and size-selected using magnetic beads as described.

Following preparation, all libraries were quantified using a Qubit® 2.0 Fluorometer. DNA fragment quality and size was assessed using Bio-Rad Experion™ Automated Electrophoresis System. Sequencing data have been deposited to the BioProject database (National Center for Biotechnology Information), BioProject accession PRJNA284931.

## B.3 Results and Discussion

### *B.3.i Nanodroplets are a shelf-stable agent that perform better than microbubbles for DNA fragmentation*

Microbubbles were initially evaluated as a cavitation enhancement agent in the Covaris E110 sonicator. We observed a significant increase in fragmentation of DNA within 300-500 bp (as illustrated by the % band density of the gels outside the desired bp range, Figure B.1) Microbubbles, however, are rapidly fragmented in a high amplitude acoustic field (half-life in the order of seconds) so their effective cavitation enhancement was only 5-10 seconds with the given acoustic parameters. We hypothesized that by condensing microbubbles to form nanodroplets, we could control the release of microbubbles therefore sustaining the cavitation enhancement.

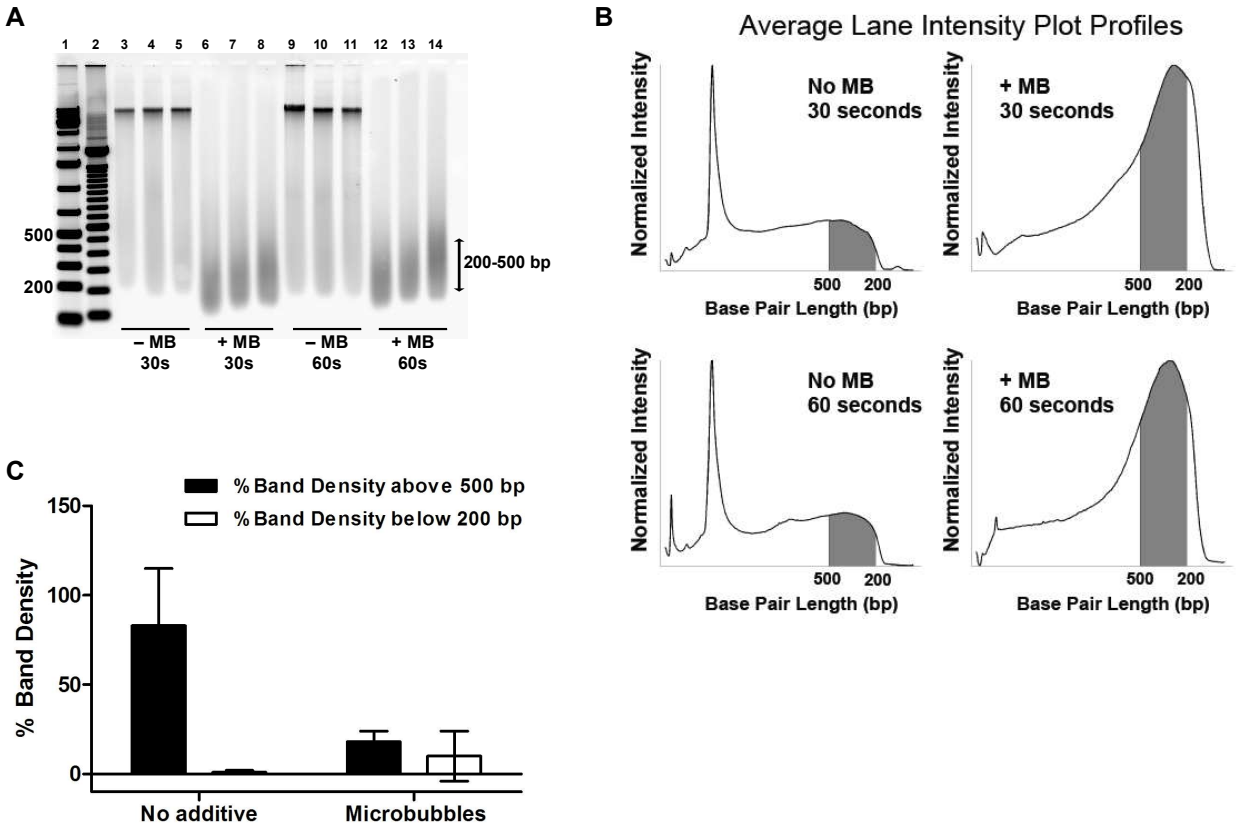


Figure B. 1. Analysis of the fragmented DNA products following focused-wave sonication of purified genomic DNA. Gel electrophoresis (A) demonstrated DNA fragments in the desired 200-500 base pair (bp) range after 30 (lanes 6-8) and 60 seconds (lanes 12-14) of sonication in the presence of microbubbles (microbubble). In contrast, few fragments of this size were recovered in the absence of microbubbles out to 1 minute (lanes 3-5 and 9-11). The normalized average intensity plot profiles for each test condition (B) were graphed as a function of bp length, with the desired range shaded gray. (C) Densitometry analysis indicates that DNA fragmentation is centered in the 200-500 bp range for samples sonicated in the presence of lipid-encapsulated microbubbles. Error bars represent the standard deviation for 3 biological replicates with 3 technical replicates each.

Microbubbles were produced through vigorous mechanical agitation of a lipid solution inside a 3 mL vial, followed by simultaneously cooling and increasing ambient pressure of the microbubble solution to condense the bubbles into nanodroplets (Figure B.2A). A persistence study was performed to test the half-life of microbubbles versus nanodroplets using the

ultrasonic bath, showing that nanodroplets persist much longer with acoustic parameters kept constant (Figure B.2B). In addition, we demonstrated that nanodroplets have excellent shelf stability; they can be stored at -20°C with no loss of performance following multiple freeze-thaw cycles (Figure B.3A).

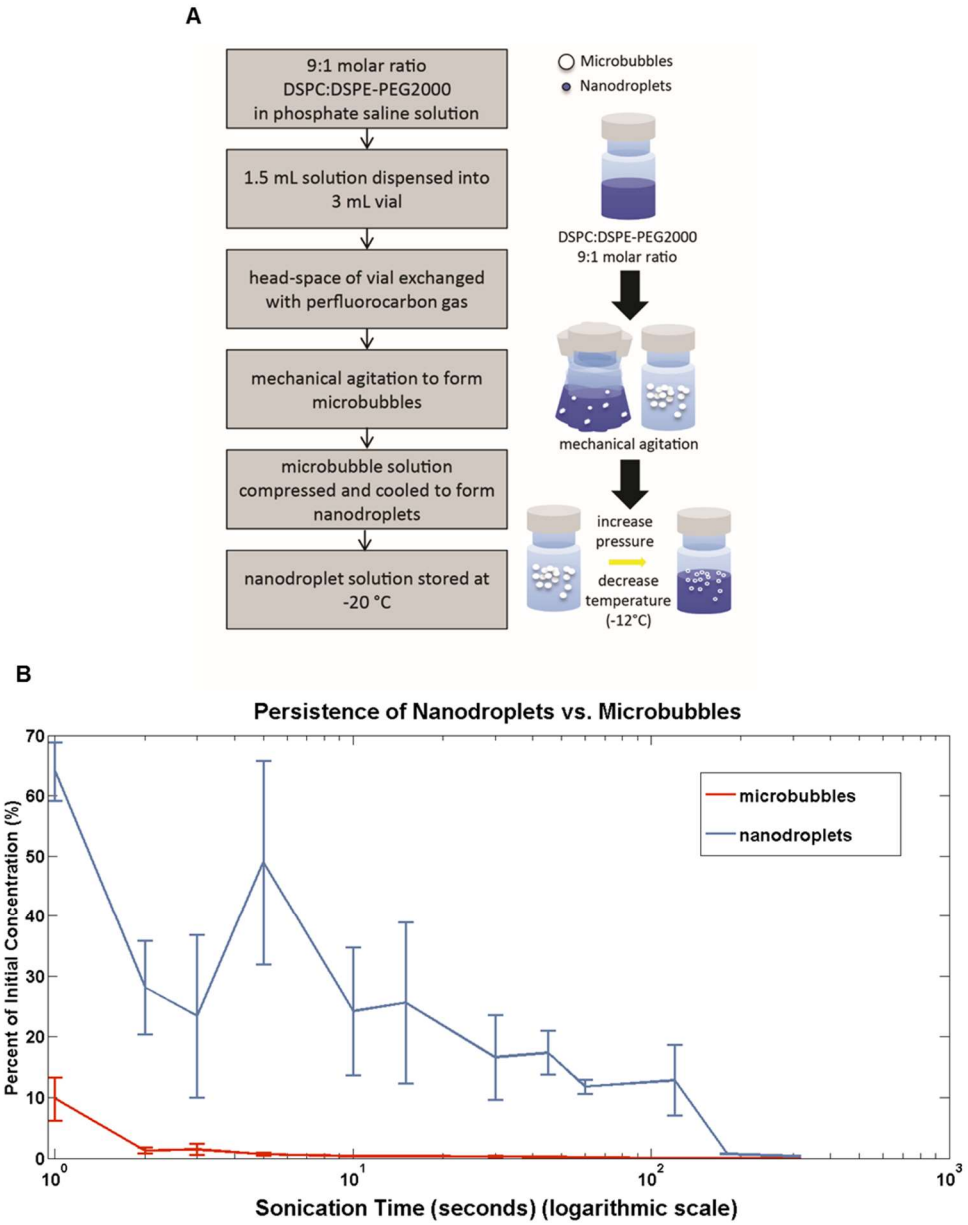


Figure B. 2. Nanodroplets persisted in solution longer than microbubbles. A) Flow chart outlining method for production of nanodroplets. B) A persistence study was performed in the ultrasonic bath to compare nanodroplets and microbubbles. An Accusizer particle sizing system (Particle Sizing Systems, Port Richey, FL) was used to measure the microbubble and nanodroplet concentrations at specific time points between 0 and 300 seconds (5 minutes). Nanodroplets maintained between 10–20% of their initial concentration as far out as 3 minutes into the sonication treatment, while the microbubble concentration dropped to 10% after 1 second.

### *B.3.ii DNA fragmented in the presence of nanodroplets is consistent with DNA fragmented by a commercially available method*

DNA fragmentation was initially compared with or without nanodroplets in the commercially available Covaris E110 sonicator. Borosilicate glass vials produced a smaller average fragment size within a given sonication time compared to plastic PCR tubes, so all further experiments in this instrument were performed in the borosilicate glass Covaris microTUBE (Figure B.3B, compare lanes 1-3 to lanes 4-6). The Covaris microTUBE contains a hydrophobic polymer rod with small pores that enucleate gas bubbles when exposed to acoustic energy [190]. Comparisons were made between duplicate samples of the microTUBE with the rod, and the microTUBE with nanodroplets (Figure B.4A). Genomic DNA purified from the Saccharomyces cerevisiae strain, BY4741, was used for this study as the small genome size allowed for high density sequencing coverage.

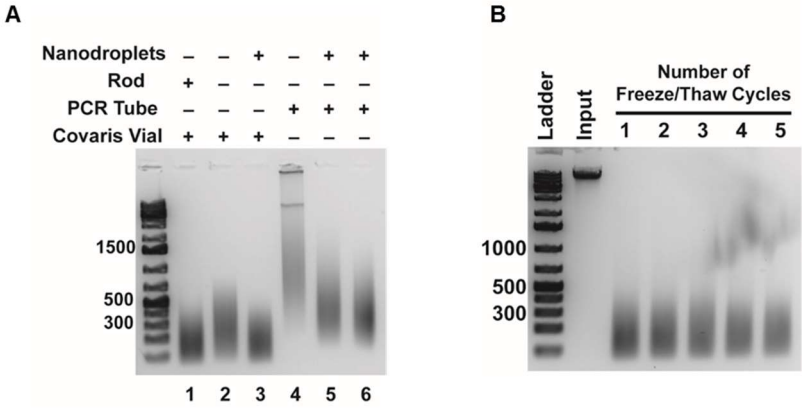


Figure B. 3. Nanodroplets are an effective cavitation agent for use in DNA fragmentation. A) The effectiveness of nanodroplets as a cavitation enhancement agent after multiple freeze-thaw cycles was tested. DNA ladder size is indicated in base pairs. Input is DNA prior to sonication with nanodroplets. B) Comparison of DNA fragmentation efficiency after two minutes in glass (Lanes 1-3) versus plastic (Lanes 4-6) tubes in the Covaris E110 sonicator. The addition of nanodroplets to Covaris microTUBES produces a DNA fragment size distribution comparable to the microTUBES with a rod (compare Lanes 1 and 3). DNA fragmented in glass microTUBES had a smaller DNA size distribution compared to plastic 0.2 mL PCR tubes (compare Lanes 3 and 5-6). DNA ladder size is indicated in base pairs.

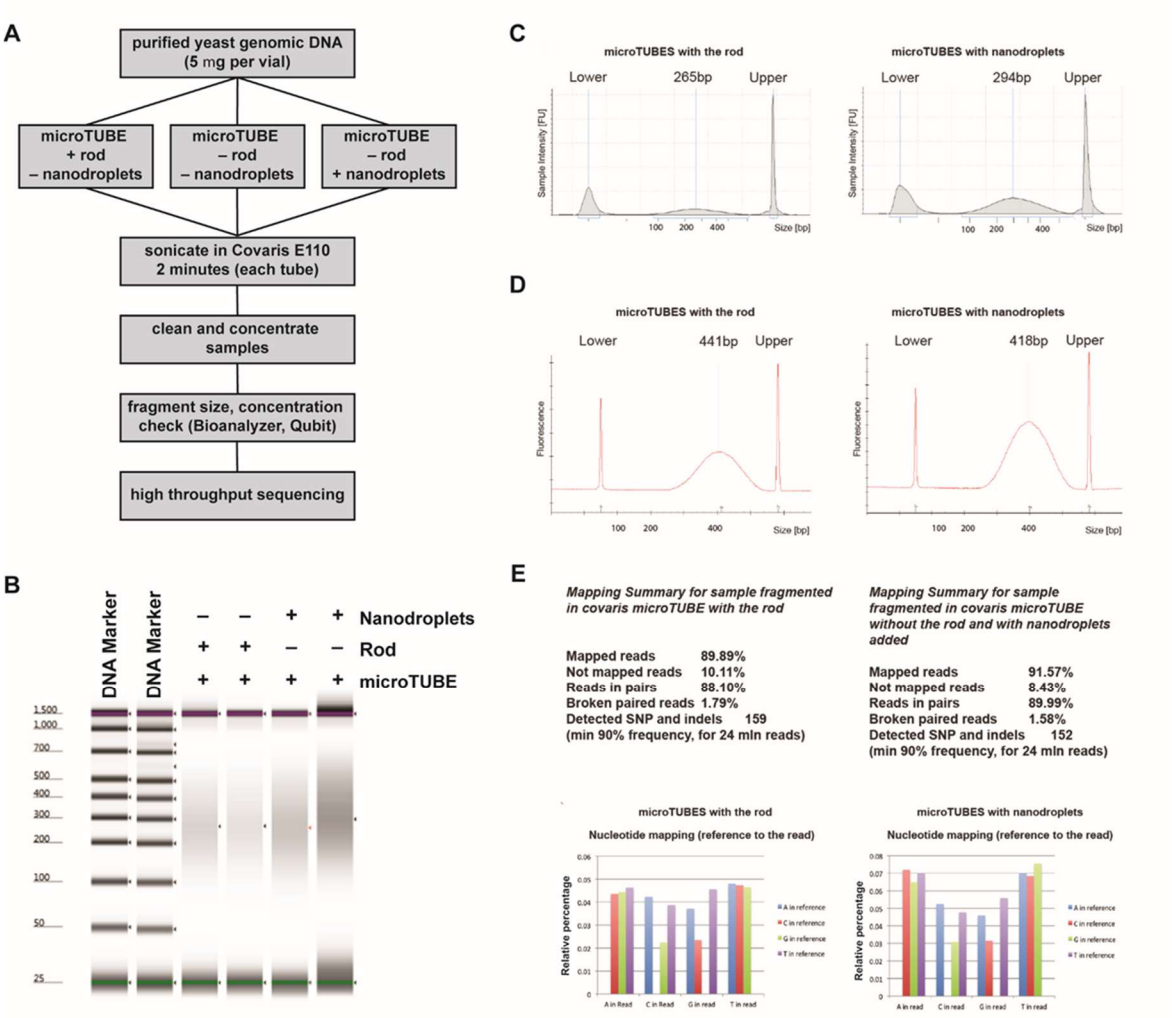


Figure B. 4. Saccharomyces cerevisiae genomic DNA (BY4741) fragmented with nanodroplets in a commercial sonicator is comparable in quality to DNA fragmented using a commercial method. A) Flow chart outlining method for comparing DNA fragmentation methods. B-C) DNA fragment size distribution was determined on an Agilent D1000 ScreenTape system. B) False gel picture showing DNA fragment size distribution in base pairs for samples fragmented in the Covaris E110 sonicator. Purple bars indicate the upper (1,500 bp) molecular weight marker and green bars indicate the lower (25 bp) molecular weight marker in each lane. C) Traces for DNA samples in microTUBES with the rod (left panel) or microTUBES with nanodroplets (right panel) that were subjected to sequencing. Average size is indicated in base pairs (bp). DNA size markers are denoted by Upper and Lower. D) Traces showing similar size distribution of DNA after sequencing library preparation. Average size is indicated in base pairs (bp). DNA size markers are denoted by Upper and Lower. E) Mapping sequencing reads to the Saccharomyces cerevisiae (S288c) reference genome is comparable in detection of single nucleotide variations and indels. Abundance and profile of relative errors in sequencing reads does not indicate a difference in the presence of error bias in the data.

Following two minutes of sonication, the average DNA fragment size was comparable between the microTUBE and nanodroplet samples (Figure B.4B, Figure B.4C). To confirm that the DNA fragmented in the presence of nanodroplets was suitable for downstream applications, we subjected these samples to next-generation sequencing. Following library preparation, no difference in quality and profile was noted between the two samples (Figure B.4D) or between duplicate samples. Both average fragment size and the fragment distribution profiles were similar and depended on the chosen size selection method and not sonication method (Table D.2).

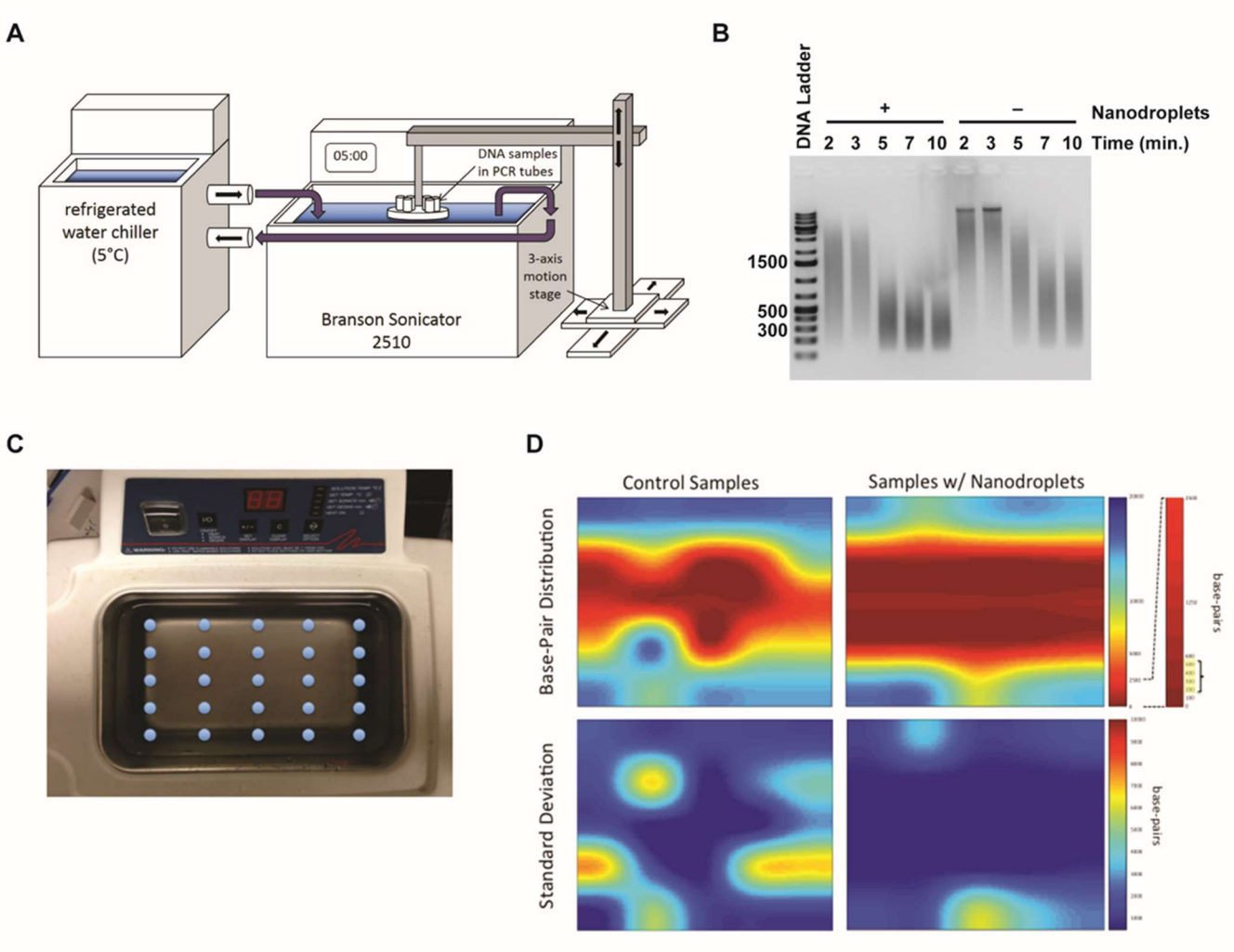


Figure B. 5. The addition of nanodroplets allows genomic DNA fragmenation in an ultrasonic water bath. A) Schematic showing the ultrasonic bath used for sonication. Samples are immobilized in the water bath using a stand with a tube rack attached. The circulating water chiller is optional. Water chilled to four degrees Centigrade can be added just prior to sonication, with no loss in DNA fragmentation efficiency. B) A time-titration was performed with samples with and without nanodroplets. Following fragmentation, samples were run on a 1.5% agarose gel and visualized using SYBR green. DNA ladder sizes are indicated in base pairs. C) Arrangement of DNA samples fragmented in the ultrasonic bath with and without samples to produce D) an acoustic field map of the bath. The fragmentation ability (base pair size) is visualized with the color bar, where red indicates complete fragmentation in the 200-500 bp range.

Sequencing reads were mapped to the Saccharomyces cerevisiae S288C reference genome, from which the BY4741 strain used in this study was derived [191]. Samples fragmented in the presence of nanodroplets showed no appreciable difference in mapped reads,

detection of single nucleotide variations and insertions and deletions (indels), or error bias in the data (Figure B.4E) compared to samples fragmented in the microTUBEs. Thus, genomic DNA fragmented in the presence of nanodroplets is consistent with a commercially available method.

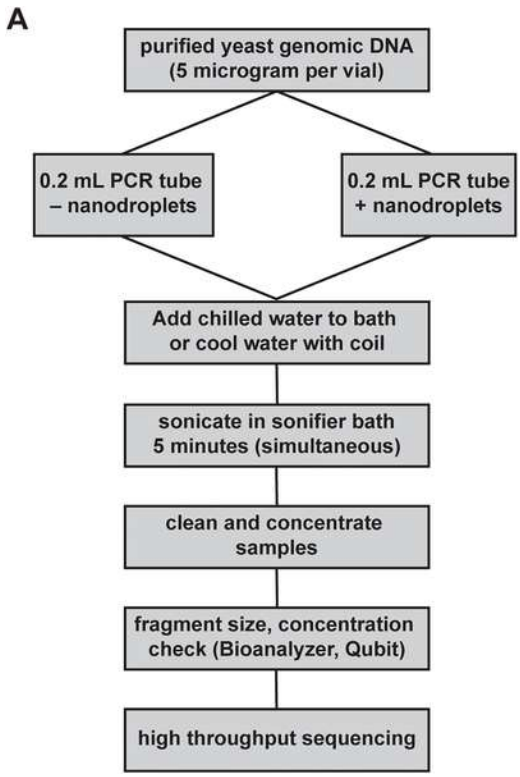


Figure B. 6. DNA fragmentation in an ultrasonic water batch compared to a commercially available device. A) Flow chart outlining method for comparing DNA fragmentation methods.

### *B.3.iii The addition of nanodroplets permits DNA fragmentation in a bench top ultrasonic water bath*

Most commercially available sonication devices are low thoughput, sonicating only a single sample at a time. Since gDNA fragmentation with nanodroplets was effective in a commercially available sonicator, we tested the performance of nanodroplets in a standard laboratory ultrasonic water bath with the aim of increasing sample throughput, and negating the

need for specialized equipment.

A Branson 2510 Ultrasonic Cleaning Bath was converted to a gDNA sonicator by installing a simple custom tube holder to submerge sample vessels at desired positions in the bath. To maintain the temperature conditions of current DNA fragmentation methods, water was pre-chilled to 4° C and added to the ultrasonic bath. Chilled water could also be circulated using a refrigerated water chiller (Figure B.5A). The operating level of the ultrasonic bath was demarcated by the manufacturer at double the operating wavelength of the acoustic field in water at room temperature (25°C). To maintain constant acoustic parameters, we adjusted the water level according to the wavelength change of the acoustic field in water at 5°C. Sonication time was optimized to five minutes in thin walled PCR tubes (Figure B.5B). These tubes were selected because the thin wall was less likely to interfere with the acoustic field, and they are inexpensive and readily available from a number of commercial vendors. An acoustic field map achieved by sonicating a five-by-five array of DNA samples (Figure B.5C) determined that the most consistent gDNA fragmentation occurred in the central region of the bath (Figure 5D), so samples were immobilized within this area using a custom sample holder. The holder for these studies consisted of a single row of 14 samples with 0.5 inch spacing. In future studies, spacing will be further optimized to maximize the number of samples that can be fragmented at once.

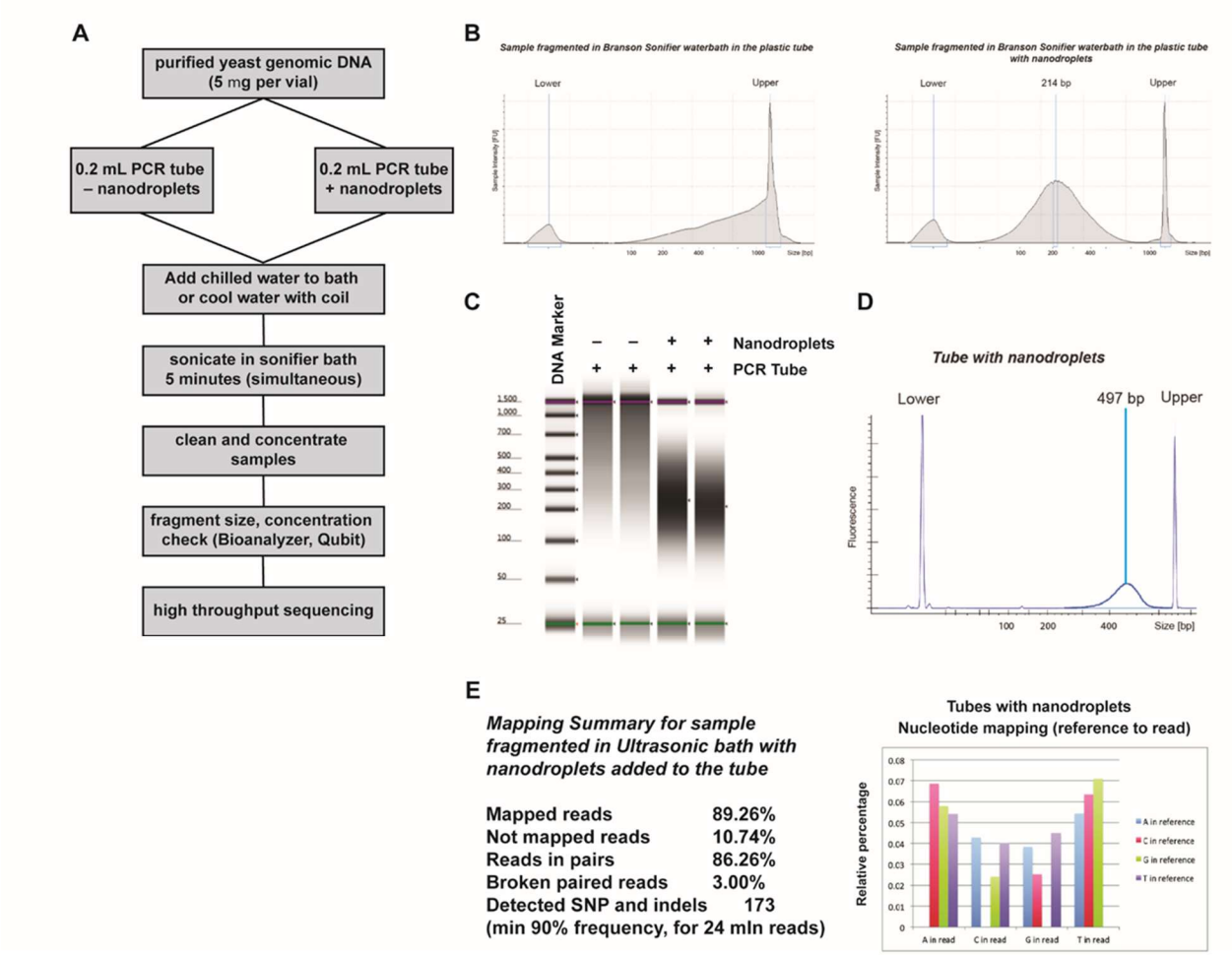


Figure B. 7. Saccharomyces cerevisiae genomic DNA (BY4741) fragmented with nanodroplets in an ultrasonic water bath is comparable in quality to DNA fragmented in a commercially available device. (A) Agilent D1000 ScreenTape data showing size distribution of DNA fragmented in tubes without (left panel) or tubes with nanodroplets (right panel). Average size is indicated in base pairs (bp). DNA size markers are denoted by Upper and Lower. (B) False gel picture indicating that DNA fragmented without nanodroplets had an average fragment size >1,500 bp. Purple bars indicate the upper (1,500 bp) molecular weight marker and green bars indicate the lower (25 bp) molecular weight marker in each lane. (C) Size distribution of DNA after sequencing library preparation. Average size is shown in base pairs (bp). DNA size markers are denoted by Upper and Lower. (D) Mapping sequencing reads to the Saccharomyces cerevisiae (S288c) reference genome is comparable in detection of single nucleotide variations and indels in Figure B.4E. Abundance and profile of relative errors in sequencing reads does not indicate a difference in the presence of error bias in the data compared to data in Figure B.4E.

To confirm that the DNA fragmented in the ultrasonic water bath could be used for next-generation sequencing, fragmentation of BY4741 yeast gDNA was performed in duplicate in the presence and absence of nanodroplets (Figure B.6). In the absence of nanodroplets, the average DNA fragment size was >1,500 bp, a size not suitable for library preparation (Figure B.7A, B.7B, Table D.2). Samples with nanodroplets had an average fragment size of <250 bp before library preparation (Figure B.7A, B.7B), and an average size of 500 bp after library preparation (Figure B.7D, Table D.2), which was comparable to data obtained from fragmentation in the Covaris (Figure B.4C, B.4D, Table D.2). After sequencing, the duplicate samples fragmented in the presence of nanodroplets showed no appreciable difference in mapped reads, detection of single nucleotide variations and indels, or error bias in the data (Figure B.7E). Therefore, cavitation enhancement by nanodroplets in a standard laboratory ultrasonic water bath produced fragmented gDNA that was comparable to DNA obtained from sonication in a commercially available device.

The sonication methods that are employed by the Covaris and the ultrasonic water bath are different with respects to the acoustic frequency used and the distribution of the acoustic field. The Covaris uses a spherically focused 1 MHz ultrasound transducer which produces a very tight (~2 mm) focus. The ultrasonic water tank uses two heavy-duty 40 kHz sandwich type transducers that produce a broad acoustic field within the tank, which is amplified by standing waves created by reflections from the water-air interface and the sides of the tank. DNA can be fragmented using both systems, through the combination of cavitation mechanisms and high microscopic fluid flow (Figure C.4). The overall intensity of the acoustic field in the ultrasonic water tank is less than the acoustic intensity at the focal spot of the Covaris transducer, however the probability threshold for cavitation events increases with decreasing frequency

[187]. Furthermore, the addition of the nanodroplets further enhances the cavitation effect. The ultrasonic tank possesses the advantage of increasing the number of cavitation events and having a larger effective acoustic field area allowing greater number of samples to be treated simultaneously (Figure B.5D).

## B.4 Conclusion

We have demonstrated that fragmentation of gDNA in the presence of nanodroplets does not require specialized equipment, can be performed for multiple (up to 14) samples simultaneously in five minutes, and produces high quality, fragmented DNA for next-generation sequencing. Phase change nanodroplets are produced using a simple method and can be stored at -20°C for extended periods of time, withstanding multiple freeze-thaw cycles. The use of this cavitation enhancement agent in combination with a standard laboratory ultrasonic bath is a useful and cost-effective method for academic institutions and research laboratories that do not have access to specialized sonication devices, and provides new accessibility and improved efficiency for a crucial step in next-generation sequencing.

# APPENDIX C:

## Supplementary Figures

Figure C. 1

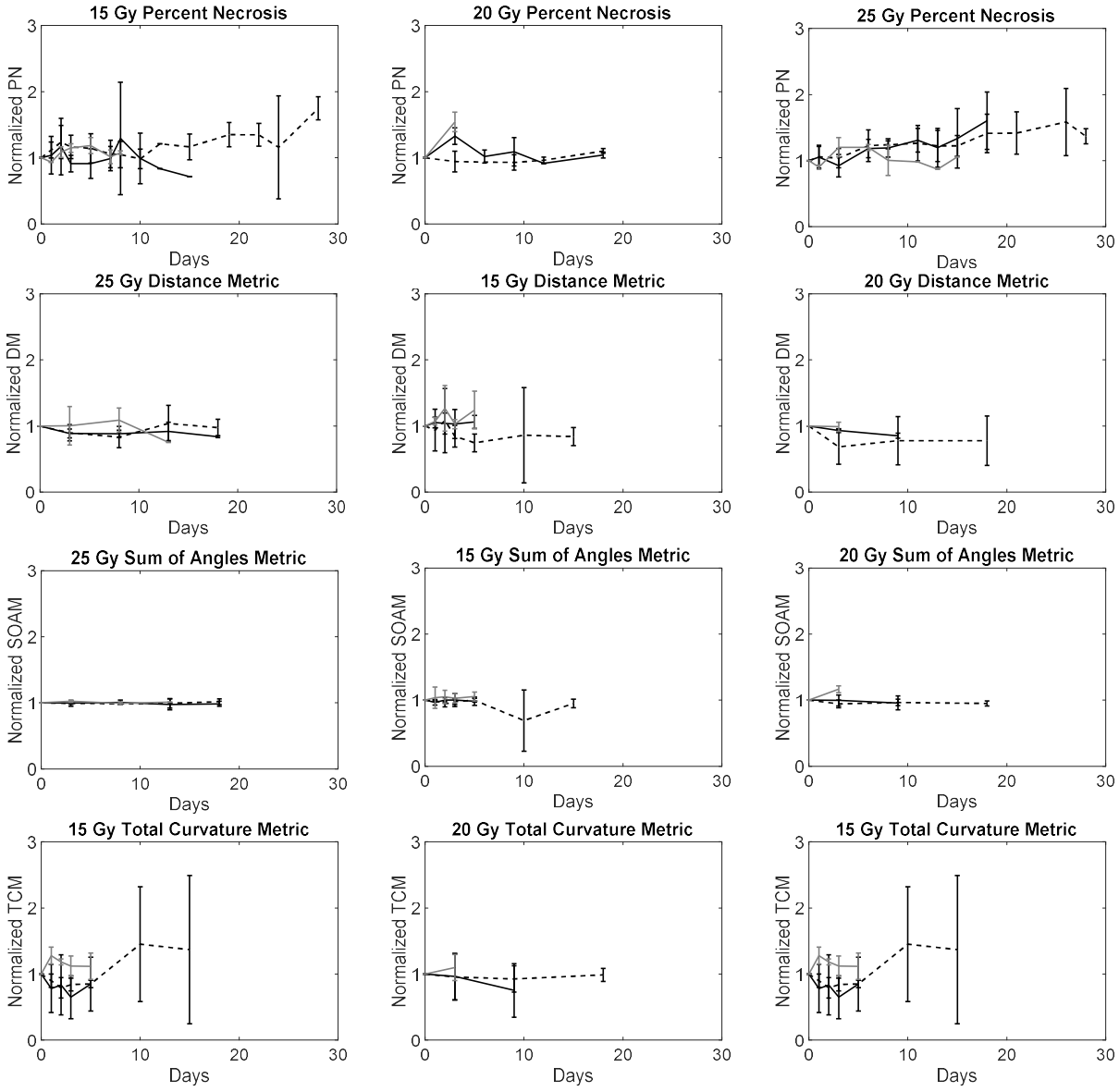


Figure C. 1. Growth curves of PN and vessel tortuosity metrics (SOAM, DM, and TCM). No statistically significant differences in any metrics were observed. Increased PN is observed in partial responders, however the mean values for untreated controls and complete responders are inconsistent.

Figure C. 2

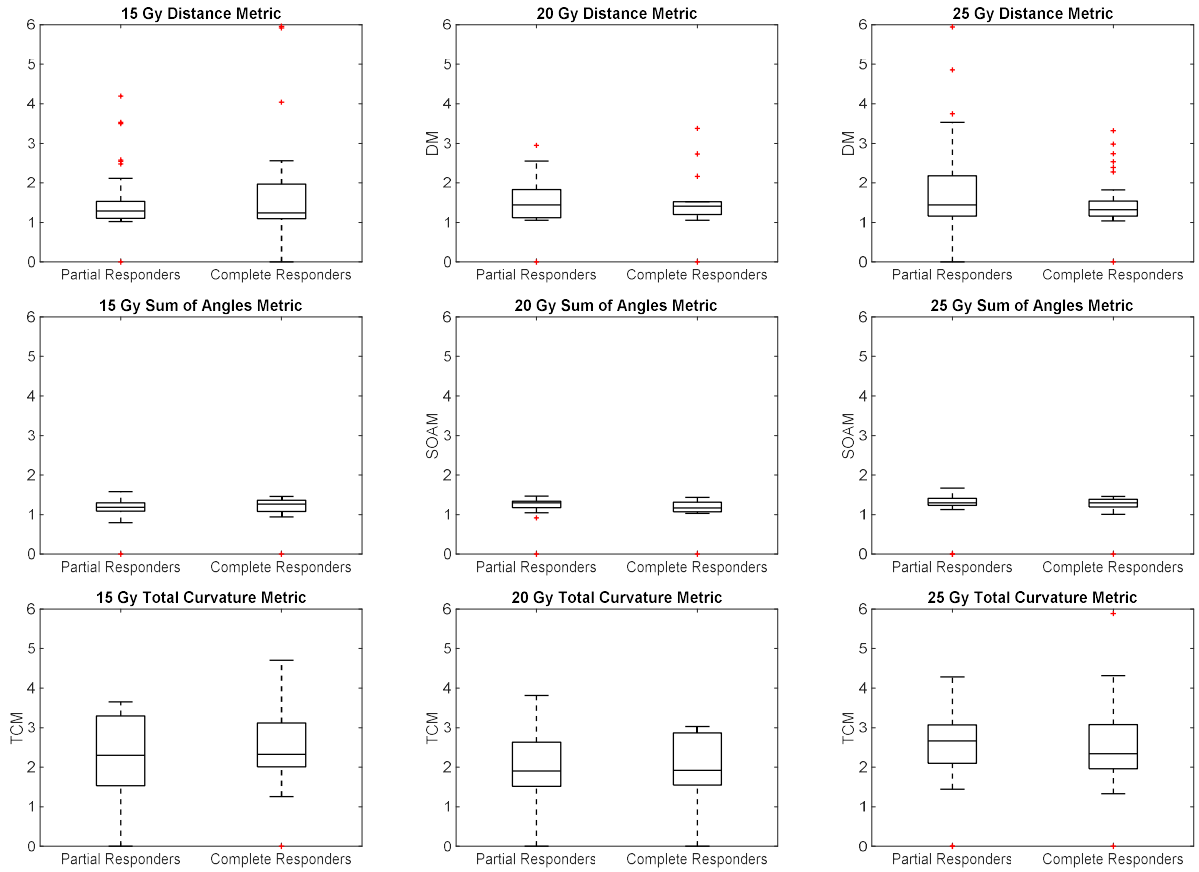


Figure C. 2. Differences in SOAM, DM, and TCM between partial responders and complete responders at the final measurement time point when we clearly observe statistical differences between the two groups using TV. No statistical differences were found between response groups.

Figure C. 3

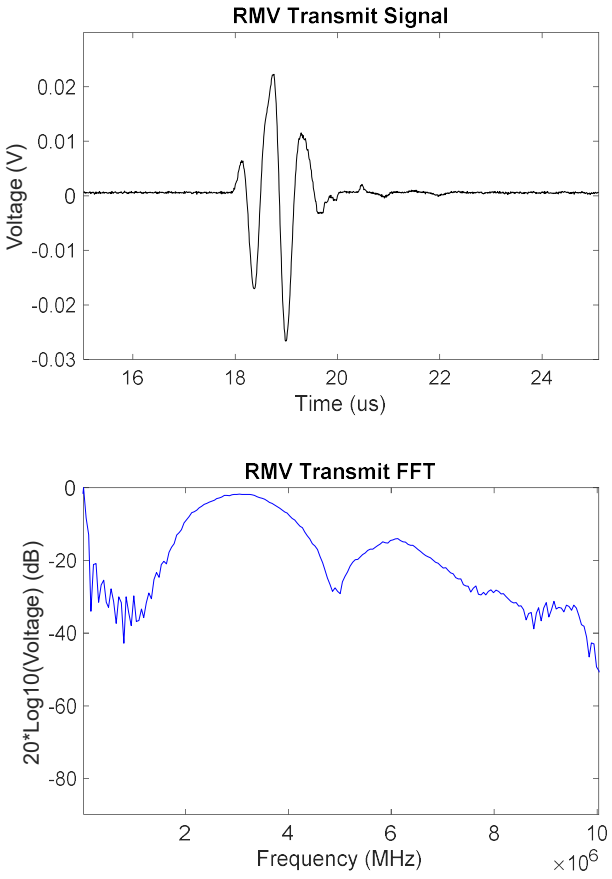


Figure C. 3. Transmit waveform centered at 3.5 MHz. and frequency spectrum of the RMV probe, as a comparison to the DF-TRUS and DP-DF transducers. The pulse length is considerably shorter than the DF-TRUS probe.

Figure C. 4

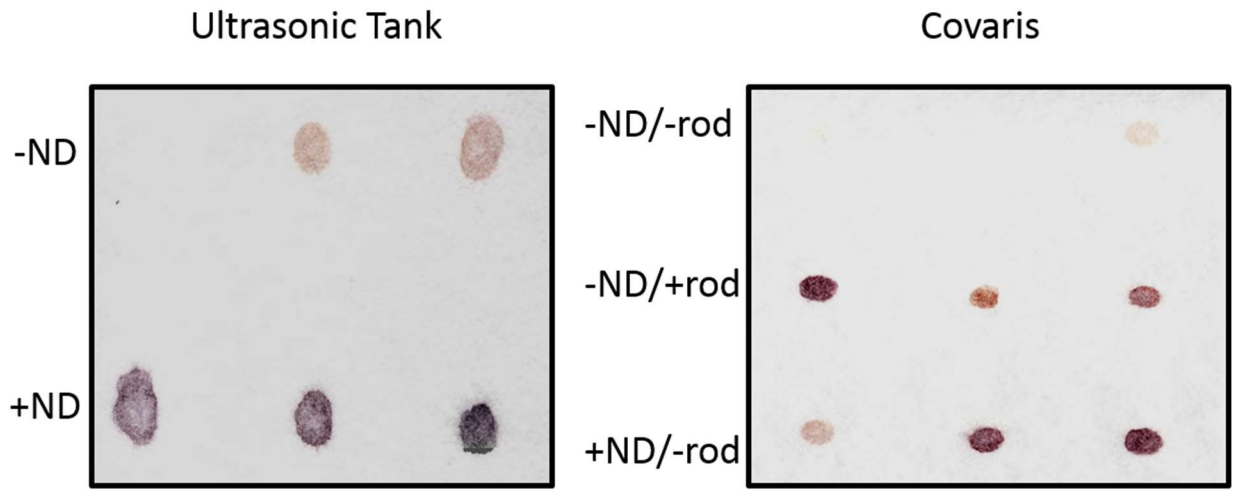


Figure C. 4. The starch-iodine test was performed to confirm the presence of cavitation. If cavitation is present, the Starch-KI solution turns from clear to blue. Reactive oxygen species that form during a violent cavitation event transform dissolved iodide ions into iodine. Iodine then conforms to the starch molecule and results in a visible blue color. The results from the Covaris and the ultrasonic bath are displayed in a dot blot array. In both the Covaris and the ultrasonic bath, vials with no rod or nanodroplets showed minimal fragmentation.

Figure C. 5

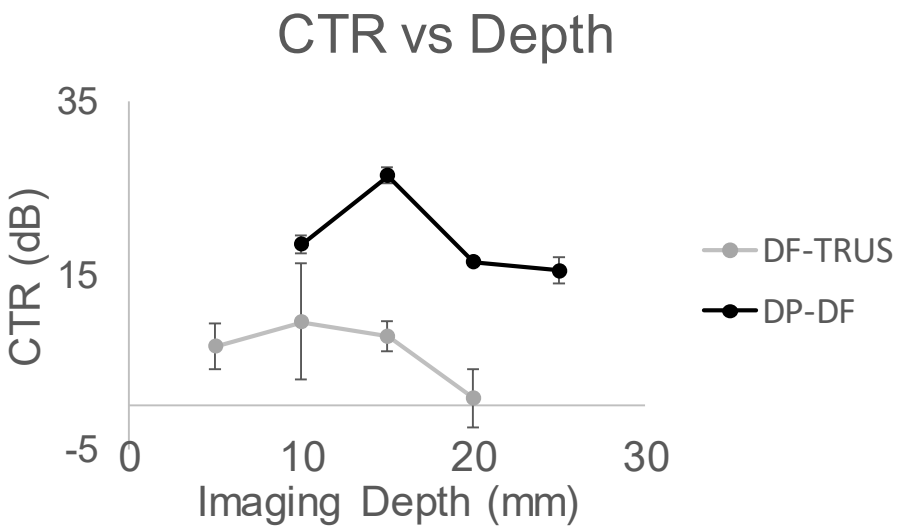


Figure C. 5. CTR vs. Imaging Depth in an attenuating phantom of the DF-TRUS and DP-DF transducers. The CTR drastically decreases past 10 mm for the DF-TRUS probe.

## APPENDIX D:

## Supplementary Tables

Table D. 1. Summary of SNR and CTR values for all probes for comparison.

| | DF-TRUS | DP-DF | RMV | EV-8C4 |
|---|---|---|---|---|
| $SNR_{dB}$ (dB) | 19.25 | 24.05 | ~ | ~ |
| $SNR_{Img}$ | 0.86 | 3.66 | 2.6 | 1 |
| $CTR_{dB}$ (dB) | 6.9 | 16.6 | ~ | ~ |
| $CTR_{Img}$ | 0.26 | 1.1 | 4.5 | 1 |

Table D. 2. Preparation methods for sequencing libraries.

| Sonication Device | Sample ID | Average Fragment Size (bp) | Concentration (ng/µL) | Size Selection Method | Average Fragment Size After Library Preparation (bp) |
|---|---|---|---|---|---|
| Covaris | microTUBE with rod | 265 | 7.26 | Pippin Prep | 480 |
| Covaris | microTUBE with rod | 267 | 20.4 | Bead | 440 |
| Covaris | microTUBE with nanodroplets | 259 | 12 | Pippin Prep | 470 |
| Covaris | microTUBE with nanodroplets | 294 | 35.8 | Bead | 420 |
| Ultrasonic Bath | PCR tube no additive | >1,500 | N/A | N/A | N/A |
| Ultrasonic Bath | PCR tube no additive | >1,500 | N/A | N/A | N/A |
| Ultrasonic Bath | PCR tube with nanodroplets | 246 | 24.6 | Bead | 503 |
| | | | 15.6 | Bead | 515 |
| Ultrasonic Bath | PCR tube with nanodroplets | 214 | 32.2 | Bead | 497 |
| | | | 9.4 | Bead | 482 |

Table D. 2. The average fragment size for each sample is shown before and after library preparation. Size selection methods include magnetic bead (Bead) and automatic gel size selection (Pippin Prep, Sage Science). Samples with variable concentrations produced libraries with a similar fragment size.

## REFERENCES


1. Ferlay J, Shin H-R, Bray F, Forman D, Mathers C, Parkin DM. Estimates of worldwide burden of cancer in 2008: GLOBOCAN 2008. Int. J. cancer [Internet]. 2010; 127(12):2893–917.

2. Jemal A, Bray F, Center MM, Ferlay J, Ward E, Forman D. Global cancer statistics. CA. Cancer J. Clin. [Internet]. 61(2):69–90.

3. Siegel RL, Miller KD, Jemal A. Cancer statistics, 2017. CA. Cancer J. Clin. [Internet]. 2017; 67(1):7–30.

4. Jain V, Jain S, Mahajan SC. Nanomedicines based drug delivery systems for anti-cancer targeting and treatment. Curr. Drug Deliv. [Internet]. 2015; 12(2):177–91.

5. Heymach J, Krilov L, Alberg A, Baxter N, Chang SM, Corcoran R, et al. Clinical Cancer Advances 2018: Annual Report on Progress Against Cancer From the American Society of Clinical Oncology. J. Clin. Oncol. [Internet]. 2018; :JCO2017770446.

6. Tomasetti C, Li L, Vogelstein B. Stem cell divisions, somatic mutations, cancer etiology, and cancer prevention. Science [Internet]. 2017; 355(6331):1330–1334.

7. Maley C, Greaves M. Frontiers in Cancer Research [Internet]. New York, NY: Springer New York; 2016.

8. Wagener C, Stocking C, Muller O. Cancer Signaling: From Molecular Biology to Targeted Therapy. Wiley; 2016.

9. Al-Abd AM, Alamoudi AJ, Abdel-Naim AB, Neamatallah TA, Ashour OM. Anti-angiogenic agents for the treatment of solid tumors: Potential pathways, therapy and current strategies - A review. J. Adv. Res. [Internet]. 2017; 8(6):591–605.

10. Walsh JC, Lebedev A, Aten E, Madsen K, Marciano L, Kolb HC. The clinical importance of assessing tumor hypoxia: relationship of tumor hypoxia to prognosis and therapeutic opportunities. Antioxid. Redox Signal. [Internet]. 2014; 21(10):1516–54.

11. Weis SM, Cheresh DA. Tumor angiogenesis: molecular pathways and therapeutic targets. Nat. Med. [Internet]. 2011; 17(11):1359–70.

12. Hellberg C, Ostman A, Heldin C-H. PDGF and vessel maturation. Recent Results Cancer Res. [Internet]. 2010; 180:103–14.

13. Edwards JG, Swinson DEB, Jones JL, Muller S, Waller DA, O'Byrne KJ. Tumor Necrosis Correlates with Angiogenesis and Is a Predictor of Poor Prognosis in Malignant Mesothelioma. Chest. 2003; 124(5):1916–1923.

14. Bachmann IM, Ladstein RG, Straume O, Naumov GN, Akslen LA. Tumor necrosis is associated with increased alphavbeta3 integrin expression and poor prognosis in nodular cutaneous melanomas. BMC Cancer. 2008; 8.

15. Huang D, Lan H, Liu F, Wang S, Chen X, Jin K, et al. Anti-angiogenesis or pro-angiogenesis for cancer treatment: focus on drug distribution. Int. J. Clin. Exp. Med. [Internet]. 2015; 8(6):8369–76.

16. Saaristo A, Karpanen T, Alitalo K. Mechanisms of angiogenesis and their use in the inhibition of tumor growth and metastasis. Oncogene [Internet]. 2000; 19(53):6122–9.

17. Fix SM, Borden MA, Dayton PA. Therapeutic gas delivery via microbubbles and liposomes. J. Control. Release. 2015; 209:139–149.

18. Delaney G, Jacob S, Featherstone C, Barton M. The role of radiotherapy in cancer treatment: estimating optimal utilization from a review of evidence-based clinical guidelines. Cancer [Internet]. 2005; 104(6):1129–37.

19. Barnett GC, West CML, Dunning AM, Elliott RM, Coles CE, Pharoah PDP, et al. Normal tissue reactions to radiotherapy: towards tailoring treatment dose by genotype. Nat. Rev. Cancer [Internet]. 2009; 9(2):134–42.

20. Rukstalis DB. Treatment options after failure of radiation therapy-a review. Rev Urol [Internet]. 2002; 4 Suppl 2:S12-7.

21. Julien JP, Bijker N, Fentiman IS, Peterse JL, Delledonne V, Rouanet P, et al. Radiotherapy in breast-conserving treatment for ductal carcinoma in situ: first results of the EORTC randomised phase III trial 10853. EORTC Breast Cancer Cooperative Group and EORTC Radiotherapy Group. Lancet [Internet]. 2000; 355(9203):528–33.

22. Dosoretz DE, Katin MJ, Blitzer PH, Rubenstein JH, Salenius S, Rashid M, et al. Radiation therapy in the management of medically inoperable carcinoma of the lung: results and implications for future treatment strategies. Int.J.Radiat.Oncol.Biol.Phys. 1992; 24(1):3–9.

23. Gauden S, Ramsay J, Tripcony L. The curative treatment by radiotherapy alone of stage I non-small cell carcinoma of the lung. Chest. 1995; 108(5):1278–1282.

24. Douki T, Ravanat J-L, Pouget J-P, Testard I, Cadet J. Minor contribution of direct ionization to DNA base damage inducedby heavy ions. Int. J. Radiat. Biol. 2006; 82(2):119–127.

25. Fang YZ, Yang S, Wu G. Free radicals, antioxidants, and nutrition. Nutrition. 2002; 18(10):872–879.

26. J. Mundt A. Biological Basis of Radiation Therapy. 2003.

27. Eisenhauer EA, Therasse P, Bogaerts J, Schwartz LH, Sargent D, Ford R, et al. New response evaluation criteria in solid tumours: Revised RECIST guideline (version 1.1). Eur. J. Cancer. 2009; 45(2):228–247.

28. Potiron VA, Abderrahmani R, Cleḿent-Colmou K, Marionneau-Lambot S, Oullier T, Paris F, et al. Improved functionality of the vasculature during conventionally fractionated radiation therapy of prostate cancer. PLoS One. 2013; 8(12).

29. Garcia-Barros M, Paris F, Cordon-Cardo C, Lyden D, Rafii S, Haimovitz-Friedman A, et al. Tumor response to radiotherapy regulated by endothelial cell apoptosis. Science [Internet]. 2003; 300(5622):1155–9.

30. Park HJ, Griffin RJ, Hui S, Levitt SH, Song CW. Radiation-Induced Vascular Damage in Tumors: Implications of Vascular Damage in Ablative Hypofractionated Radiotherapy (SBRT and SRS). Radiat. Res. 2012; 177(3):311–327.

31. Bussink J, Kaanders JH, Rijken PF, Raleigh JA, Van der Kogel AJ. Changes in blood perfusion and hypoxia after irradiation of a human squamous cell carcinoma xenograft tumor line. Radiat. Res. 2000; 153(4):398–404.

32. Denis F, Bougnoux P, Paon L, le Floch O, Tranquart F. Radiosensitivity of rat mammary tumors correlates with early vessel changes assessed by power Doppler sonography. J. Ultrasound Med. 2003; 22(9):921–929.

33. Mayr N, Yuh W, Magnotta V. Tumor perfusion studies using fast magnetic resonance imaging technique in advanced cervical cancer: a new noninvasive predictive assay. Int. J. … [Internet]. 1996; 36(3):623–633.

34. Solesvik O V, Rofstad EK, Brustad T. Vascular changes in a human malignant melanoma xenograft following single-dose irradiation. Radiat. Res. 1984; 98(1):115–128.

35. Maeda A, Leung MKK, Conroy L, Chen Y, Bu J, Lindsay PE, et al. In vivo optical imaging of tumor and microvascular response to ionizing radiation. PLoS One. 2012; 7(8).

36. Bullitt E, Ewend MG, Aylward S, Lin W, Gerig G, Joshi S, et al. Abnormal vessel tortuosity as a marker of treatment response of malignant gliomas: Preliminary report. Technol. Cancer Res. Treat. 2004; 3(6):577–584.

37. Han X, Wang J, Sun Y. Circulating Tumor DNA as Biomarkers for Cancer Detection. Genomics. Proteomics Bioinformatics [Internet]. 2017; 15(2):59–72.

38. Mitchell PS, Parkin RK, Kroh EM, Fritz BR, Wyman SK, Pogosova-Agadjanyan EL, et al. Circulating microRNAs as stable blood-based markers for cancer detection. Proc. Natl. Acad. Sci. [Internet]. 2008; 105(30):10513–10518.

39. Abel HJ, Duncavage EJ. Detection of structural DNA variation from next generation sequencing data: a review of informatic approaches. Cancer Genet. [Internet]. 2013; 206(12):432–40.

40. Lee ES, Lee JM. Imaging diagnosis of pancreatic cancer: a state-of-the-art review. World J. Gastroenterol. [Internet]. 2014; 20(24):7864–77.

41. Druskin SC, Macura KJ. MR Imaging for Prostate Cancer Screening and Active Surveillance. Radiol. Clin. North Am. [Internet]. 2018; 56(2):251–261.

42. De Wever W, Verschakelen J, Coolen J. Role of imaging in diagnosis, staging and follow-up of lung cancer. Curr. Opin. Pulm. Med. 2014; 20(4):385–392.

43. Histed SN, Lindenberg ML, Mena E, Turkbey B, Choyke PL, Kurdziel KA. Review of functional/anatomical imaging in oncology. Nucl. Med. Commun. [Internet]. 2012; 33(4):349–61. 44. Kang H, Lee HY, Lee KS, Kim J-H. Imaging-based tumor treatment response evaluation: review of conventional, new, and emerging concepts. Korean J. Radiol. [Internet]. 13(4):371–90.

45. Fowler AM, Mankoff DA, Joe BN. Imaging Neoadjuvant Therapy Response in Breast Cancer. Radiology [Internet]. 2017; 285(2):358–375. 46. O'Connor JPB, Tofts PS, Miles KA, Parkes LM, Thompson G, Jackson A. Dynamic contrast-enhanced imaging techniques: CT and MRI. Br. J. Radiol. [Internet]. 2011; 84 Spec No:S112-20.

47. Carmeliet P. Angiogenesis in life, disease and medicine. Nature [Internet]. 2005; 438(7070):932–6.

48. Vijayasarathi A, Duszak R, Gelbard RB, Mullins ME. Knowledge of the Costs of Diagnostic Imaging: A Survey of Physician Trainees at a Large Academic Medical Center. J. Am. Coll. Radiol. [Internet]. 2016; 13(11):1304–1310.

49. Feliciano MAR, Uscategui RAR, Maronezi MC, Simões APR, Silva P, Gasser B, et al. Ultrasonography methods for predicting malignancy in canine mammary tumors. PLoS One. 2017; 12(5).

50. Dayton PA, Rychak JJ. Molecular ultrasound imaging using microbubble contrast agents. Front. Biosci. [Internet]. 2007; 12:5124–5142.

51. Blomley MJK, Cooke JC, Unger EC, Monaghan MJ, Cosgrove DO. Science, medicine, and the future: Microbubble contrast agents: a new era in ultrasound. Bmj [Internet]. 2001; 322(7296):1222–1225.

52. Anvari A, Forsberg F, Samir AE. A Primer on the Physical Principles of Tissue Harmonic Imaging. Radiographics [Internet]. 35(7):1955–64.

53. de Jong N, Emmer M, van Wamel A, Versluis M. Ultrasonic characterization of ultrasound contrast agents. Med. Biol. Eng. Comput. [Internet]. 2009; 47(8):861–873.

54. Gessner R, Lukacs M, Lee M, Cherin E, Foster FS, Dayton PA. High-resolution, high-contrast ultrasound imaging using a prototype dual-frequency transducer: In vitro and in vivo studies. IEEE Trans. Ultrason. Ferroelectr. Freq. Control. 2010; 57(8):1772–1781.

55. de Jong N, Bouakaz A, Frinking P. Basic Acoustic Properties of Microbubbles. Echocardiography [Internet]. 2002; 19(3):229–240.

56. Dayton PA, Gessner RC, Phillips L, Shelton SE, Heath Martin K, Lee M, et al. The implementation of Acoustic Angiography for microvascular and angiogenesis imaging. Conf. Proc. ... Annu. Int. Conf. IEEE Eng. Med. Biol. Soc. IEEE Eng. Med. Biol. Soc. Annu. Conf. 2014; 2014:4283–4285.

57. Kasoji SK, Rivera JN, Gessner RC, Chang SX, Dayton PA. Early Assessment of Tumor Response to Radiation Therapy using High-Resolution Quantitative Microvascular Ultrasound Imaging. Theranostics [Internet]. 2018; 8(1):156–168.

58. Bullitt E, Gerig G, Pizer SM, Lin W, Aylward SR. Measuring Tortuosity of the Intracerebral Vasculature from MRA Images. IEEE Trans. Med. Imaging. 2003; 22(9):1163–1171.

59. Gessner RC, Aylward SR, Dayton PA. Mapping microvasculature with Acoustic Angiography yields quantifiable differences between healthy and tumor-bearing tissue volumes in a rodent model. Radiology [Internet]. 2012; 264(3):733–40.

60. Shelton SE, Lee YZ, Lee M, Cherin E, Foster FS, Aylward SR, et al. Quantification of microvascular tortuosity during tumor evolution using Acoustic Angiography. Ultrasound Med. Biol. 2015; 41(7):1896–1904.

61. Streeter JE, Gessner R, Miles I, Dayton PA. Improving sensitivity in ultrasound molecular imaging by tailoring contrast agent size distribution: In vivo studies. Mol. Imaging. 2010; 9(2):87–95.

62. Grant JP, Wells SA. Tumor resistance in rats immunized to fetal tissues. J. Surg. Res. 1974; 16(5):533–540.

63. Schroeder T, Yuan H, Viglianti BL, Peltz C, Asopa S, Vujaskovic Z, et al. Spatial heterogeneity and oxygen dependence of glucose consumption in R3230Ac and fibrosarcomas of the Fischer 344 rat. Cancer Res. 2005; 65(12):5163–5171.

64. Gessner RC, Frederick CB, Foster FS, Dayton PA. Acoustic Angiography: A new imaging modality for assessing microvasculature architecture. Int. J. Biomed. Imaging. 2013; 2013.

65. Aylward S, Kwitt R, McCormick M. TubeTK [Internet]. 2016; Available from: https://public.kitware.com/Wiki/TubeTK.

66. Aylward SR, Bullitt E. Initialization, noise, singularities, and scale in height ridge traversal for tubular object centerline extraction. IEEE Trans. Med. Imaging. 2002; 21(2):61–75.

67. Ungersma SE, Pacheco G, Ho C, Yee SF, Ross J, Van Bruggen N, et al. Vessel imaging with viable tumor analysis for quantification of tumor angiogenesis. Magn. Reson. Med. 2010; 63(6):1637–1647.

68. Fenton BM, Paoni SF, Beauchamp BK, Ding I. Zonal image analysis of tumour vascular perfusion, hypoxia, and necrosis. Br. J. Cancer [Internet]. 2002; 86(11):1831–6.

69. Otsu N. A threshold selection method from gray-level histograms. IEEE Trans. Syst. Man. Cybern. [Internet]. 1979; 9(1):62–66.

70. Paling MR, Shawker TH, Dwyer A. Ultrasonic evaluation of therapeutic response in tumors: its values and implications. J. Clin. Ultrasound [Internet]. 1981; 9(6):281–288.

71. Hermans R. Post-treatment imaging of head and neck cancer. Cancer Imaging. 2004; 4:S6–S15.

72. Kozin S V., Duda DG, Munn LL, Jain RK. Neovascularization after irradiation: What is the source of newly formed vessels in recurring tumors? J. Natl. Cancer Inst. 2012; 104(12):899–905.

73. Gorski DH, Beckett MA, Jaskowiak NT, Calvin DP, Mauceri HJ, Salloum RM, et al. Blockade of the Vascular Endothelial Growth Factor Stress Response Increases the Antitumor Effects of Ionizing Radiation. Cancer Res. [Internet]. 1999; 59(14):3374–3378.

74. Palmowski M, Peschke P, Huppert J, Hauff P, Reinhardt M, Maurer M, et al. Molecular ultrasound imaging of early vascular response in prostate tumors irradiated with carbon ions. Neoplasia [Internet]. 2009; 11(9):856–63.

75. Brenner DJ. Dose, volume, and tumor-control predictions in radiotherapy. Int. J. Radiat. Oncol. Biol. Phys. 1993; 26(1):171–179.

76. Johnson CR, Thames HD, Huang DT, Schmidt-Ullrich RK. The tumor volume and clonogen number relationship: tumor control predictions based upon tumor volume estimates derived from computed tomography. Int. J. Radiat. Oncol. Biol. Phys. 1995; 33(2):281–287.

77. Lövey J, Lukits J, Remenár E, Koronczay K, Kásler M, Németh G, et al. Antiangiogenic effects of radiotherapy but not initial microvessel density predict survival in inoperable oropharyngeal squamous cell carcinoma. Strahlentherapie und Onkol. 2006; 182(3):149–156.

78. Harada H. How Can We Overcome Tumor Hypoxia in Radiation Therapy? J. Radiat. Res. [Internet]. 2011; 52(5):545–556.

79. Pignataro L, Carboni N, Midolo V, Bertolini F, Buffa R, Mario Cesana B, et al. Clinical relevance of microvessel density in laryngeal squamous cell carcinomas. Int. J. Cancer. 2001; 92(5):666–670.

80. Brown JM. Tumor Hypoxia in Cancer Therapy. Methods Enzymol. 2007; 435.

81. Withers HR. Biologic basis for altered fractionation schemes. Cancer. 1985; 55(9 Suppl):2086–2095.

82. Magnuson WJ, Mahal A, Yu JB. No TitleEmerging Technologies and Techniques in Radiation Therapy. Semin. Radiat. Oncol. 2017; 27(1):34–42.

83. Jabbari S, Weinberg VK, Kaprealian T, Hsu IC, Ma L, Chuang C, et al. Stereotactic body radiotherapy as monotherapy or post-external beam radiotherapy boost for prostate cancer: Technique, early toxicity, and PSA response. Int. J. Radiat. Oncol. Biol. Phys. 2012; 82(1):228–234.

84. Hannan R, Tumati V, Xie X-J, Cho LC, Kavanagh BD, Brindle J, et al. Stereotactic body radiation therapy for low and intermediate risk prostate cancer-Results from a multi-institutional clinical trial. Eur. J. Cancer [Internet]. 2016; 59:142–151.

85. Loo DT. In situ detection of apoptosis by the TUNEL assay: An overview of techniques. Methods Mol. Biol. 2011; 682:3–13.

86. McTyre E, Scott J, Chinnaiyan P. Whole brain radiotherapy for brain metastasis. Surg. Neurol. Int. [Internet]. 2013; 4(5):236.

87. Hanahan D, Weinberg RA. Hallmarks of cancer: The next generation. Cell. 2011; 144(5):646–674.

88. Ramsay JO, Silverman BWW. Functional data analysis, 2nd edition [Internet]. 2005.

89. Ullah S, Finch CF. Applications of functional data analysis: A systematic review. BMC Med. Res. Methodol. [Internet]. 2013; 13:43.

90. Muller H-G, Müller H-G. Functional Modeling of Longitudinal Data. Longitud. Data Anal. 2006; :223–252.

91. Yao F, Müller H-G, Wang J-L. Functional Data Analysis for Sparse Longitudinal Data. J. Am. Stat. Assoc. [Internet]. 2005; 100(470):577–590.

92. Yao F, Muller H-G, Wang J. Functional Linear Regression Analysis for Longitudinal Data. Ann. Statictics. 2004; 33(6):2873–2903.

93. King JR, Jackson DA. Variable selection in large environmental data sets using principal components analysis. Environmetrics. 1999; 10(1):67–77.

94. Yao F, Müller H-G, Wang J-L. Functional Data Analysis for Sparse Longitudinal Data. J. Am. Stat. Assoc. 2005; 100(470):577–590.

95. Ullah S, Finch CF. Applications of functional data analysis: A systematic review. BMC Med. Res. Methodol. 2013; 13:43.

96. Wang J-L, Chiou J-M, Mueller H-G. Review of Functional Data Analysis. arXiv Prepr. [Internet]. 2015; :1–47.

97. Gessner R, Dayton PA. Advances in molecular imaging with Ultrasound. Mol. Imaging. 2010; 9(3):117–127.

98. Streeter JE, Herrera-Loeza SG, Neel NF, Yeh JJ, Dayton PA. A comparative evaluation of ultrasound molecular imaging, perfusion imaging, and volume measurements in evaluating response to therapy in patient-derived xenografts. Technol. Cancer Res. Treat. [Internet]. 2013; 12(4):311–21.

99. Zhou J, Wang H, Zhang H, Lutz AM, Tian L, Hristov D, et al. Vegfr2-targeted three-dimensional ultrasound imaging can predict responses to antiangiogenic therapy in preclinical models of colon cancer. Cancer Res. 2016; 76(14):4081–4089.

100. El Kaffas A, Smith K, Pradhan P, Machtaler S, Wang H, von Eyben R, et al. Molecular Contrast-Enhanced Ultrasound Imaging of Radiation-Induced P-Selectin Expression in Healthy Mice Colon. Int. J. Radiat. Oncol. Biol. Phys. 2017; 97(3):581–585.

101. Tsuruta JK, Klauber-DeMore N, Streeter J, Samples J, Patterson C, Mumper RJ, et al. Ultrasound molecular imaging of secreted frizzled related protein-2 expression in murine angiosarcoma. PLoS One. 2014; 9(1).

102. Stieger SM, Dayton PA, Borden MA, Caskey CF, Griffey SM, Wisner ER, et al. Imaging of angiogenesis using Cadence contrast pulse sequencing and targeted contrast agents. Contrast Media Mol. Imaging [Internet]. 3(1):9–18.

103. Tsuruta JK, Schaub NP, Rojas JD, Streeter J, Klauber-DeMore N, Dayton P. Optimizing ultrasound molecular imaging of secreted frizzled related protein 2 expression in angiosarcoma. PLoS One. 2017; 12(3).

104. Fix S, Nyankima A, McSweeney M, Tsuruta J, Dayton P. Accelerated clearance of microbubbles containing polyethylene glycol (PEG) is associated with the generation of anti-PEG antibodies. Ultrasound Med. Biol.

105. Shelton SE, Lindsey BD, Tsuruta JK, Foster FS, Dayton PA. Molecular Acoustic Angiography: A New Technique for High-resolution Superharmonic Ultrasound Molecular Imaging. Ultrasound Med. Biol. 2016; 42(3):769–781.

106. Lin F, Shelton S, Espíndola D, Rojas J, Pinton G, Dayton P. Ultrasound Localization Microscopy for Identifying Microvascular Morphology Features of Tumor Angiogenesis at a Resolution Beyond the Diffraction Limit of Conventional Ultrasound. Theranostics. 2017; 7(1):196–204.

107. Heath Martin K. Dual-frequency piezoelectric transducers for contrast enhanced ultrasound imaging. Sensors. 2014; 14(11).

108. Kim J, Li S, Kasoji S, Dayton PA, Jiang X. Phantom evaluation of stacked-type dual-frequency 1-3 composite transducers: A feasibility study on intracavitary Acoustic Angiography. Ultrasonics. 2015; 63:7–15.

109. Gillies RJ, Kinahan PE, Hricak H. Radiomics: Images Are More than Pictures, They Are Data. Radiology [Internet]. 2015; 278(2):151169.

110. Bouakaz A, Frigstad S, Ten Cate FJ, de Jong N. Super harmonic imaging: A new imaging technique for improved contrast detection. Ultrasound Med. Biol. 2002; 28(1):59–68.

111. Van Neer PLMJ, Danilouchkine MG, Matte GM, Van Der Steen AFW, De Jong N. Dual-pulse frequency compounded superharmonic imaging. IEEE Trans. Ultrason. Ferroelectr. Freq. Control. 2011; 58(11):2316–2324. doi:10.1109/TUFFC.2011.2089.

112. van Neer PLMJ, Danilouchkine MG, Verweij MD, Demi L, Voormolen MM, van der Steen AFW, et al. Comparison of fundamental, second harmonic, and superharmonic imaging: A simulation study. J. Acoust. Soc. Am. 2011; 130(5):3148.

113. van Neer PLMJ, Matte G, Danilouchkine MG, Prins C, van den Adel F, de Jong N. Super-harmonic imaging: development of an interleaved phased-array transducer. IEEE Trans. Ultrason. Ferroelectr. Freq. Control [Internet]. 2010; 57(2):455–68.

114. Martin KH, Lindsey BD, Ma J, Lee M, Li S, Foster FS, et al. Dual-Frequency Piezoelectric Transducers for Contrast Enhanced Ultrasound Imaging. Sensors [Internet]. 2014; 14:20825–20842.

115. American Cancer Society. Cancer Facts & Figures. Cancer Facts Fig. 2016. 2016; :1–9.

116. Applewhite JC, Matlaga BR, McCullough DL. Results of the 5 region prostate biopsy method: the repeat biopsy population. J. Urol. 2002; 168(August):500–503.

117. Norberg M, Egevad L, Holmberg L, Spar??n P, Norl??n BJ, Busch C. The sextant protocol for ultrasound-guided core biopsies of the prostate underestimates the presence of cancer. Urology. 1997; 50(4):562–566.

118. Rabbani F, Stroumbakis N, Kava BR, Cookson MS, Fair WR. Incidence and clinical significance of false-negative sextant prostate biopsies. J. Urol. 1998; 159(4):1247–1250.

119. Stroumbakis N, Cookson MS, Reuter VE, Fair WR. Clinical significance of repeat sextant biopsies in prostate cancer patients. In: Urology. 1997. p. 113–118.

120. Strazdina A, Krumina G, Sperga M. The value and limitations of contrast-enhanced ultrasound in detection of prostate cancer. Anticancer Res. 2011; 31(4):1421–6.

121. Marks L, Young S, Natarajan S. MRI-ultrasound fusion for guidance of targeted prostate biopsy. Curr. Opin. Urol. [Internet]. 2013; 23(1):43–50.

122. Halpern EJ, Gomella LG, Forsberg F, McCue P a., Trabulsi EJ. Contrast Enhanced Transrectal Ultrasound for the Detection of Prostate Cancer: A Randomized, Double-Blind Trial of Dutasteride Pretreatment. J. Urol. [Internet]. 2012; 188(5):1739–1745.

123. Kay P a, Robb R a, Bostwick DG. Prostate cancer microvessels: a novel method for three-dimensional reconstruction and analysis. Prostate [Internet]. 1998; 37(4):270–7.

124. Taneja SS. Imaging in the Diagnosis and Management of Prostate Cancer. Rev Urol. 2004; 6(3):101–113.

125. Krimholtz R, Leedom DA, Matthaei GL. New Equivalent Circuits for Elementary Piezoelectric Transducers. Electron. Lett. [Internet]. 1970; 6(13):398–399.

126. Jensen JA. FIELD: A Program for Simulating Ultrasound Systems. Med. Biol. Eng. Comput. 1996; 34(SUPPL. 1):351–352.

127. Li S, Kim J, Wang Z, Kasoji S, Lindsey B. A Dual-frequency Co-linear Array for Acoustic Angiography in Prostate Cancer Evaluatione. IEEE Trans. Ultrason. Ferroelectr. Freq. Control.

128. Worthington A., Trachtenberg J, Sherar M. Ultrasound properties of human prostate tissue during heating. Ultrasound Med. Biol. [Internet]. 2002; 28(10):1311–1318.

129. Lindsey BD, Rojas JD, Martin KH, Shelton SE, Dayton PA. Optimization of contrast-to-tissue ratio and role of bubble destruction in dual-frequency contrast-specific "Acoustic Angiography" imaging. In: IEEE International Ultrasonics Symposium, IUS. 2014. p. 1774–1777.

130. Matrone G, Savoia AS, Caliano G, Magenes G. Ultrasound Synthetic Aperture Focusing with the Delay Multiply and sum beamforming algorithm. In: Proceedings of the Annual International Conference of the IEEE Engineering in Medicine and Biology Society, EMBS. 2015. p. 137–140.

131. Errico C, Pierre J, Pezet S, Desailly Y, Lenkei Z, Couture O, et al. Ultrafast ultrasound localization microscopy for deep super-resolution vascular imaging. Nature. 2015; 527(7579):499–502.

132. Smolev JK, Heston WD, Scott WW, Coffey DS. Characterization of the Dunning R3327H prostatic adenocarcinoma: an appropriate animal model for prostatic cancer. Cancer Treat. Rep. 1977; 61(2):273–287.

133. Isaacs JT, Isaacs WB, Feitz WFJ, Scheres J. Establishment and characterization of seven dunning rat prostatic cancer cell lines and their use in developing methods for predicting metastatic abilities of prostatic cancers. Prostate. 1986; 9(3):261–281.

134. American Cancer Society. Cancer Facts & Figures. Cancer Facts Fig. 2014. Atlanta Am. Cancer Soc. 2014;

135. TCGA Network. Comprehensive molecular characterization of clear cell renal cell carcinoma. Nature. 2013; 499(7456):43–49.

136. Davis C, Rickets C, Wang M. The somatic genomic landscape of chromophobe renal cell carcinoma. Cancer Cell. 2014; 26:319–330.

137. TCGA Network. Comprehensive Molecular Characterization of Papillary Renal-Cell Carcinoma. N. Engl. J. Med. 2015;

138. Mileto A. Iodine Quantification to Distinguish Clear Cell from Papillary Renal Cell Carcinoma at Dual-Energy Multidetector CT: A Multireader Diagnostic Performance Study. Radiology. 2014; 273(3).

139. Hagenkord JM, Gatalica Z, Jonasch E, Monzon FA. Clinical genomics of renal epithelial tumors. Cancer Genet. 2011; 204(6):285–297. doi:10.1016/j.cancergen.2011.06.001.

140. Lu Q, Huang B. Differentiation of Renal Tumor Histotypes: Usefulness of Quantitative Analysis of Contrast-Enhanced Ultrasound. Am. J. Roentgenol. 2015; 205(3).

141. Shuch B, Amin A, Armstrong AJ, Eble JN, Ficarra V, Lopez-Beltran A, et al. Understanding Pathologic Variants of Renal Cell Carcinoma: Distilling Therapeutic Opportunities from Biologic Complexity. Eur. Urol. 2014;

142. Harvey CJ, Cosgrove D. Role of US Contrast Agents in the Assessment of Indeterminate Solid and Cystic Lesions in Native and Transplant Kidney. RSNA. 2015; 35(5).

143. Wang L. Diagnostic value of quantitative contrast-enhanced ultrasound (CEUS) for early detection of renal hyperperfusion in diabetic kidney disease. J. Nephrol. 2015;

144. Chang EH, Chong WK, Kasoji SK, Dayton PA, Rathmell WK. Management of indeterminate cystic kidney lesions: Review of contrast-enhanced ultrasound as a diagnostic tool. Urology. 2015;

145. Cai Y, Du L, Li F, Gu J, Bai M. Quantification of enhancement of renal parenchymal masses with contrast-enhanced ultrasound. Ultrasound Med. Biol. 2014; 40(7):1387–1393.

146. G. King K, Gulati M. Quantitative assessment of solid renal masses by contrast-enhanced ultrasound with time-intensity curves: how we do it. Abdom. Imaging. 2015;

147. Atri M, Epid D, Tabatabaeifar L. Accuracy of Contrast-enhanced US for Differentiating Benign from Malignant Solid Small Renal Masses. Radiology. 2015; 0(0).

148. Gerst S, Hann L, Li D, Gonen M, Tickoo S, Sohn M, et al. Evaluation of renal masses with contrast-enhanced ultrasound: initial experience. Am. J. Roentgenol. 2011; 194(4):897–906.

149. R Development Core Team. R: A Language and Environment for Statistical Computing [Internet]. R Found. Stat. Comput. Vienna Austria. 2012; 0:{ISBN} 3-900051-07-0.

150. Aoki S, Hattori R, Yamamoto T, Funahashi Y, Matsukawa Y, Gotoh M, et al. Contrast-enhanced ultrasound using a time-intensity curve for the diagnosis of renal cell carcinoma. BJU Int. 2011; 108(3):349–354.

151. Dong Y, Wang W, Cao J, Fan P, Lin X. Quantitative Evaluation of Contrast-Enhanced Ultrasonography in the Diagnosis of Chronic Ischemic Renal Disease in a Dog Model. PLoS One. 2013; 8(8).

152. Karshafian R, Burns PN, Henkelman MR. Transit time kinetics in ordered and disordered vascular trees. Phys. Med. Biol. [Internet]. 2003; 48(19):3225–37.

153. Hudson JM, Williams R, Lloyd B, Atri M, Kim TK, Bjarnason G, et al. Improved flow measurement using microbubble contrast agents and disruption-replenishment: clinical application to tumour monitoring. Ultrasound Med. Biol. [Internet]. 2011; 37(8):1210–21.

154. Vikram R, Ng CS, Tamboli P, Tannir NM, Jonasch E, Matin SF, et al. Papillary renal cell carcinoma: radiologic-pathologic correlation and spectrum of disease. Radiographics [Internet]. 2009; 29(3):741-54–7.

155. Zhang J, Kang SK, Wang L, Touijer A, Hricak H. Distribution of renal tumor growth rates determined by using serial volumetric CT measurements. Radiology. 2009; 250(1):137–144.

156. Xue L, Lu Q. Papillary renal cell carcinoma and clear cell renal cell carcinoma: Differentiation of distinct histological types with contrast-enhanced ultrasonography. Eur. J. Radiol. 2015;

157. Courthod G. Papillary renal cell carcinoma: A review of the current therapeutic landscape. Tucci, Marcello. 2015;

158. Kogan P, Johnson KA, Feingold S, Garrett N, Guracar I, Arendshorst WJ, et al. Validation of dynamic contrast-enhanced ultrasound in rodent kidneys as an absolute quantitative method for measuring blood perfusion. Ultrasound Med. Biol. 2011; 37(6):900–908.

159. Gerlinger M, Horswell S, Larkin J, Rowan AJ, Salm MP, Varela I, et al. Genomic architecture and evolution of clear cell renal cell carcinomas defined by multiregion sequencing. Nat. Genet. 2014; 46(3):225–33.

160. Feingold S, Gessner R, Guracar IM, Dayton PA. Quantitative volumetric perfusion mapping of the microvasculature using contrast ultrasound. Invest. Radiol. 2010; 45(10):669–674.

161. Tang M-X, Mulvana H, Gauthier T, Lim AKP, Cosgrove DO, Eckersley RJ, et al. Quantitative contrast-enhanced ultrasound imaging: a review of sources of variability. Interface Focus [Internet]. 2011; 1(4):520–39.

162. Thomas F, Desmedt C, Aftimos P, Awada A. Impact of tumor sequencing on the use of anticancer drugs. Curr. Opin. Oncol. [Internet]. 2014; 26(3):347–56.

163. Gonzalez-Garay ML. The road from next-generation sequencing to personalized medicine. Per. Med. [Internet]. 11(5):523–544.

164. Knierim E, Lucke B, Schwarz JM, Schuelke M, Seelow D. Systematic comparison of three methods for fragmentation of long-range PCR products for next generation sequencing. PLoS One [Internet]. 2011; 6(11):e28240.

165. Morey M, Fernández-Marmiesse A, Castiñeiras D, Fraga JM, Couce ML, Cocho JA. A glimpse into past, present, and future DNA sequencing. Mol. Genet. Metab. [Internet]. 110(1–2):3–24.

166. Anderson S. Shotgun DNA sequencing using cloned DNase I-generated fragments. Nucleic Acids Res. [Internet]. 1981; 9(13):3015–27.

167. Roe BA. Shotgun library construction for DNA sequencing. Methods Mol. Biol. [Internet]. 2004; 255:171–87.

168. Seed B, Parker RC, Davidson N. Representation of DNA sequences in recombinant DNA libraries prepared by restriction enzyme partial digestion. Gene [Internet]. 1982; 19(2):201–9.

169. Gingrich JC, Boehrer DM, Basu SB. Partial CviJI digestion as an alternative approach to generate cosmid sublibraries for large-scale sequencing projects. Biotechniques. 1996; 21(1):99–104.

170. Hoheisel JD, Nizetic D, Lehrach H. Control of partial digestion combining the enzymes dam methylase and MboI. Nucleic Acids Res. [Internet]. 1989; 17(23):9571–82.

171. Wong KK, Markillie LM, Saffer JD. A novel method for producing partial restriction digestion of DNA fragments by PCR with 5-methyl-CTP. Nucleic Acids Res. [Internet]. 1997; 25(20):4169–71.

172. Osoegawa K, Mammoser AG, Wu C, Frengen E, Zeng C, Catanese JJ, et al. A bacterial artificial chromosome library for sequencing the complete human genome. Genome Res. [Internet]. 2001; 11(3):483–96.

173. Hengen PN. Shearing DNA for genomic library construction. Trends Biochem. Sci. [Internet]. 1997; 22(7):273–4.

174. Burger G, Lavrov D V, Forget L, Lang BF. Sequencing complete mitochondrial and plastid genomes. Nat. Protoc. [Internet]. 2007; 2(3):603–14.

175. Okpodu CM, Robertson D, Boss WF, Togasaki RK, Surzycki SJ. Rapid isolation of nuclei from carrot suspension culture cells using a BioNebulizer. Biotechniques. 1994; 16(1):154–158.

176. Oefner PJ, Hunicke-Smith SP, Chiang L, Dietrich F, Mulligan J, Davis RW. Efficient random subcloning of DNA sheared in a recirculating point-sink flow system. Nucleic Acids Res. [Internet]. 1996; 24(20):3879–86.

177. Thorstenson YR, Hunicke-Smith SP, Oefner PJ, Davis RW. An automated hydrodynamic process for controlled, unbiased DNA shearing. Genome Res. [Internet]. 1998; 8(8):848–55.

178. Schoppee Bortz PD, Wamhoff BR. Chromatin immunoprecipitation (ChIP): revisiting the efficacy of sample preparation, sonication, quantification of sheared DNA, and analysis via PCR. PLoS One [Internet]. 2011; 6(10):e26015.

179. Aparicio O, Geisberg J V, Struhl K. Chromatin immunoprecipitation for determining the association of proteins with specific genomic sequences in vivo. Curr. Protoc. cell Biol. [Internet]. 2004; Chapter 17:Unit 17.7.

180. Teytelman L, Ozaydin B, Zill O, Lefrançois P, Snyder M, Rine J, et al. Impact of chromatin structures on DNA processing for genomic analyses. PLoS One [Internet]. 2009; 4(8):e6700.

181. Poptsova MS, Il'Icheva IA, Nechipurenko DY, Panchenko LA, Khodikov M V., Oparina NY, et al. Non-random DNA fragmentation in next-generation sequencing. Sci. Rep. 2014; 4.

182. Martin KH, Dayton PA. Current status and prospects for microbubbles in ultrasound theranostics. Wiley Interdiscip. Rev. Nanomed. Nanobiotechnol. [Internet]. 5(4):329–45.

183. Chomas JE, Dayton P, May D, Ferrara K. Threshold of fragmentation for ultrasonic contrast agents. J. Biomed. Opt. [Internet]. 2001; 6(2):141.

184. Shi WT, Forsberg F, Tornes A, Ostensen J, Goldberg BB. Destruction of contrast microbubbles and the association with inertial cavitation. Ultrasound Med. Biol. [Internet]. 2000; 26(6):1009–19.

185. Chomas JE, Dayton PA, May D, Allen J, Klibanov A, Ferrara K. Optical observation of contrast agent destruction. Appl. Phys. Lett. [Internet]. 2000; 77(7):1056.

186. Sheeran PS, Luois SH, Mullin LB, Matsunaga TO, Dayton PA. Design of ultrasonically-activatable nanoparticles using low boiling point perfluorocarbons. Biomaterials [Internet]. 2012; 33(11):3262–9.

187. Sheeran PS, Wong VP, Luois S, McFarland RJ, Ross WD, Feingold S, et al. Decafluorobutane as a phase-change contrast agent for low-energy extravascular ultrasonic imaging. Ultrasound Med. Biol. [Internet]. 2011; 37(9):1518–30.

188. Sheeran PS, Dayton PA. Phase-change contrast agents for imaging and therapy. Curr. Pharm. Des. [Internet]. 2012; 18(15):2152–65.

189. Sheeran PS, Rojas JD, Puett C, Hjelmquist J, Arena CB, Dayton PA. Contrast-enhanced ultrasound imaging and in vivo circulatory kinetics with low-boiling-point nanoscale phase-change perfluorocarbon agents. Ultrasound Med. Biol. [Internet]. 2015; 41(3):814–31.

190. Laugharn J, Beckett C. Method and system for acoustically treating material. 2013;

191. Brachmann CB, Davies A, Cost GJ, Caputo E, Li J, Hieter P, et al. Designer deletion strains derived from Saccharomyces cerevisiae S288C: a useful set of strains and plasmids for PCR-mediated gene disruption and other applications. Yeast [Internet]. 1998; 14(2):115–32.